Charge separation in contact systems with CdSe quantum dot layers

Dissertation zur Erlangung des akademischen Grades des Doktors der Naturwissenschaften (Dr. rer. nat.)

eingereicht im Fachbereich Biologie, Chemie, Pharmazie
der Freien Universität Berlin

vorgelegt von

Elisabeth Franziska Zillner

aus Augsburg

2013

Die vorliegende Arbeit wurde in der Zeit von Dezember 2009 bis November 2012 im *Institut for Heterogene Materialsysteme* am *Helmholtz-Zentrum Berlin für Materialien und Energie* unter Leitung von *PD. Dr. Thomas Dittrich* angefertigt.

1. Gutachter: PD. Dr. Thomas Dittrich
2. Gutachter: Prof. Dr. Eckart Rühl

Disputation am 06. März 2013

Abstract

Quantum dot (QD) solar cells are a fast developing area in the field of solution processed photovoltaics. Central aspects for the application of QDs in solar cells are separation and transport of charge carriers in the QD layers and the formation of charge selective contacts. Even though efficiencies of up to 7 % were reached in QD solar cells, these processes are not yet fully understood. In this thesis the mechanisms of charge separation, transport and recombination in CdSe QD layers and layer systems were studied. Charge separation was measured via surface photovoltage (SPV) at CdSe QD layers with thicknesses in the range of monolayers. To determine the influence of interparticle distance of QDs and trap states on the surface of QDs on charge separation, QDs with four different surfactant layers were studied. Layers of CdSe QDs were prepared on ITO, Si, SiO_2 and CdS by dip coating under inert atmosphere. The layers were characterized by Rutherford backscattering spectrometry, UV-vis spectroscopy, step profilometry and scanning electron microscopy to determine the areal density, the absorption and thickness of CdSe QD monolayers. SPV measurements show that initial charge separation from the CdSe QDs on ITO only happened from the first monolayer of QDs. Electrons, photo-excited in the first monolayer of CdSe QDs, were trapped on the ITO surface. The remaining free holes were trapped in surface states and/or diffused into the neighboring QD layers. The thick surfactant layer ($\approx$ 1.6 nm) of pristine QDs had to be reduced by washing and/or ligand exchange for separation of photo-excited charge carriers. Both, interparticle distance and trap density, influenced the processes of charge separation and recombination. SPV transients of CdSe monolayers could be described by a single QD approximation model, based on Miller-Abrahams hopping of holes between the delocalized excitonic state, traps on the surface of the QD and the filled trap on the ITO surface (recombination). The values of QD-ITO distance and trap density, determined with the simulation were consistent with transmission electron microscopy and photoluminescence measurements. The separation and diffusion of charge carriers was limited due to trapping of charge carriers. Smaller interparticle distances led to faster decays in CdSe QD monolayers. However the increase of traps, which resulted in a slower decay dominated and led to longer decay times of SPV transients of modified CdSe QD layers. By deposition of CdSe QDs on CdS a heterojunction was created. The CdS layer served as acceptor for electrons excited in CdSe QDs. Furthermore a CdSe QD/CdTe nanoparticle heterojunction was realized by successive electrophoretic deposition. CdSe QDs acted as electron acceptors, whereas CdTe nanoparticles acted as electron donors. Charge separation was dominated by the CdSe QD/CdTe nanoparticle interphase, as inverted layer stacking of CdSe QDs and CdTe nanoparticles gave an inverted SPV signal.

Zusammenfassung

Quantenpunkt (QD) Solarzellen sind ein junges Gebiet im Bereich der Photovoltaik. Für die Verwendung von QDs in Solarzellen sind Trennung und Transport von Ladungsträgern in QD-Schichten und ladungsselektive Kontakte zentrale Aspekte. Obwohl schon Wirkungsgrade von bis zu 7 % für QD-Solarzellen erreicht wurden, liegt noch kein vollständiges Verständnis über diese Prozesse vor. In dieser Arbeit wurden die Mechanismen von Ladungstrennung, -transport und -rekombination in CdSe-QD-Schichten und Schichtsystemen untersucht. Die Ladungstrennung wurde durch Oberflächenphotospannung (SPV) an CdSe-QD-Schichten im Bereich von Monolagen gemessen. Um den Einfluss von Partikelabstand und Störstellendichte auf der Oberfläche von QDs zu bestimmen, wurden QDs mit vier unterschiedlichen Oberflächenmodifikationen untersucht. Die QD-Schichten wurden über eine Tauchbeschichtung unter Inertatmosphäre auf ITO, Si, SiO_2 und CdS hergestellt. Die Schichten wurden mit Rutherford-Rückstreu-Spektrometrie, UV-Vis-Spektroskopie, Step-Profilometrie und Rasterelektronenmikroskopie untersucht, um die Flächendichte, die Absorption und die Dicke von CdSe-QD-Monolagen zu bestimmen. SPV Untersuchungen zeigen, dass die anfängliche Ladungstrennung aus CdSe-QDs auf ITO nur von der ersten Monolage von CdSe-QDs ausging. Elektronen, welche in der ersten CdSe-QD-Monolage angeregt wurden, wurden an ITO-Oberflächendefekten eingefangen. Die verbleibenden freien Löcher wurden an Defekten auf der QD-Oberfläche eingefangen und/oder diffundierten in benachbarte QD-Schichten. Eine Reduzierung der Dicke der Moleküllage ($\approx$ 1.6 nm) auf den ursprünglichen QDs durch Waschen und/oder Ligandenaustausch war nötig um Trennung von angeregten Ladungsträgern zu erreichen. Sowohl der Abstand zwischen QDs als auch die Defektdichte beeinflussten die Prozesse von Ladungstrennung und -rekombination. SPV-Transienten an CdSe-QD-Monolagen konnten durch ein Modell separater QDs beschrieben werden. Das Model basiert auf thermisch angeregten Übergängen der Löcher (Miller-Abrahams Sprünge) zwischen dem delokalisiertem exzitonischem QD-Zustand, den Defektzuständen auf der QD-Oberfläche und dem besetztem Defekt auf der ITO-Oberfläche (Rekombination). Die Werte der Simulation der SPV-Transienten für den ITO-QD-Abstand und der Defektdichte stimmen mit den Transmissionselektronenmikroskopie- und Photolumineszenzmessungen überein. Die Trennung und Diffusion der Ladungsträger ist durch die Defektzustände transportlimitiert. Ein geringerer QD-Abstand führte in CdSe-QD-Monolagen zu schnelleren Transienten, wobei die Verlangsamung der Transienten durch höhere Defektdichten dominierte und zu längeren Abklingzeiten der SPV-Transienten von modifizierten CdSe-QD-Schichten führte.

Durch Abscheiden von CdSe-QDs auf CdS wurde ein Heteroübergang geschaffen. Die CdS-Schicht diente als Akzeptor für in CdSe-QDs angeregte Elektronen. Zudem wurde ein CdSe-QD/CdTe-Nanopartikel-Heteroübergang durch aufeinander folgendes elektrophoretisches Abscheiden der QDs und Nanopartikel realisiert. Die CdTe-Nanopartikel fungierten als Elekronendonatoren, wobei die CdSe QDs als Elektronenakzeptorn in dem System dienten. Die Ladungstrennung wurde durch die CdSe-QD/CdTe-Nanopartikel-Grenzfläche dominiert, da umgekehrte Schichtstapelung zu einem invertierten SPV-Signal führte.

Contents

1 Introduction

Climate change and the growing scarcity of fossil fuels demand for alternative and renewable energy sources. The biggest source of energy is the sun, which provides the earth with ≈ 10,000 times the amount of energy than is consumed.[1,2] Photovoltaic cells are one possibility to use this energy, by a conversion of solar energy into electricity. Photovoltaic cells will have to provide power in the range of terawatts to have an impact, as a world wide power consumption of 46 TW is predicted by 2100.[3] Current PV-technologies cannot provide power in this scale, as they either require scarce materials as In (CIGS and thin-film Si solar cells), Te (CdTe solar cells), Ru (dye-sensitized solar cells), or Ag (electrodes of crystalline and thin-film Si solar cells) or have a high energy input in fabrication (crystalline Si solar cells).[1,4] Therefore new concepts for solar cells from available elements with low energy production have to be developed.

One new concept is quantum dot (QD) solar cells. QDs are "fragments of semiconductor[s] consisting of hundreds to many thousands of atom...Quantum dots exhibit strongly size-dependent optical and electrical properties"[5] Due to their tunable band gap they expand the range of materials suitable for absorbers in solar cells.[4] PbS for example is a relative cheap, abundant material, with a high absorption coefficient whose band gap can be enlarged by QDs.[4] Additional multi exciton generation[6,7] and the extraction of hot charge carriers[8] have been shown in QDs. Both mechanisms bear the opportunity to enhance the efficiency of solar cells and even to overcome the Schockley-Queisser Limit.[9]

Four different concepts of QD solar cells are currently studied, (i) Schottky barrier solar cells, (ii) inorganic heterojunction solar cells , (iii) QD-sensitized solar cells and (iv) hybrid solar cells. Figure 1.1 gives an overview of the morphology and electronic structure of the different QD solar cell concepts. All cells are superstrate solar cells which are build onto a transparent oxide (ITO or FTO) and illuminated

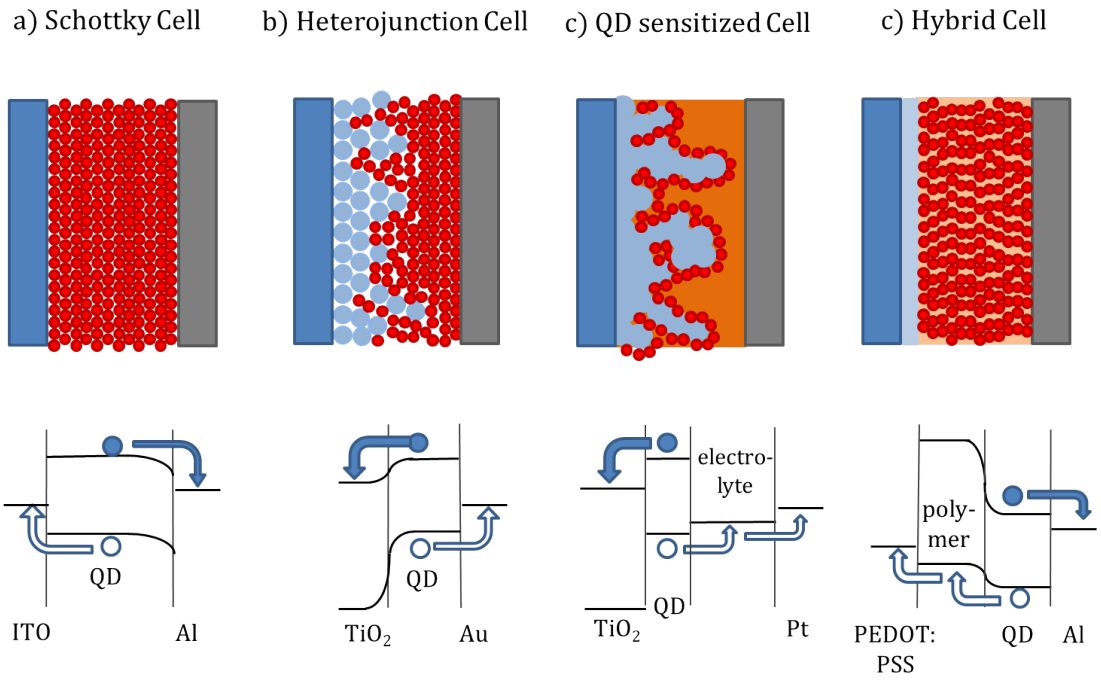

Figure 1.1: Scheme of the architecture and energy levels in different QD solar cell concepts, adapted from Pattantyus-Abraham et al.[10] and Skompska.[11] The cells are all superstrate solar cells which are build onto a transparent conductive oxide (ITO or FTO) and illuminated from the bottom.

from the bottom.

The easiest approach is the Schottky barrier solar cell (see figure 1.1 a) using a Schottky junction as charge selective contact. Efficiencies as high as 4 % have been achieved with PbS and PbSe QD absorbers for this type of solar cells.[12–20] However Schottky solar cells suffer from a low open circuit voltage (V_{OC}) and a small fill factor (FF) due to the low barrier of hole injection into the cathode.[10] Therefore recent research focused on different heterojunction solar cells. In the heterojunction solar cell two semiconductor materials are brought into contact, such that one semiconductor serves as an electron acceptor and the second one as an electron donor, thus avoiding injection of electrons at the anode and holes at the cathode.

The schemes in figure 1.1 (b - d) show different architectures of heterojunction solar cells; b) an all inorganic heterojunction, c) a QD sensitized solar cell with an electrolyte and d) a hybrid solar cell with a hole conducting polymer. Generally

a high interface between donor and acceptor is favorable as QD layers suffer from small exciton diffusion lengths. For the inorganic heterojunction solar cell different concepts were investigated. QDs were for example deposited on a wide bandgap semiconductor, which serves as electron acceptor. Examples are the deposition of PbS QDs on nanoporous TiO_2[10,21,22] or ZnO,[23] reaching efficiencies as high as 7 %[22] and 4.4 %,[23] respectively. Another approach is the use of nanorods, for example TiO_2 nanopillars,[24] providing both a high interface and a direct diffusion path of electrons in the TiO_2 towards the cathode. Apart from wide bandgap semicondcutors also heterjunctions between two QDs, which both absorb in the visible range were realized. Tang et al. and Liu et al. built solar cells with a heterojunction between p- and n-doped PbS QDs, reaching efficiencies up to 6.1 %.[25,26]

An alternative approach of QD solar cells are QD sensitized solar cells which follow the principle of dye sensitized solar cells[27] (see figure 1.1 c). Instead of dyes as absorption centers QD are applied. QDs are deposited on TiO_2 nanoparticles, a wide bandgap semiconductor, which serves as electron acceptor. PbS QDs,[28] PbSeS QDs,[28] CdSe QDs,[29,30] CdS QDs[31] and CdSe quantum rods[32] were for example used as absorbers. The photo-excited hole in the QD is injected into a redox electrolyte. The conventional used redox couple for dye sensitized solar cells I^-/I_3^- has the disadvantage of being corrosive to many metals and QDs. Therefore it was exchanged with a sulfide/polysulfide (S^{2-}/S_n^{2-}) redox couple, which stabilizes QDs.[30,31] Efficiencies up to 2.7 %, 3 % and 3.2 % were reached with CdSe quantum rods,[32] CdSe QDs[29] and CdS QDs[31] absorbers, respectively.

In Hybrid QD solar cells the heterojunction is created between QDs and a conjugated conducting polymer (see figure 1.1 d). The polymer serves as an electron donor. Photo-excited holes in the QDs are injected into the polymer. QDs and polymer are mixed into a blend to ensure a high interface and short diffusion paths for excitons in the QD domains. Blends used in hybrid QD solar cells were for example PCP-DTBT[i]:CdSe nanorods and QDs,[33,34] P3HT[ii]:CdSe QDs,[35,36] and P3HT:CdSe hyperbranched crystals,[37] reaching efficiencies of 3.4 %,[33] 2 %[36] and 1.1 %.[37]

[i] poly[2,6-(4,4-bis-(2-ethylhexyl)-4H-cyclopental[2,1-b;3,4-b']-dithiophene)-alt-4,7-(2,1,3-benzothiadiazole)]

[ii] Poly(3-hexylthiophen)

Even though QD solar cells with efficiencies as high as 7 %[22] have been realized, the mechanisms of charge separation and transport in QD layers are still not fully understood. Colloidal QDs, which are synthesized in a solution based synthesis, need capping agents to avoid agglomeration and preserve the confinement of charges. Common ligands, used in the synthesis of QDs are organic molecules, for example trioctylphosphine (TOP) and oleic acid (OA). For the application of QDs in solar cells interparticel charge transport in QD layers and injection of charges at the contacts is required. Thus an optimum between confinement of charges in QDs and electronic coupling between QDs has to be achieved. The exchange of long ligand molecules like TOP and OA is therefore a key step for the application of QDs in solar cells. Guyot-Sionnest et al. showed a strong increase of conductivity in CdSe QDs layers by ligand exchange of TOP/TOPO with diamines and dithiols.[38,39] Diamines and dithiols do not only decrease the distance between QDs but also link them. Conductivities of up to 10^{-2} S/cm^2 were measured for 1,4-phenylenediamine linked CdSe QDs.[38,39] A 600-fold increase in maximum power output in PbS QD hybrid solar cells was reached by exchanging OA with octylamine and annealing of the QD layer to 220 °C.[40] Capping of PbS QDs with benzenedithiol and 3-mercaptopropionic acid led to efficiencies of 3.6 % in the infrared for Schottky barrier solar cells[18] and more than 5 % for inorganic heterojunction solar cells.[10,21]

In addition to the reduction of interparticle distance, defect passivation at the surface of QDs plays a major role. The passivation of dangling bonds at the QD surface is crucial to avoid trapping of charge carriers. Higher mobility of charge carriers in 3-mercaptopropionic acid capped PbS QDs inorganic heterojunction solar cells was ascribed to improved passivation of defects.[41] 3-mercaptopropionic acid has two types of functional groups, thiols and carboxylate groups, which both passivate the QD surface.[41] The current highest efficiency for QD solar cells of 7 % was reached by a combined passivation of PbS QDs with 3-mercaptopropionic acid and halide anions.[22] The halide anions bind to sites that cannot be accessed by the organic ligand. This highlights the importance of surface control and passivation of the QD surface for an effective electron transport and high efficiency QD solar cells.

In this thesis layers of CdSe QD were used as a model system for the investigation of charge separation and transport processes in thin QD layers. Colloidal CdSe

QDs were chosen as they have a high stability in suspension and their optoelectronic properties are well known. CdSe QDs with a diameter of 4.5 ± 0.5 nm and varying surfactants were studied. Pristine QDs had a thick layer of OA and TOP surfactants (pristine OA + TOP CdSe QDs). The thickness of the surfactant layer of these QDs was reduced by washing (washed OA + TOP CdSe QDs). To reduce the interparticle distance of QDs in layers further the OA + TOP surfactants were exchanged by pyridine (pyridine capped CdSe QDs). For linking of QDs 1-4-benzenedithiol (dithiol) was used, as it is a strongly binding, conjugated bidentate linker. Exchange with dithiol was applied on pyridine capped CdSe QD layers (dithiol capped CdSe QDs).

Charge separation in CdSe QD layers was measured by surface photovoltage (SPV). The SPV signal is proportional to the number and distance between centers of separated electrons and holes and can be measured in time and spectral dependency. Both fast and slow charge separation processes can be determined by the fixed capacitor and Kelvin probe setup, respectively. Furthermore SPV was proven to be sensitive to charge separation in the monolayer range of CdSe and CdTe QDs.[42] Pl is complementary to SPV as in PL radiatively recombining charge carriers are detected, whereas in SPV only separated charge carriers can be measured. Photoluminescence (PL) measurements at room temperature and at 4 K were applied to determine transitions by radiative recombination.

In **chapter 2** the properties of quantum dots, the conductivity of QD films in general, the properties of CdSe QDs and the conduction of CdSe films in particular are described.

Chapter 3 describes the CdSe QDs that were used and gives an overview of the methods that were applied. Thin homogeneous layers in the monolayer range were prepared by dip coating. For the measurement of spectral and time dependent charge separation SPV was applied. Absorption and radiative recombination of charges in CdSe QD layers was measured by UV-vis and photoluminescence spectroscopy. Rutherford-Backscattering spectrometry was used to determine areal densities of Cd and Se in CdSe QD layers.

The results of the thesis are described and discussed in **chapter 4**. The chapter is divided into four sections.

In the first section (**section 2.1.2**) the morphology, thickness and absorption of CdSe QD layers, prepared by dip coating, are determined. These informations are required to analyze the results of SPV measurements in the following sections. Transmission electron microscopy, Rutherford-Backscattering spectrometry, UV-vis spectroscopy, step profilometry and scanning electron microscopy were applied to determine the interparticle distance, the areal density, the absorption and the thickness of a single CdSe QD monolayer.

This section is followed by the determination of charge separation in pyridine capped CdSe QDs on ITO (**section 4.2**). Determining the influence of photon energy, light intensity and layer thickness on the charge separation led to the conclusion that initial charge separation took place only in the first monolayer of QDs.
The role of ligand exchange is studied in **section 4.3**. The influence of ligand exchange on the optical properties in terms of photon absorption and photoluminescence of CdSe QD layers is determined. The density of defect states and the interparticle distance is correlated with charge separation leading to the single QD approximation model. SPV transients could be simulated with this model and trap densities and interparticle distances being in agreement with TEM and PL measurements were found.

In the last section (**section 4.4**) charge separation in CdSe QD layer systems is measured and the influence of the substrate is discussed. Injection of charges into a CdS layer and CdTe nanoparticles is measured and the formation of a CdSe QD/CdS layer and CdSe QD/CdTe nanoparticle layer is shown.

The results are summarized in **chapter 5** and an outlook on the use of CdSe QDs in solar cells is given.

2 Fundamentals

2.1 Properties of semiconductor quantum dots

2.1.1 Electronic states of quantum dots

"There is plenty of room at the bottom...in the science of ultra-small structures" was the famous statement of R. Feymann at a talk given in the year 1959.[43] In this talk R. Feymann described his vision of fantastic and numerous possibilities if one could control the size and dimension of objects in the nanometer range and thus create objects with completely new properties lying in between atoms/molecules and solids. Nanoparticles are located at this junction between atoms/molecules and solids consisting of 100 to 10,000 atoms. Going from a solid 'infinite' crystal to an atom the density of states change from continuous bands to discrete energy levels. As the energy levels of nanocrystals lie in between atoms/molecules and solid 'infinite' crystals, their electronic properties are size dependent. For semiconductors the Fermi level is located between two bands, therefore the optical and electronic properties are mainly dominated by the edges of the energy bands. As the edges of a band develop last, even for relatively large particles (around 10,000 atoms) discrete energy levels are observed.[44] The change in electronic and optical properties observed in semiconductor nanoparticles relative to the semiconductor solid material is called quantum size effect. Semiconductor nanoparticles that show a quantum size effect are called quantum dots. Figure 2.1 illustrates the effect of reduced dimension in a semiconductor. The energy levels become discrete near the energy level when going from an infinite "3D" crystal to a "0D" quantum dot.[45]

The discrete energy levels for electrons in a quantum dot, can be described by quantum mechanics in the easiest case as an electron in a spherical potential well

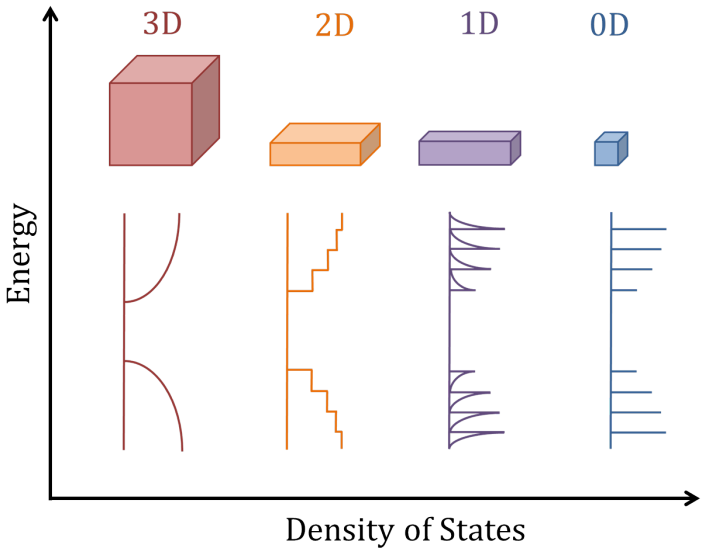

Figure 2.1: Density of states in a semiconductor as a function of dimension.[45]

with infinite barriers.[46] The solution $\psi(r)$ of the time independent Schrödinger equation

$$\left[\frac{-\hbar^2}{2m_e}\bigtriangledown^2 + U(r)\right]\psi(r) = E\psi(r) \tag{2.1}$$

is the wavefunction of the electron. By applying the Hamilton operator $H = \left[\frac{\hbar^2}{2m_e}\bigtriangledown^2 + U(r)\right]$ on the wavefunction the eigenvalues E_n and therefore the allowed energy states of the electrons are obtained. The potential energy $U(r)$ depends solely on the distance $r = \sqrt{x^2 + y^2 + z^2}$ and is[46]

$$U(r) = \begin{cases} 0, & \text{for } r < a \quad (2.2a) \\ \infty, & \text{for } r \geq a, \quad (2.2b) \end{cases}$$

where a is the radius of the quantum dot. The Laplace operator $\triangle = \bigtriangledown^2$ in spherical coordinates includes radial and spherical parts, the radius r the azimuth angle $0 \leq \varphi \leq 2\pi$ and the polar angle $0 \leq \theta \leq \pi$ and consists of[46]

$$\triangle = \bigtriangledown^2 = \bigtriangledown_r^2 + \frac{1}{r^2}\bigtriangledown_{\varphi\theta}^2 . \tag{2.3}$$

Therefore the Schrödinger equation for an electron in a spherical potential can be written as[46]

$$\left[\bigtriangledown_r^2 + \frac{1}{r^2}\bigtriangledown_{\varphi\theta}^2 + \frac{2m_e}{\hbar^2}(E - U(r))\right]\psi(r,\varphi,\theta) = 0. \tag{2.4}$$

The wavefunction can be separated into a radial- and an angle-dependent function $\psi(r,\varphi,\theta) = X(r)Y(\varphi,\theta)$, as the potential $U(r)$ is independent on the angle. Using the boundary condition that the wavefunction has to vanish for $r = a$ and equation 2.4 a solution for the radial function $X(r)$ is[46]

$$X(r) = \sqrt{\frac{2}{a}}\frac{sin(kr)}{r}, \tag{2.5}$$

with $k = g_{nl}/a$. g_{nl} are the roots of the corresponding Bessel function. The boundary condition that $X(r)$ has to vanish for $r = a$ leads to a quantization and to three new quantum numbers $n = 1, 2, 3, ...$, $l = 0, 1, 2, 3, ...$ and $m = 0, \pm1, \pm2, ..., \pm l$, where l is called the orbital quantum number and therefore the states $l = 0$, $l = 1$ and $l = 2$ are called analogous to atomic orbitals s, p and d and m is the orbital magnetic quantum number. The resulting energies of an electron in the allowed stationary states are[46]

$$E_{nl} = \frac{\hbar^2}{2m_e a^2}g_{nl}^2, \tag{2.6}$$

where m_e is the effective mass of the electron. Therefore the energy of the electron in a quantum dot has discrete values and scales with the inverse square of the quantum dot radius a. As g_{10} equals π , the lowest energy of an electron in an allowed state is therefore[46]

$$E_{10} = \frac{\hbar^2}{2m_e a^2}\pi^2. \tag{2.7}$$

Equation 2.6 and 2.7 give the confinement energy of an electron in a quantum dot with a radius a. To get an estimation of the energy of optical transitions in quantum dots one has to consider the macro crystalline band gap of the material plus the confinement of the electron in the conduction band and the hole in the valence band, which form during absorption. Therefore the easiest estimation for

the transition of the first excitonic peak, where $n = 1$ and $l = 0$ is[47]

$$E = E_{gap} + E_{10}^{e} + E_{10}^{h} = E_{gap} + \frac{\hbar^2 \pi^2}{2a^2}\left(\frac{1}{m_e} + \frac{1}{m_h}\right), \tag{2.8}$$

where m_h denotes the effective mass of the hole. The energy of the first excitonic peak is changed by the Coulomb attraction between electron and hole and by the solvation energy induced by the surrounding medium (equation 2.9).[47,48]

$$\begin{aligned} E &= E_{gap} + E_{10}^{e} + E_{10}^{h} - E_{Coulomb} + E_{Sol} \\ &= E_{gap} + \frac{\hbar^2 \pi^2}{2a^2}\left(\frac{1}{m_e} + \frac{1}{m_h}\right) - \frac{1.8}{\varepsilon_{in}}\frac{e^2}{4\pi\varepsilon_0 a} + \frac{e^2}{a}\sum_{n=1}^{\infty}\frac{(\frac{\varepsilon_{in}}{\varepsilon_{out}} - 1)(n+1)}{\varepsilon_{in}(\frac{\varepsilon_{in}}{\varepsilon_{out}} + n + 1)}\left(\frac{S}{a}\right)^{2n} \end{aligned} \tag{2.9}$$

ε_{in} and ε_{out} are the dielectric constants of the quantum dot and the surrounding medium, respectively, e is the elementary charge, and S is the magnitude of the distance that the wave function peaks from the center of the spherical particle. Table 2.1 lists the electronic parameters of a few selected crystalline direct band gap semiconductors. The effective electron and hole mass are in units of the free electron mass (9.11×10^{-31} kg).

	E_{gap} (eV)	m_e	m_h	ε_{in}
CdTe	1.43	0.11	0.41	7.1
GaAs	1.52	0.07	0.68	10.9
CdSe	1.75	0.13	0.45	5.8
CdS	2.58	0.19	0.8	5.7
ZnO	3.44	0.24	0.45	3.7

Table 2.1: Band gap (E_{gap}), effective electron (m_e) and hole mass (m_h) and the optical dielectric constant of a few selected crystalline direct band gap semiconductors.[47,49]

Table 2.2 shows the energy shifts of the first excitonic peak of QD with a diameter of 6 nm relative to the band gap of the bulk semiconductor. The values calculated with equation 2.9 and the electronic parameters given in table 2.1. The calculations were done for QD in vacuum therefore $\varepsilon_{out} = 1$ and S/a was set to 0.2. The total shifts varied between 0.09 and 0.59 eV, while the kinetic energy had the

biggest share and the influence of the solvation energy was minor.

	E_{Kin}	$E_{Coulomb}$	E_{Sol}	E_{total}
CdTe	0.48	-0.12	0.05	0.41
GaAs	0.66	-0.11	0.04	0.59
CdSe	0.41	-0.15	0.05	0.32
CdS	0.27	-0.15	0.05	0.17
ZnO	0.27	-0.23	0.06	0.09

Table 2.2: Energy shifts of the first excitonic peak in QDs of selected semiconductors ($d = 6\,\text{nm}$) due to the kinetic energy ($E_{kin} = E^e_{10} + E^h_{10}$), the Coulomb energy ($E_{Coulomb}$) and the solvation energy (E_{Sol}) summing up to a total shift E_{total}. The energy values are given in eV.[47]

2.1.2 Optical absorption in CdSe QDs

CdSe is a direct semiconductor with a band gap of 1.75 eV and a Bohr exciton radius of 5.4 nm. Therefore CdSe absorbs light with wavelengths higher than 708 nm, that means in the whole visible range and thus is black. The electronic and optical properties of CdSe QDs depend on the size of the QDs. Nanoparticles which are smaller than the Bohr exciton radius of 5.4 nm show a quantum size effect. The band gap can be tuned in the region from 1.75 eV up to 2.8 eV.[50] CdSe QDs are highly luminescent and can show luminescence in the whole range of the visible light. CdSe QDs are chemically stable and are probably the most intensively studied QDs.

Equation 2.9[47] can be used to get an approximation for the energetic position of the first excitonic peak (E_{1s}) of CdSe QDs. In table 2.1 the electronic parameters of CdSe used for the calculation of the first ecxitonic peak are listed. Figure 2.2 shows the resulting energetic positions of the first excitonic peak from the equation of Brus[47] plotted against the diameter of CdSe QDs in the range from 2 to 8 nm, when using $\varepsilon_{out} = 1$ and $\frac{S}{a} = 0.2$. The position shifts from 1.9 eV for 8 nm QDs to 5.2 eV for 2 nm QDs.

Jasieniak et al.[51] did an extensive study of the size-dependent absorption properties of CdSe QDs in suspension. In agreement with an earlier study of Yu et al.[52] they found the following correlation between the first excitonic peak and size of QDs, determined by TEM, for QDs between 2 and 8 nm.

$$D(nm) = 59.608 - 0.547\lambda + 1.887 \times 10^{-3}\lambda^2 - 2.857 \times 10^{-6}\lambda^3 + 1.630 \times 10^{-9}\lambda^4 \tag{2.10}$$

In figure 2.2 the theoretical values determined from the equation of Brus[47] and the experimental correlation by Jaseniak[51] are compared. Equation 2.9 clearly gives energies which are too large, especially in the region of the smaller QDs, when compared to the experimental data.

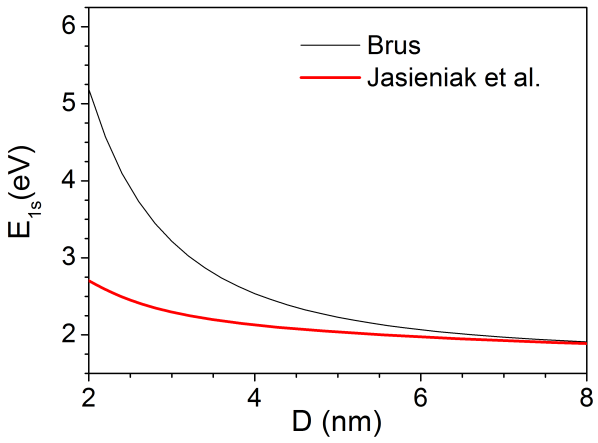

Figure 2.2: Size-dependent position of the first excitonic peak of CdSe QDs. Comparison of the theoretical position after Brus (equation 2.9)[47] and the experimental determined correlation by Jasieniak.[51]

Also the extinction coefficient of CdSe QD at the first excitonic peak varies with the position of the first excitonic peak and thus with the size of QDs. Smaller QDs, having an excitonic peak at higher energies, have a smaller extinction coefficient than larger QDs. For CdSe QDs with an excitonic peak (E_{1S}) between 2.00 and 2.72 eV the following exponential function was found.[51]

$$\epsilon_{1s}(M^{-1}cm^{-1}) = 155507 + 6.670\,54 \times 10^{13} e^{\left(-\frac{E_{1S}}{0.105\,51\,\mathrm{eV}}\right)} \tag{2.11}$$

The absorption of CdSe QDs at higher energies approaches the absorption of bulk CdSe and is therefore independent on the size of QDs. An absorption coefficient α of $1.33 \times 10^5\,\mathrm{cm}^{-1}$ at 350 nm (3.54 eV) was both determined theoretically and

experimentally.[51,53]

Optical properties of CdSe QDs are not only determined by their size. The surrounding of the QDs influence their absorption properties. Therefore CdSe QDs with equal sizes can have their first excitonic peak at different energy positions. One possible factor is a higher effective radius than the true radius. In this case the electron and/or the hole is not completely confined in the QD. This is either due to an electronic coupling of neighboring QDs in layers,[48,54,55] or due to an extension of the electron and/or the hole into the surrounding medium. Extension of electrons in the CdS shell of CdSe/CdS core/shell QDs was for example proposed by Liu et al.[56]. The second factor influencing the position of the first excitonic peak is the dielectric screening by the surrounding medium. This causes changes in the Coulomb energy and the solvation energy (see equation 2.9).[48,55] QDs in layers with a small interparticle distance often show a significant broadening and shift of the first excitonic peak. Both, an electronic coupling and a change in the dielectric environment, lead to this large shift.[57]

2.1.3 Photoluminescence of CdSe QDs

While UV-vis spectroscopy is applied to study the absorption of CdSe QDs, photoluminescence (PL) gives information about the transitions in CdSe QDs. Comparing the position of the first excitonic peak in UV-vis and PL, a relatively large Stokes shift is observed. The lowest excitonic state in wurzite CdSe is eightfold degenerated, in CdSe QDs this excitonic state is split into five levels, by the crystal shape asymmetry, the intrinsic crystal field and the electron-hole exchange interaction.[58] The asymmetry of the crystal shape is due to the non-spherical shape of the nanocrystal and the intrinsic asymmetry of the hexagonal lattice structure of the crystal (see also figure 3.1).[59] The splitting becomes larger with smaller QD diameter. Two of the five states, including the ground state are optically passive. Therefore these states do not appear in UV-vis spectroscopy, but are active in PL. As the lowest state is an optically passive one, a large Stokes shift results. The Stokes shift is the difference between the mean energy of the three light exciton states and the dark ground state. Efros et al. measured Stokes shifts of $35 \pm 5\,\mathrm{meV}$, $55 \pm 5\,\mathrm{meV}$ and $90 \pm 5\,\mathrm{meV}$ for CdSe QDs with a diameter

of 8 nm, 4 nm and 2.4 nm, respectively.[58]

The lifetime of excitons in CdSe QDs is strongly size and temperature dependent.[60] Exciton lifetimes in the range of μs have been measured for CdSe QDs at temperatures below 10 K.[60,61] CdSe QDs with a diameter of 1.7 nm had lifetimes as high as 1.4 µs, while 6.3 nm large QDs had lifetimes of only 0.3 µs for the dark exciton. At higher temperature the lifetimes of excitons decrease as the electron is thermally excited from the dark ground state into the higher lying bright state, resulting in lifetimes in the range of 10 ns[60] at room temperature.

Comparing suspensions to layers of CdSe QDs the emission line of the first excitonic peak is shifted even further to lower energies due to the Förster energy transfer.[62] The rate of electronic energy transfer is defined as[63]

$$k_{DA} = \tau_D^{-1} \left(\frac{R_0}{R_{DA}} \right)^6 \tag{2.12}$$

where R_{DA} is the distance between the donor and the acceptor, R_0 it the Förster distance and τ_D the lifetimes of the excited donor. Values in the range of $1 \times 10^8\,\mathrm{s}^{-1}$ for k_{DA} and 5 nm for R_0 were determined by Kagan et al. for CdSe QDs.[63]

Figure 2.3 illustrates the processes of light absorption, charge carrier relaxation, Förster energy transfer and radiative recombination in a QD layer.[62] The rates of Förster energy transfer ($1 \times 10^8\,\mathrm{s}^{-1}$) are much smaller than the rates of absorption ($10^{14}\,\mathrm{s}^{-1}$) and the vibrational relaxation ($10^{12}\,\mathrm{s}^{-1}$), but are faster than the rates of radiative recombination at low temperature and in the same range as radiative recombination at room temperature. Therefore the charge carriers mainly relax into the lowest excitonic state first and are subsequently transfered to the neighboring QD with the lowest energy state, i. e. the largest QD, where the charge carriers recombine. The inhomogeneities in the size of QDs lead to a shift of charge carriers into the larger QDs and therefore a shift of the first excitonic peak to lower energies.[62,63]

Apart from the first excitonic peak, defect peaks with a lower energy are observed in PL spectroscopy. CdSe QDs have traps at the surface of QDs from which charge carriers can recombine radiatively and nonradiatively. Trap states for charge carriers at the surface of CdSe QDs are nonsaturated Cd and Se dangling bonds or states introduced by surfactants. In a CdSe QD with an unreconstructed surface

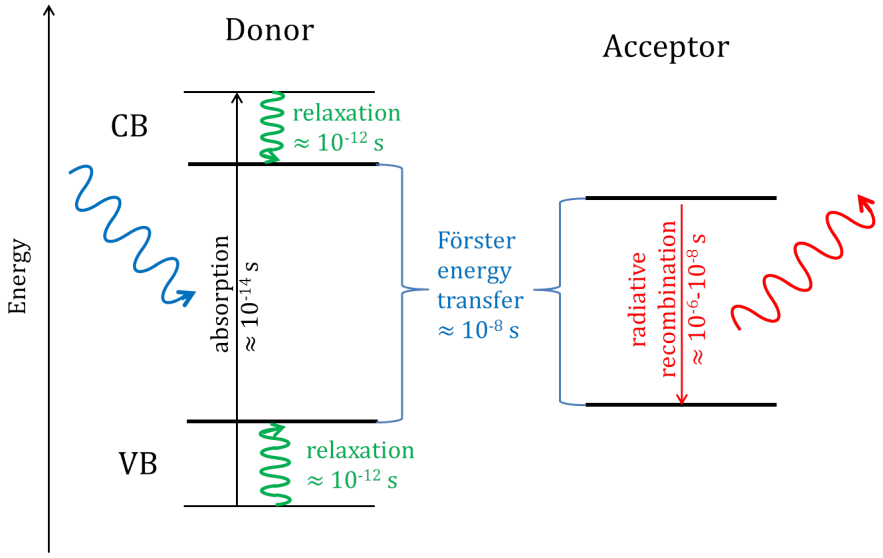

Figure 2.3: Scheme of the processes of light absorption, charge carrier relaxation, Förster energy transfer and radiative recombination in a QD layer. (Adapted from Murray et al.[62]

electrochemically unsaturated surface atoms serve as traps. The Cd surface atoms are electron and the Se surface atoms are hole traps.[64] Surface reconstruction, where the surface Se atoms have an outward displacement of $\approx 0.2\,\text{Å}$ and the Cd atoms an inward displacement of $\approx 0.5\,\text{Å}$, leads to a shift of the Cd surface atoms into the conduction band and the Se surface atom with one dangling bond into the valence band.[65] A midbandgap state of Se edge atoms with two dangling bonds persists as a deep hole trap.[66]

The PL in CdSe QDs is determined by the exciton dynamics illustrated in figure 2.4 (adapted from Underwood et al.)[64]. The short-lived emission results from the recombination of the excited electron with the hole and from recombination of the hole with the electron from the Se dangling bond. The long-lived emission is due to recombination of the electron from the dark ground state, which is a triplet state with the hole in the valence band and the hole in the Se dangling bond.

Surfactant molecules can also introduce trap states.[67] If the molecule has a highest occupied molecular orbital (HOMO) which is higher in energy than the valence band of the CdSe QD the HOMO serves as a trap state for holes. Quenching of radiative recombination by trapping of holes is for example known from pyridine and thiol compounds. Pyridine, being an aromat, has a high lying HOMO and

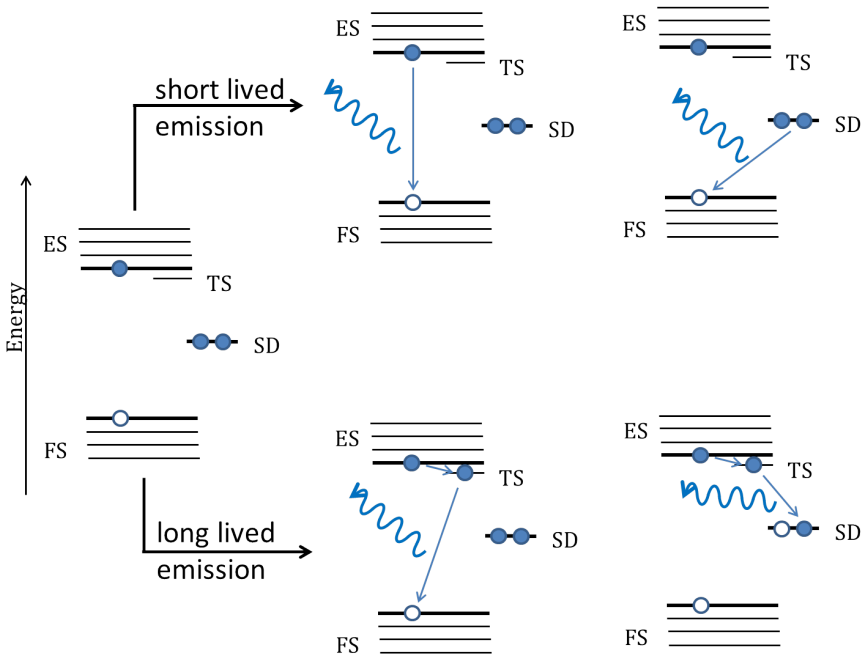

Figure 2.4: Model of exciton dynamics in CdSe QDs. The short lived band edge emission results from immediate recombination of the electron and the hole after excitation or from recombination of the hole with an Se surface dangling bond (SD). The long lived emission results from recombination of the electron in the dark ground state (TS), which is a triplet state with the valence band hole and the hole in the Se dangling bond. FS and ES denote filled and empty states. (Adapted from Underwood et al.)[64]

can stabilize holes in its π ring.[68] Thiol compounds form a covalent bond between the Cd at the surface of CdSe QDs and the sulfur atom. Holes are trapped in the lone pairs of this bonds and quench the photoluminescence.[68,69]

2.2 Conductivity in QD layers

For the application of CdSe QD layers in solar cells a charge carrier transfer between QDs needs to be realized. An optimum between charge carrier confinement for the engineering of the band gap by the quantum size effect and electronic coupling between QDs for charge carrier transfer has to be found. Colloidal QDs are typically synthesized with a stabilizing shell of trioctylphosphine (TOP) and oleic acid (OA). These bulky molecules inhibit charge transfer between QDs in QD layers. Therefore a ligand exchange with smaller and/or linking molecules is done. Guyot-Sionnest et al. was the first one to introduce a ligand exchange at TOP/TOPO capped CdSe QDs, reaching mobilities of up to $10^{-2}\,\mathrm{cm}^2/(\mathrm{Vs})$ with 1,4-phenylenediamine linked QDs.[39,70] Mobilities of up to $10\,\mathrm{cm}^2/(\mathrm{Vs})$ were measured by Lee et al. and band-like transport was claimed.[71]

2.2.1 Charge transport in QD layers

Different models of charge transport in QD layers exist. First one can distinguish between strongly and weakly coupled QDs.[72] Strong coupling of QDs is reached when the coupling is larger than the natural line width and the variation in energy of involved states $h\Gamma \geqslant k_B T$ and $h\Gamma \geqslant \Delta E$.[72,73] h is the Planck's constant, Γ the tunneling rate between two orbitals of neighboring QDs and ΔE the difference in energy between the orbitals involved. When strong coupling is reached the discrete QD orbitals form a mini-band in analogy to bulk crystals, with a width of $h\Gamma$ (see figure 2.5a).[72] The mobility of charges in QD layers forming a mini-band increases with decreasing temperature, showing band-like transport.

In the weak coupled region where $h\Gamma \ll k_B T$ a charge transport takes place via hopping. Different models of charge carrier hopping are discussed, (i) tunneling of the electron to a neighboring QD due to electronic coupling, without the influence of phonons (see figure 2.5b); (ii) thermally activated hopping of electrons, which

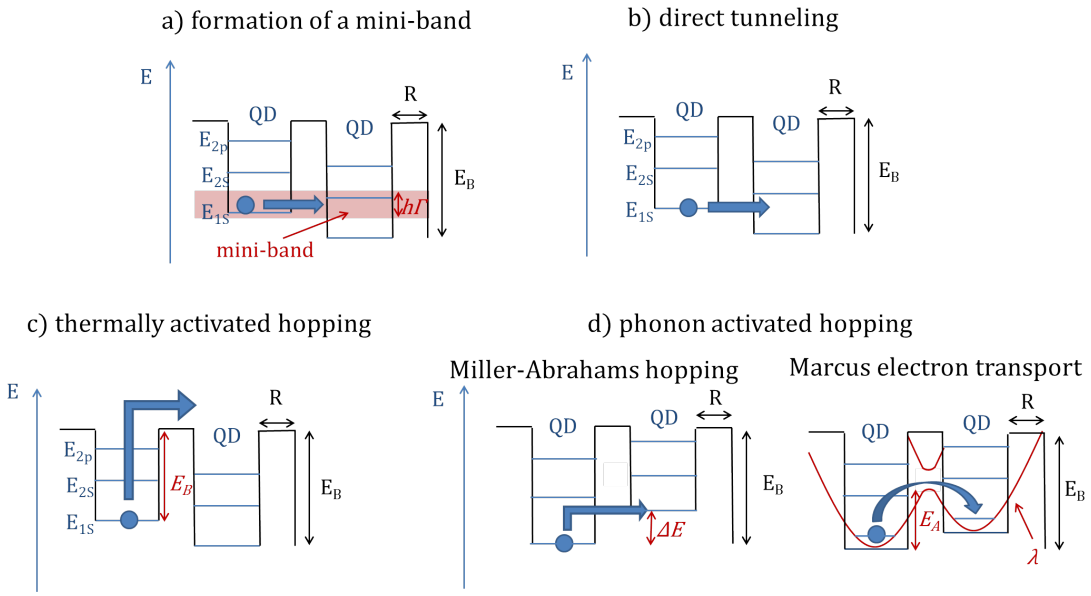

Figure 2.5: Illustration of different charge transport mechanisms in QD layers; a) formation of a mini-band, b) direct tunneling, c) thermally activated hopping, d) phonon assisted hopping. E_B and R are the energy and the width of the barrier separating QDs, $h\Gamma$ is the width of the mini-band. ΔE is the difference in energy between the acceptor and donor state. E_A and λ are the activation and reorganization energy as defined by Marcus.

were excited to energies higher than the potential barrier introduced by the ligand (see figure 2.5c); (iii) phonon assisted hopping (see figure 2.5d).[74]

For direct tunneling of electrons the width of the electronic states in the QDs (k_BT) has to be larger than the variation in their energetic position ΔE. The energetic position of the states varies due to different sizes and the nature of the surroundings of QDs. In the second hopping transport mechanism, the electrons are thermally activated to QD eigenstates higher in energy than the potential barrier E_B and are then freely transported to the neighboring QD. Phonon assisted hopping describes tunneling of electrons coupled with phonons. The electrons absorb one or multiple phonons during the hopping step.[74] The mobility of charges transported by hopping is increasing with increasing temperature.

For phonon assisted hopping different models exist. One model is the tunneling by Miller-Abrahams hopping.[75] In this model a phonon is used to overcome the energy mismatched between electron donor and acceptor during the tunneling

process if the energy of the acceptor state is higher than the energy of the donor. For tunneling to lower energy states no phonon is required (see equation 2.13).

$$\Gamma = \begin{cases} \Gamma_0 e^{-2\alpha R} e^{-(\Delta E)/k_b T}, & \text{for } \Delta E > 0 \quad (2.13a) \\ \Gamma_0 e^{-2\alpha R}, & \text{for } \Delta E \leqslant 0 \quad (2.13b) \end{cases}$$

In equation 2.13 $\alpha = \sqrt{\frac{m_e E_B}{2\hbar^2}}$ is the inverse tunneling length and R is the width of the barrier. Another model is the model by R. A. Marcus.[76] In the Marcus Theory electron transfer requires a reorganization of the system. This reorganization is reflected in the reorganization energy λ, which is related to the activation energy E_A for charge transport:

$$E_A = \frac{(\lambda + \Delta E)^2}{4\lambda} \quad (2.14)$$

The resulting rates of electron transfer are therefore

$$\Gamma = \Gamma_0 e^{\frac{-(\lambda+\Delta E)^2}{4\lambda k_B T}} \quad (2.15)$$

The Marcus theory is the only model which considers the energy required for the reorganization of charges in a QD due to electron donation or acceptation. In Marcus Theory a phonon is also required to overcome an activation energy if electrons hop into a lower lying state. The equation by Miller-Abrahams does not consider coupling with phonon for this case. The disadvantage of the Marcus Theory is that the reorganization energy and therefore also the activation energy for charge transport is often not known.

For the formation of a mini-band the reorganization energy is also important. If an electron is in a delocalized mini-band the reorganization energy has be to overcome. To favor an extended mini-band over a confined state the electron coupling constants between QDs have to be higher than the reorganization energy.[74]

2.2.2 Charge transport in CdSe QD layers

In section 2.2.1 different mechanisms of charge transport in QD layers were described. In this section these mechanisms are compared for their feasibility in CdSe QD layers, deposited from colloidal QDs. The discussion is mainly based on publications by Chu et al.[74] and Guyot-Sionnest et al.[73]

The formation of a mini-band in CdSe QD layers is quite unlikely due to multiple reasons. Band formation requires coupling larger than the energy detuning and larger than the natural line width of the states. The fluctuation in quantum confinement due to size variations and a small density of states close to the band gap in QDs causes large differences in the energies of the first excitonic state. Further disorder in the system, as variations in coupling due to different interparticle distances, electron-electron repulsion and thermal broadening, causes charge transfer by a hopping mechanism.[73] Additionally Chu et al. calculated reorganization energies which were much higher than the electron coupling constants, therefore the electron prefers to be confined inside the QD instead of being in an extended mini-band.[74]

To achieve direct tunneling, without the involvement of phonons, the electron accepting QD should have a state at the same energy level as the state the electron is in, in the electron donating QD. As mentioned before, the variation in QDs size and therefore the differences in the energetic position of the first excitonic state and a low density of states makes this very unlikely. To realize resonant coupling the energy differences in the electronic states (typically around 50 mV for 5 % size distribution) would have to be smaller than the coupling energies (around 1 meV).[74]

For hopping over the barrier introduced by the surfactants the electron needs to overcome a barrier of approximately 2.4 eV for CdSe QDs of $d = 5\,\mathrm{nm}$. This barrier is a lot higher than reorganization energies calculated for phonon assisted hopping (in the range of 1 meV). Therefore a phonon assisted hopping as described by the Marcus Theory is the most likely transport mechanism in conducting CdSe QD layers.[74]

3 Materials and Methods

3.1 CdSe QDs

3.1.1 Size and crystal structure of CdSe QDs

CdSe QDs were synthesized and provided by Bayer Technology Services (BTS). The TEM image in Figure 3.1 a) shows CdSe QDs as dark spots. A size of 4.5 ± 0.5 nm could be determined from TEM measurements. In Figure 3.1 b) one QD (marked by the white circle in the TEM image) is enlarged.

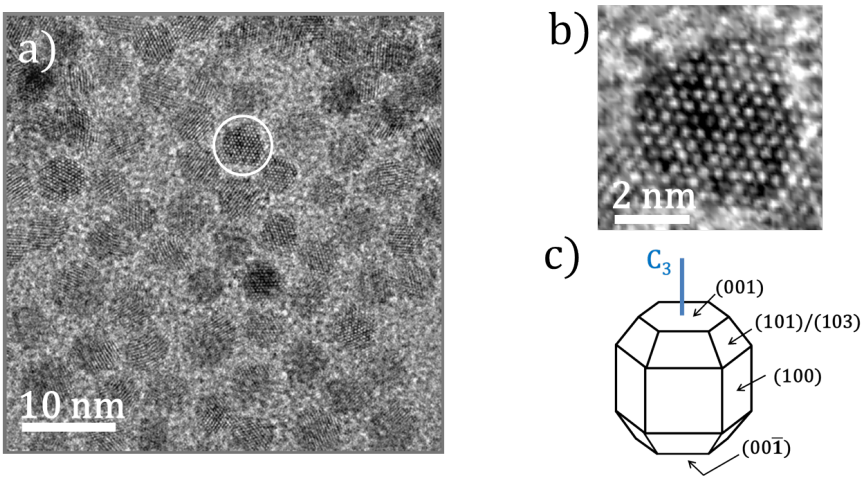

Figure 3.1: a) TEM image of CdSe QDs on a polymer film; b) enlarged view of a CdSe QD oriented along the (001) axis; c) wireframe outline of a model crystallite.

The high-resolution TEM image in figure 3.1b) shows lattice crystal fringes, giving evidence of the crystallinity of the QD. The QD has a Wurtzite structure and is oriented along the (001) axis, its hexagonal shape and the lattice planes along the (100) plane are clearly visible. A lattice spacing of 0.39 nm was determined which

is close to the theoretical value of 0.37 nm for Wurtzite CdSe.[77]

Figure 3.1 c) shows a wireframe outline of a model crystallite with the indices for the various surface types and the C_3 axis. The symmetry of the Wurtzite space group C_{6v}^4 is reduced to C_{3v} in the QD. The unreconstructed (001) surface is purely terminated by Cd, whereas the $(00\bar{1})$ surface is Se terminated. Therefore the horizontal mirror plane is removed.[59]

Figure 3.2 shows an x-ray diffractogram of a drop cast CdSe QD layer (pyridine capped) with the reflections of the Wurtzite and the Zincblende structure. No change in the x-ray diffractogram due to ligand exchange or heating to 200 °C was observed. The characteristic reflections of the Wurtzite structure at 35° and 46° are present, but smaller than expected for a pure Wurtzite structure. Therefore our QDs might consist of a mixture of Wurtzite and Zincblende structure. Whereas the Wurtzite has a stacking order of ABABAB, the Zincblende structure has an ABCABC stacking. Bawendi et al. describe a CdSe QD XRD spectrum very similar to ours.[78] By simulation of the data Bawendi et al. achieved the best fit of the XRD spectrum by a Wurtzite structure with one stacking fault per QD, which is equal to one stacking fault in 10 planes for 3.5 to 4.0 nm QDs.[78] The resulting stacking in the structure would therefore be ABABABCBCB. Thus our QDs have a Wurtzite structure with approximately 1 stacking fault per QD.

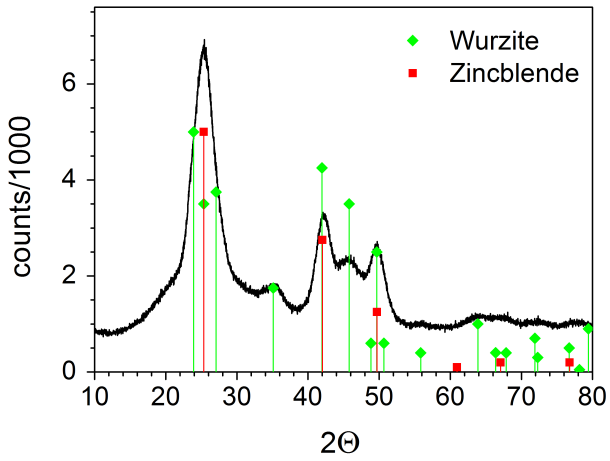

Figure 3.2: X-ray diffractogram of CdSe QDs, including the reflections of the Wurzite and Zincblende structure.

From the peak width of the reflections in the x-ray diffractogram the mean size of

the CdSe crystallites can be calculated. The full width at half maximum (FWHM) of the peak is inversely proportional to the size (L) of the crystallites as described by the Scherrer equation (equation 3.1).[79,80]

$$B(2\Theta) = \frac{K\lambda}{Lcos\Theta} \tag{3.1}$$

$B(2\Theta)$ is the FWHM of a reflection at 2Θ, λ the excitation wavelength, which is 0.1542 nm (copper K_α radiation) and $cos\Theta$ the cosine of the position of the reflection. Using the Scherrer constant $K = 0.94$ for spherical crystals a crystal size of 3.4±0.1 nm is calculated from the full width at half maximum of fitted Gaussian peaks (reflections at 42.1° and 49.8°). The crystal size is smaller than the size of QDs 4.5±0.5 nm measured from TEM images. The size of QDs is underestimated by the Scherrer equation as a spherical shape is estimated, therefore elongation of QDs and edges due to the hexagonal shape are not considered.

3.1.2 Surfactant exchange at CdSe QDs

The surface treatments, except the exchange with benzene-dithiol were developed by BTS.[33,81] Figure 3.3 gives an overview of the ligands used as surfactants for CdSe QDs. To stabilize the QDs during the synthesis oleic acid (OA) and trioctylphosphine (TOP) were used. Therefore pristine CdSe QDs had a stabilizing shell of OA and TOP and were dispersed in toluene. For the ligand exchange, the excess capping ligands of CdSe QDs from the synthesis were washed away in methanol and the CdSe QDs were recovered by centrifugation, followed by stirring in n-hexane for 12 h at room temperature inside a glovebox. Subsequently, additional washing with methanol was performed at least twice. The washed CdSe QDs were re-dispersed in chlorobenzene and are referred to as TOP + OA capped washed CdSe QDs in the thesis. For pyridine capped CdSe QDs the as described washed QDs were redispersed in pyridine and refluxed for at least 8 h at 108 °C. Finally, the pyridine-capped CdSe quantum dots were precipitated in n-hexane and recovered by centrifugation. The recovered nanoparticles were re-dispersed in pyridine as a stock solution.

The exchange of surfactants with 1-4-benzene-dithiol (dithiol) was done in a layer and not in dispersion. 1-4-benzene-dithiol is a bidental ligand and links QDs with

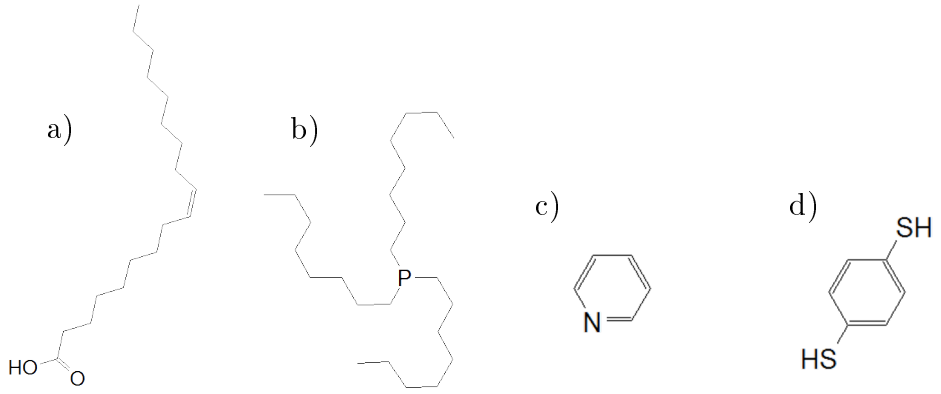

Figure 3.3: Surfactants for the stabilization of CdSe QDs, a) oleic acid, b) trioctylphosphine, c) pyridine and d) 1-4-benzene-dithiol.

each other. An exchange in dispersion leads to agglomeration and precipitation of QDs. For the exchange with dithiol thin layers of QDs were immersed for 20 min in a solution of dithiol in acetonitrile ($c = 3.5$ mM). Afterwards the layer was shortly dipped into acetonitrile to remove excess dithiol. Stable layers, which were no more soluble in the original solvent, toluene for TOP + OA pristine, chlorobenzene for TOP + OA washed and pyridine for pyridine capped CdSe QDs, were only formed by using pyridine capped CdSe QD layers. The stable layer points towards a ligand exchange which forms bonds between CdSe QDs. For layers with thicknesses above 50 nm formation of cracks was observed. Therefore dithiol capped CdSe QDs were prepared from layers of pyridine capped QDs with a thickness below 50 nm.

To investigate the surfactant shell the CdSe QDs were dried and analyzed by TGA-MS (thermo-gravimetric analysis with mass spectrometry). By TGA-MS the amount of organic surfactants in CdSe QD samples could be determined. For the measurements the samples were heated under He with 5 °C/s up to 600 °C and the evaporated fragments were determined by time of flight mass spectrometry (ToF-MS).

Figure 3.4 shows a TGA-MS measurement of pristine OA + TOP capped CdSe QDs. After the procedure 67 % of the original mass remained. Therefore we had a mass loss of 33 %, which can be assigned to the surfactants. Thus the mass fraction of organics in pristine CdSe QD was 33 %. In the first region (up to 330 °C) 17 % of the mass was lost, in the second region from 330 °C up to 600 °C

16 % of mass was lost. Molecules being attached directly to the QD were stronger bound than molecules surrounding the QD in a second shell. Thus the 17 % mass lost in the first region could be assigned to a weakly bound second shell, whereas the mass of molecules directly bounded to the QD surface was 16 %.

To assign the mass losses to a ligand, gaseous decomposition products were monitored by ToF-MS. In the measurement the ToF-MS signals of fractions of OA (236.23 u), TOP (117.08 u) and toluene (91.06 u) are monitored (u is the atomic mass unit defined as $1.660\,538\,921 \times 10^{-27}$ kg). All three compounds showed two main peaks, the first around 200 °C, located in the first region, the second around 430 °C located in the second region. Therefore the molecules measured at 430 °C were from the inner shell surrounding the QD, those at 200 °C were weaker bound molecules from the outer shell. The weight percentages of TOP+OA and toluene were 4 % and 11 %.

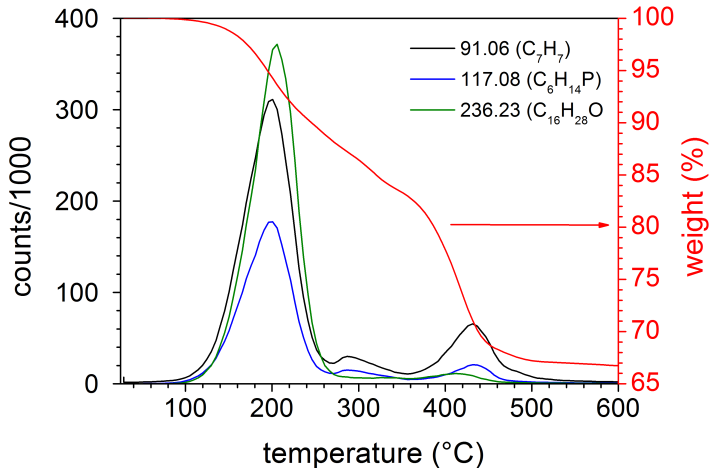

Figure 3.4: TGA-MS measurement of TOP + OA capped pristine CdSe QDs. The sample was heated under He with 5 °C/s.

Figure 3.5 shows the TGA-MS measurement of washed CdSe QDs. The mass of the sample after heating to 600 °C under He was 80 % of its original mass. Therefore an overall amount of 20 % of organics was present and the amount of organics was reduced by 39 % by washing. The weight loss of the sample started at around 250 °C compared to 100 °C for the TOP+OA pristine sample. Therefore the organics were stronger bounded to the QDs and the outer shell was removed during the washing procedure. The masses detected in the ToF-MS were 232.22 u,

236.25 u and 238.27 u. These masses are fragments of TOP and OA and were measured at temperatures between 350 °C and 600 °C. In this region a mass loss of 16 % was observed. Thus the outer shell of surfactants was removed, but the amount of molecules directly bound to the QD surface was not reduced by the washing procedure.

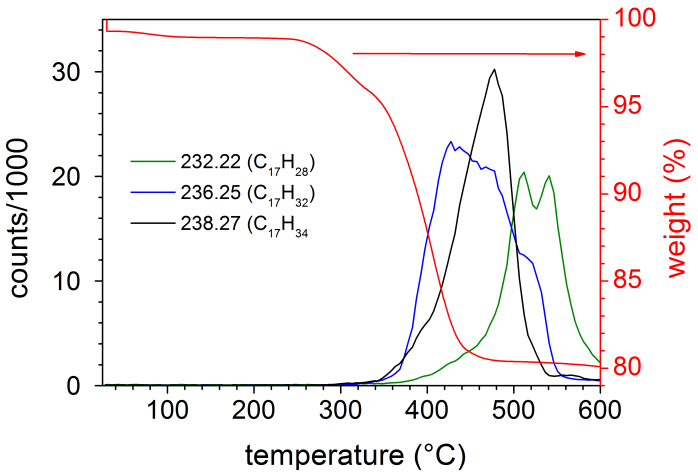

Figure 3.5: TGA-MS measurement of TOP + OA capped washed CdSe QDs. The sample was heated under He with 5 °C/s.

In figure 3.6 the TGA-MS measurement of the pyridine CdSe QDs is displayed. Note that the ToF-MS signal of pyridine (79 u) was divided by 10. The overall mass loss during the TGA-MS, being equal to the amount of organic material in the sample was 16 %. As seen for the pristine TOP+OA sample the spectrum could be divided into two parts. Below 330 °C, where the outer shell of surfactants was detected and from 330 °C up to 600 °C where directly bound molecules were detected. The outer shell consisted entirely of pyridine and had a weight percentage of 5 %, whereas for the inner shell pyridine as well as heavier fragments from TOP and OA were detected. The inner shell has weight percentage of 11 % and consisted of 4 % pyridine and 7 % OA and TOP.

Also the ligand exchange with dithiol was studied. In contrast to SPV measurements the exchange was performed in suspension to obtain a sufficient amount of material. 80 mL of dithiol solution ($c = 3.5$ mM) were added to 1.5 mL of CdSe (pyridine capped) suspension (100 mg/g). The suspension was stirred for 30 min and afterwards centrifuged for 10 min at 3000 r/min. The supernatant was rinsed

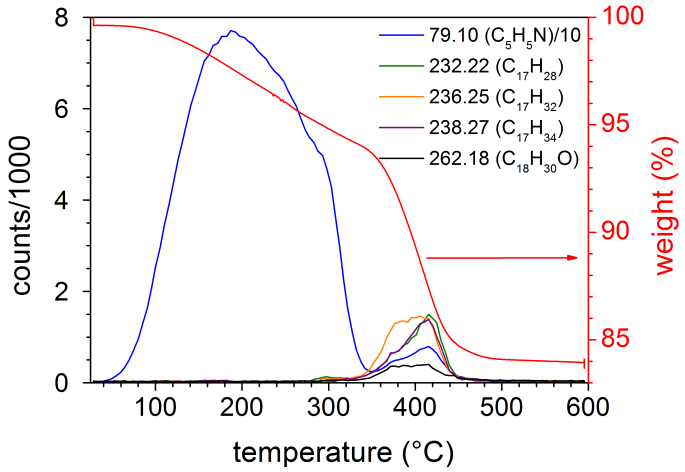

Figure 3.6: TGA-MS measurement of pyridine capped CdSe QDs. The sample was heated under He with 5 °C/s. Note that the signal from C_5H_5N was divided by 10.

away and the QDs were washed three times with 20 mL of acetonitrile to remove excess dithiol. The QD powder was left in the glovebox for drying for 12 h before the TGA-MS measurement.

Figure 3.7 shows the TGA-MS measurement of dithiol capped CdSe QDs. The mass of the QDs was reduced to 88 % of its original weight. Therefore an overall amount of 12 % of organics was present. A clear devision as for pyridine and TOP+OA capped QDs into two parts was not possible. The pyridine signal (79.10 u) is located at a temperature below 330 °C and can therefore be assigned to a weak bounded outer shell. Other compounds are thiophenol (110.18 u) which is the monothiol of benzene and therefore a dithiol fragment and a mono- and dithiol- with longer chains, probably from a reaction of dithiol with OA and/or TOP. These compounds had two peaks, one around 335 °C and one at 387 °C. These peaks were probably from single (335 °C) and double bounded (387 °C) dithiol molecules. The overall amount of pyridine and dithiol in the sample was 5 % and 7 %, respectively. Table 3.1 gives an overview of the measured content of surfactants in the dried QD samples.

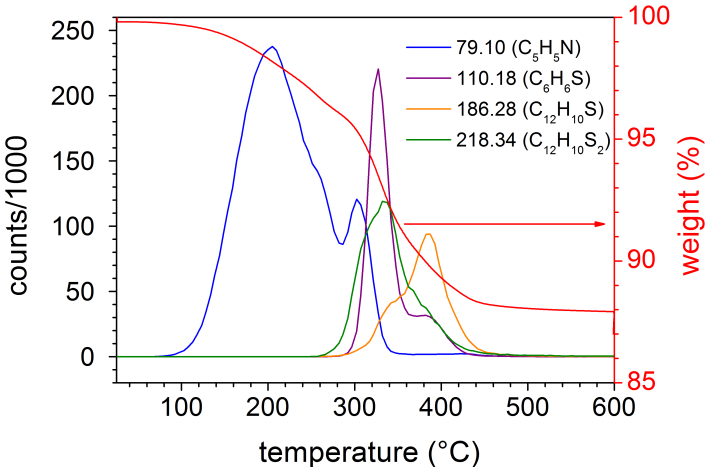

Figure 3.7: TGA-MS measurement of dithiol capped CdSe QDs. The sample was heated under He with 5 °C/s.

.

	TOP+OA	pyridine	dithiol
TOP+OA pristine	33 %	-	-
TOP+OA washed	20 %	-	-
pyridine	7 %	9 %	-
dithiol	-	5 %	7 %

Table 3.1: Content of the surfactants in dried QD samples.

3.2 Layer preparation by dip coating

3.2.1 Principles of dip coating

Ultra-thin layers of CdSe QDs were prepared by dip coating inside the glovebox. Dip coating is a simple method for the preparation of layers from solvents or dispersion, where a substrate is dipped into the dispersion and withdrawn by a constant speed. The dip coating process can be separated into 5 steps:[82] (i) immersion, (ii) start-up, (iii) deposition, (iv) drainage and (v) evaporation. According to Scriven[82] the resulting film thickness is governed by the competition between 6 forces: (i) the viscous drag upward on the liquid by the moving substrate, (ii) the force of gravity, (iii) the resultant force of surface tension in the concavely curved meniscus, (iv) the initial force of the boundary layer liquid arriving at the deposition region, (v) the surface tension gradient and (vi) the disjoining or con-

joining pressure.[82] Figure 3.8 illustrates the film formation during the dip coating process. The relationship between film thickness d, the withdrawal speed v, the surface tension of the liquid γ, the density of the liquid ρ, the viscosity of the liquid η and the gravity constant g was describe by Landau and Levich as[83]

$$d = 0.94 \frac{(\eta \cdot v)^{2/3}}{(\rho \cdot g)^{1/2} \cdot \gamma^{1/6}} \tag{3.2}$$

Therefore the film thickness of layers can be varied by variation of the withdrawal speed v. Thicker layers are obtained by increasing the withdrawal speed. Surface tension, density and viscosity of the liquid are fixed, but can vary with concentration of QDs. The concentration of QDs in suspension is a factor which is not considered in the equation.

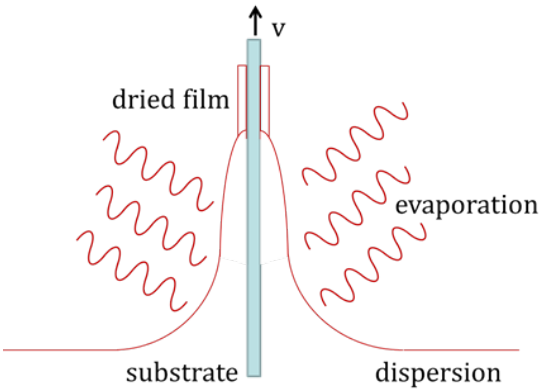

Figure 3.8: Scheme of the film formation during dip coating

3.2.2 Formation of thin homogeneous layers by dip coating

To achieve QD layers with different thickness the withdrawal speed v and the concentration of QDs in suspension were varied. According to equation 3.2 a higher withdrawal should result in thicker layers. Suspensions with different concentrations were prepared by diluting a stock solution with a known concentration. The concentration of the stock solutions was determined by gravimetric analysis of dried QDs or by measuring the absorption of QD suspensions. (CdSe QDs have an absorption coefficient of $1.3 \times 10^7\,\mathrm{m}^{-1}$ at 350 nm.[51]) The concentrations of CdSe QDs in suspensions used for dip coating were varied between 5 and 50 mg/g.

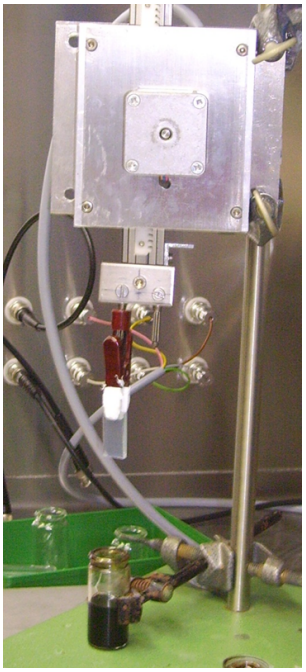

Figure 3.9: Image of the dipping robot.

Substrates (ITO, FTO, Si, SiO_2) used for dipping were cleaned by successive ultra sonication in acetone, ethanol and water for 10 min each. Before dipping they were activated by an argon plasma for 20 min. The layer preparation was done by dipping the substrate into a suspension of CdSe QDs, keeping inside the suspension for 30 s and withdrawal at a defined speed (1, 3 or 5 mm/s). To control the withdrawal speed a dipping robot, which was inside the glove box was used. The dipping robot could be controlled from outside the glove box by a computer. Figure 3.9 shows a picture of the dipping robot with an FTO substrate which is held by a clamp and dipped into the CdSe QD suspension underneath.

Figure 3.10 shows pictures of dip coated layers of CdSe QDs from a suspension of pyridine on ITO. Withdrawal speeds (1, 3 and 5 mm/s) and concentrations (5, 12.5, 25 and 50 mg/g) were varied systematically. The homogeneity and the thickness of layers could be easily seen due to interference effects of reflected light. The layers became thicker with increasing withdrawal speed and higher concentrations. As layers prepared with a pulling speed of 1 mm/s had the best homogeneity, I decided to prepare layers with a withdrawal speed of 1 mm/s with variation of layer thickness by variation of concentration.

Layers of pyridine capped CdSe QDs were both deposited on ITO and FTO substrates. Figure 3.11 shows SEM cross sections of pyridine capped CdSe QDs on FTO and ITO deposited with a withdrawal speed of 1 mm/s from a suspension with a concentration of 25 and 50 mg/g. The roughness of the substrate had a strong influence on the homogeneity of the layer thickness. FTO has a rough surface, therefore the thickness of the layer varied strongly, as seen in the cross sections (figure 3.11 a and b). In between the crystals the thickness of the layers was higher then on top of the crystals (see red errors). Therefore the CdSe QDs mainly filled the voids between the crystals. On the flat ITO substrate a smooth layer with a constant thickness (see figure 3.11 c and d) was present. The layers had a homogeneous thickness and covered the ITO completely. Therefore flat

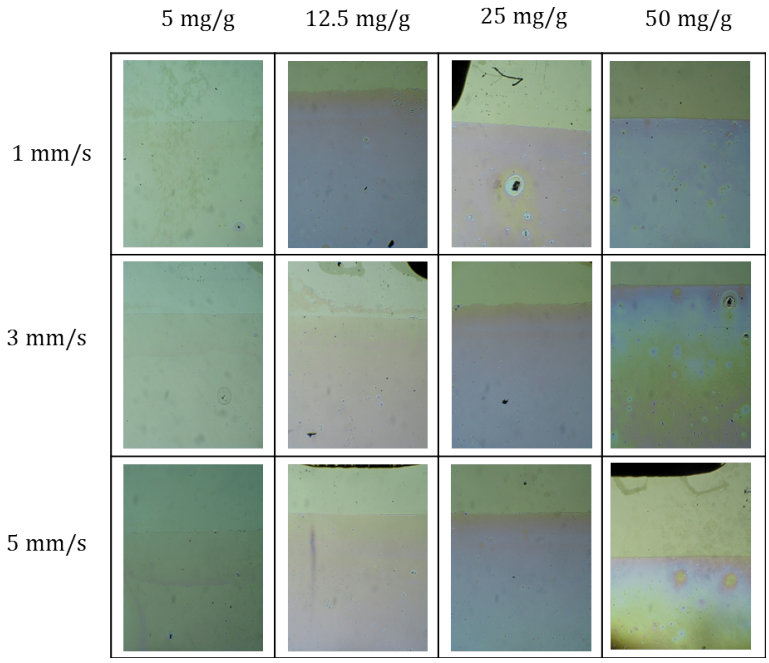

Figure 3.10: Photos of pyridine capped CdSe QD layers on ITO, deposited with different withdrawal speeds and concentrations. The differences in the thickness of the layers can be seen due to interference effects.

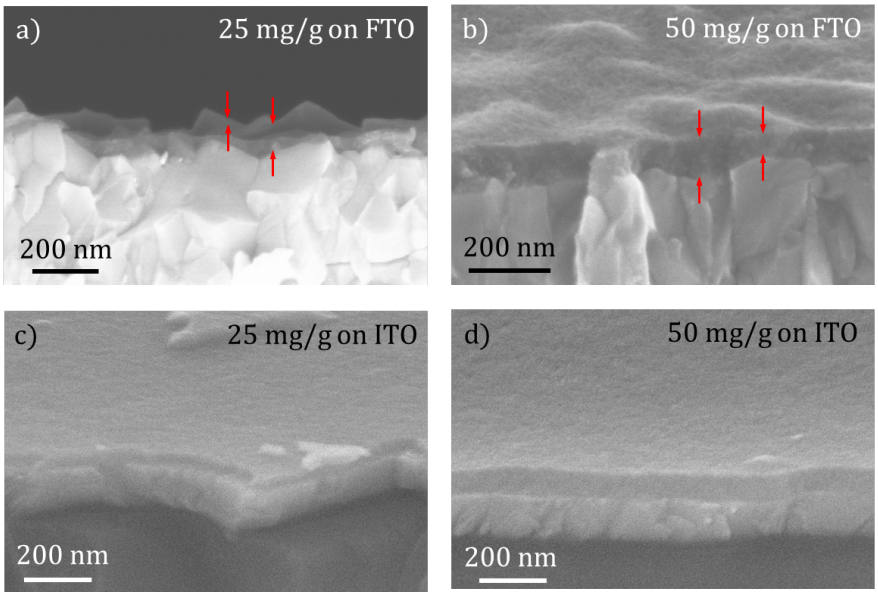

Figure 3.11: SEM cross sections of thin layers of CdSe QDs on FTO (a, b) and ITO (c, d) from a pyridine suspension with a concentration of 25 mg/g (a andc) and 50 mg/g (b and d) (accelerating voltage 5 kV (a and b) and 20 kV (c and d), Zeiss, LEO 1530 GEMINI).

substrates as ITO, Si and SiO_2 were chosen for the deposition of CdSe QDs.

For the measurement of TEM, thin layers of CdSe QDs were prepared on a polymer coated copper grid. The copper grid was therefore dipped in a highly diluted CdSe QD suspension with a concentration of 2.5 mg/g for the preparation of TOP + OA and pyridine capped CdSe QDs. The samples for the TEM measurement of dithiol capped CdSe QDs were prepared by dipping a mica sheet into a pyridine QD suspension with a concentration of 5 mg/g. After the ligand exchange with dithiol (see section 3.1.2) the layer was floated onto water and collected by the copper grid.

3.3 Surface photovoltage

A detailed description of surface photovoltage theory, experiments and applications was published by Kronik and Shapira in 1999.[84] An overview of surface photovoltage on solar cell materials can be found as an extended lecture of Dittrich.[85] Most of the figures in this paragraph were adapted from this lecture.

Surface photovoltage is a method to investigate light induced charge separation in layers. With surface photovoltage, charge separation in single and multiple layers can be measured without the need of contact preparation. Therefore single layers, which can be part of a solar cell can be studied separately. Also mechanisms of charge separation, transport and recombination can be studied. Surface photovoltage can measure charge separation over very short distances, which plays an important role in electronic and photovoltaic devices as well as in molecular and biological systems.[86] Separation of charges were investigated by SPV for example in dye and QD sensitized TiO_2,[87,88] at a CdSe/CdTe QD heterojunction,[42] in porphyrin layers,[89] or in a TiO_2/porphyrin-C_{60}-diade system.[90]

3.3.1 Principles of surface photovoltage

SPV is based on the light induced change of the work function at the surface of a layer. Separation of electrons or holes towards the surface of a layer causes a change in the surface dipole and therefore a change in work function. Figure 3.12 a) illustrates the change of the work function at the surface of a semiconductor

due to a light induced surface dipole. The free charge carriers which are created by photons are separated in space and create a surface dipole. The dipole at the surface cause a change in the workfunction ($e \cdot \Delta V_S$). ΔV_S is the surface photovoltage signal, e the elementary charge .

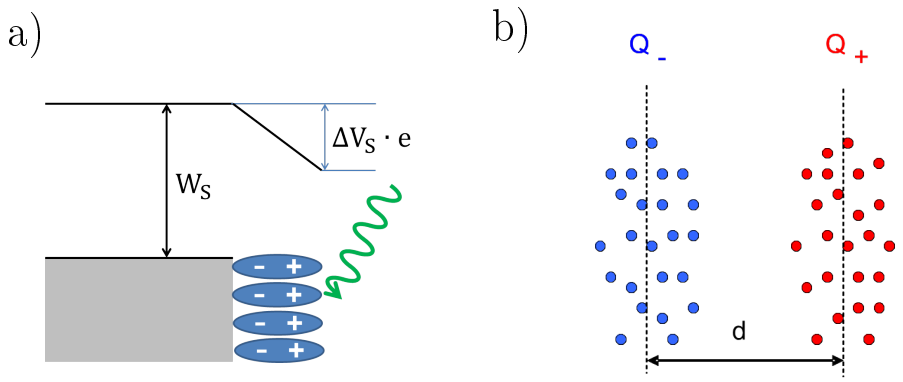

Figure 3.12: a) Change of the work function at the surface of a semiconductor due to a light induced surface dipole; $\Delta V_S \cdot e$ is the change in energy.
b) Influence of the density ($n = Q/e$) and distance (d) between charge carriers on the SPV signal.[85]

The SPV signal ΔV_S is directly proportional to the charge separation length perpencidcular to the sample surface, which is defined as the distance between the centers of positive and negative separated charge carriers with a density of charge carriers $n = Q/e$[91] (see figure 3.12 b and equation 3.3).

$$\Delta V_S = \frac{Q \cdot d}{\varepsilon \cdot \varepsilon_0} \tag{3.3}$$

The two constants ε and ε_0 are the relative dielectric constant of the layer ε and the dielectric constant of the vacuum $\varepsilon_0 = 8.85 \times 10^{-14}\,\mathrm{F/cm}$. Only charge carriers, which are separated in space, are detected. Non separated excitons do not give a SPV signal.

Different processes can lead to a change of the surface dipole by photon-excited charge carriers. Figure 3.13[85,86] depicts some processes leading to charge separation. Examples are an electrical field (e.g. a space charge region), trapping of charge carriers at the surface or an interface, injection of charge carriers into a neighboring layer, internal photoemission, or diffusion. Charges can also be separated by the polarization or restructuring of molecules adsorbed at the surface.

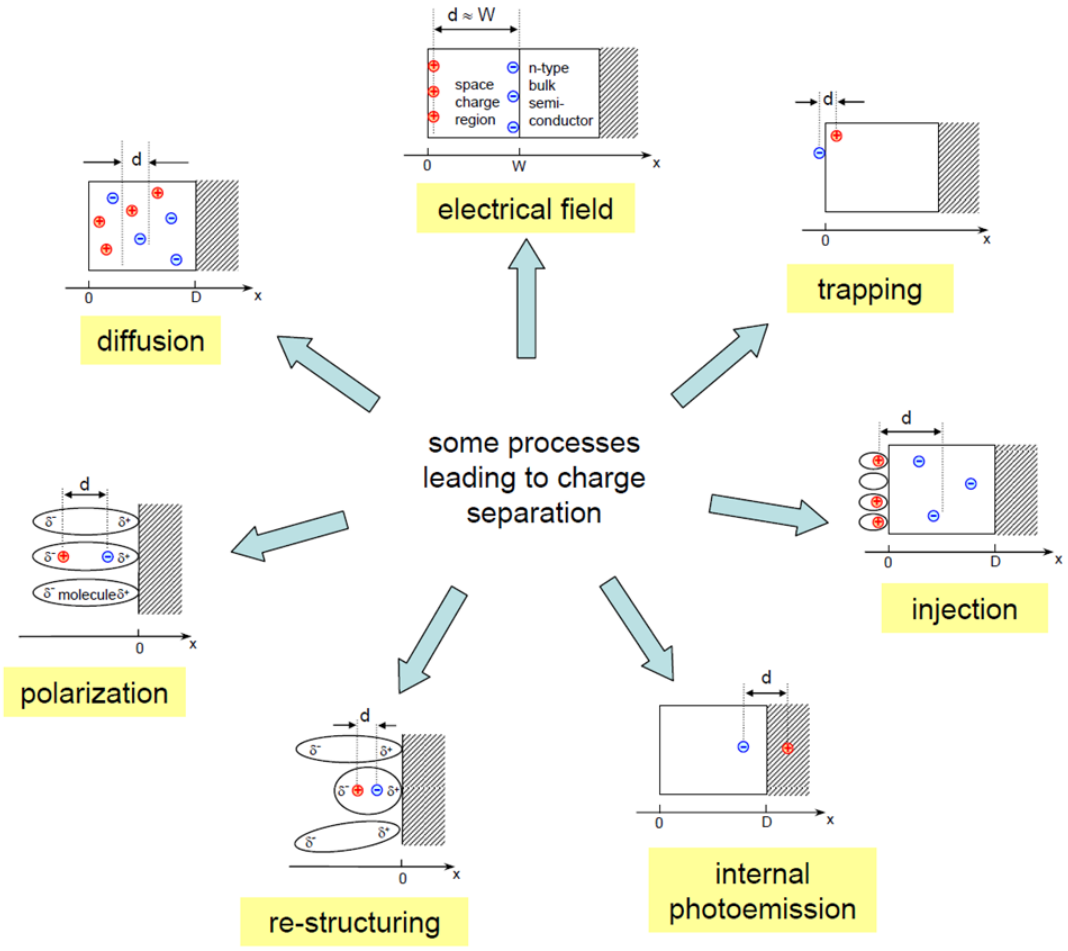

Figure 3.13: Processes leading to charge separation.[85,86]

As an example for charge separation by injection Mora-Seró et al. measured SPV at TiO_2 sensitized with CdSe QDs, where electrons were injected into the TiO_2.[88] Gross et al. measured SPV at a CdTe/CdSe nanoparticle heterojunction, where the electrons were injected into the CdSe nanoparticles and the holes into the CdTe nanoparticles. Diffusion of charges could be monitored in this system by transient SPV.[42]

In CdSe QD layers trapping at the QD surfaces plays an important role for charge separation. Electrons or holes can be trapped at nonsaturated dangling bonds or in traps provided by the ligand. As the SPV signal depends on the distance between charges a symmetrical separation of electrons and holes would not give an SPV signal. The surface of the layer or the interface to the substrate provides an asymmetry in the layer. If electrons or holes go preferentially in the direction of the surface or the interface due to injection, trapping, electrical field, or other mechanisms of charge separation the center of electrons or holes gets closer to the surface/interface and a SPV signal can be measured.

3.3.2 Measurement of surface photovoltage

The change in the surface dipole is measured with a capacitor. Two different setups are used for SPV measurements. The fixed capacitor and the Kelvin probe arrangement. In both arrangements the sample is one of the electrodes of the capacitor. In the Kelvin probe arrangement the second electrode is a vibrating gold mesh. By vibration of the electrode the capacitance C varies and an alternating current (ac) between gold electrode and sample can be measured.[85]

$$I = (CPD - V_b) \cdot \frac{dC(t)}{dt} \tag{3.4}$$

The contact potential difference (CPD) between sample and electrode, which is defined as the difference between the work functions of the sample (W_S) and the electrode (W_{ref}) divided by e. An external voltage V_b is applied at the electrode, which is adjusted to get a zero current (figure 3.14 a). If the measured current is zero CPD equals $-V_b$ and therefore the contact potential difference can be determined (see equation 3.4). A change in surface dipole and therefore work function of the sample results in a change in CPD (figure 3.14 b). The voltage

has to be readjusted to again get a zero current. The change in the applied voltage V_S is equal to $-\Delta CPD$ and is the surface photovoltage signal.

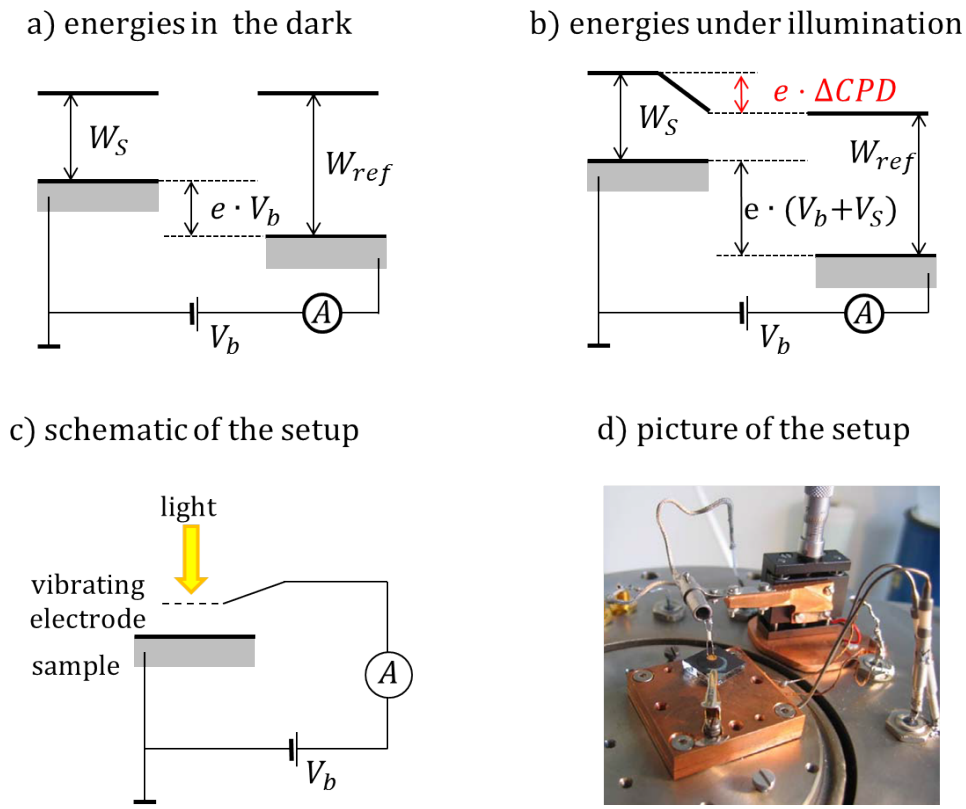

Figure 3.14: The Kelvin probe arrangement; a) and b) illustrate the energies in the dark (a) and under illumination (b) and the measurement principle; c) and d) are a schematic and a picture of the setup.[85]

Figure 3.14 c) and d) shows the setup of the Kelvin probe. The Kelvin probe and the control are a commercial Kelvin Probe S and Kelvin Control 07 from Besocke Delta Phi GmbH. The gold mesh has a diameter of 3 mm and a transparency of 60 %. The vibration of the electrode is controlled by the Kelvin Control 07 via a piezoelectric drive. The amplitude of the vibration can be varied between 0.1 and 2 mm and was set to 0.1 mm, the frequency was $\approx$ 150 Hz. The mean distance between sample and electrode during measurements was adjusted to $\approx$ 1 mm. To account for the work function of gold a voltage offset of 5 V was set. The ac current was measured with a lock in amplifier and automatically adjusted to zero. The time response of the system is in the range of 5 to 10 s and the resolution is

$\approx 1\,\mathrm{mV}$.

In the fixed capacitor arrangement the sample is connected to an electrode via the measurement resistance R_m (see figure 3.15 a and b). Therefore in the steady state the Fermi levels of sample and electrode are aligned. If the sample is illuminated its work function changes and a current flows between the electrode and the sample to realign the Fermi levels. At short times, before the capacitor is discharged a voltage V_S (the SPV signal) is measured at the resistance R_m.

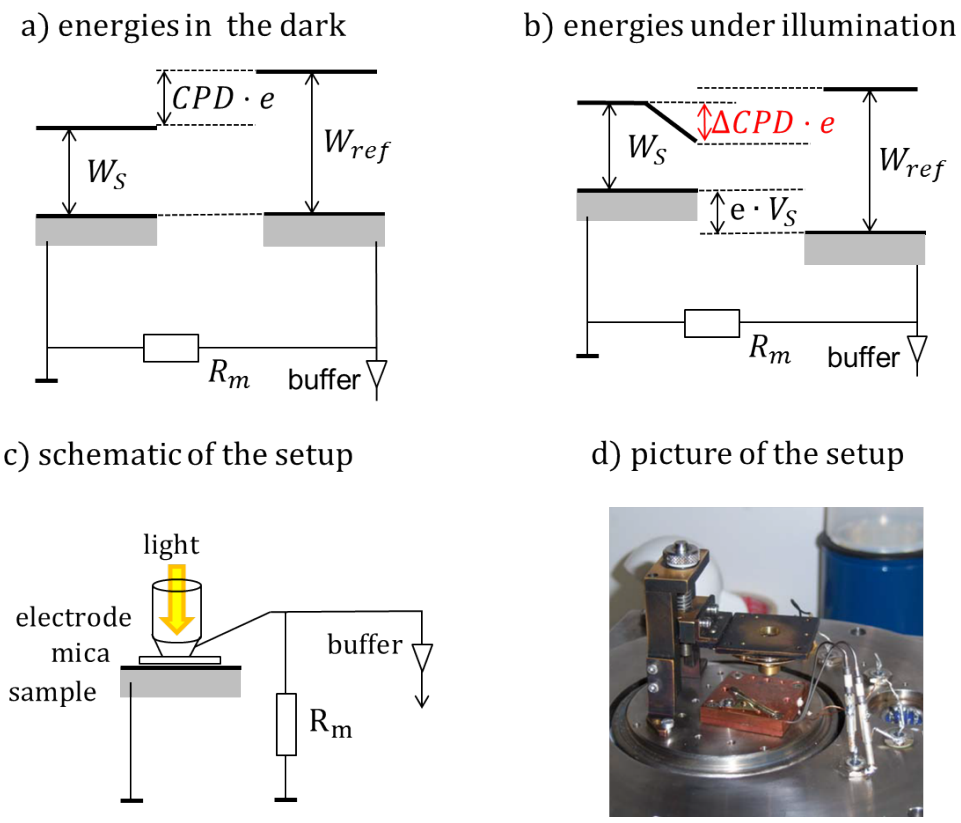

Figure 3.15: The fixed capacitor arrangement; a) and b) illustrate the energies in the dark (a) and under illumination (b) and the measurement principle; c) and d) are a schematic and a picture of the setup.[85]

In the fixed capacitor arrangement (see figure 3.15 c and d) the counter electrode consists of an SnO_2:F coated quartz cylinder with a diameter of 7 mm. As a dielectric spacer a thin mica sheet ($\approx 30\,\mu\mathrm{m}$, $\varepsilon = 6.8$) is placed between sample electrode and measurement electrode. The electrodes are connected via the ground and the measurement resistance R_m . The measurement resistance R_m is $10\,\mathrm{G\Omega}$

and the capacitance of the capacitor C is $\approx 100\,\mathrm{pF}$.

Whereas in the Kelvin probe arrangement the SPV signal is detected in the steady state, in the fixed capacitor arrangement the signal can be only detected before the capacitor is discharged via R_m. The resolution time of the Kelvin probe is given by the lock-in and feed-back and is between 5 and 10 s. In the fixed capacitor arrangement the resolution time at long times is limited by the RC-time constant $R \cdot C \approx 0.1\,\mathrm{s}$. At short times the resolution is limited by the laser pulse (5 ns), the band width of the high impedance buffer (0.5 GHz) and the band width of the oscilloscope (sampling time 10 ns). Transient can thus be measured in a time window between 10 ns and 0.1 s. Additionally spectral dependent modulated measurements are possible.

Figure 3.16 illustrates the setup of the SPV measurements. The lens, the filter wheel and the chopper can be removed from the setup to enable different measurements. As the same setup is used for excitation with the laser and the halogen lamp, the prism can be turned, such that it either guides the light from the halogen lamp, or the laser into the measurement chamber. The intensity of the laser light and the halogen lamp can be reduced by neutral density filters.

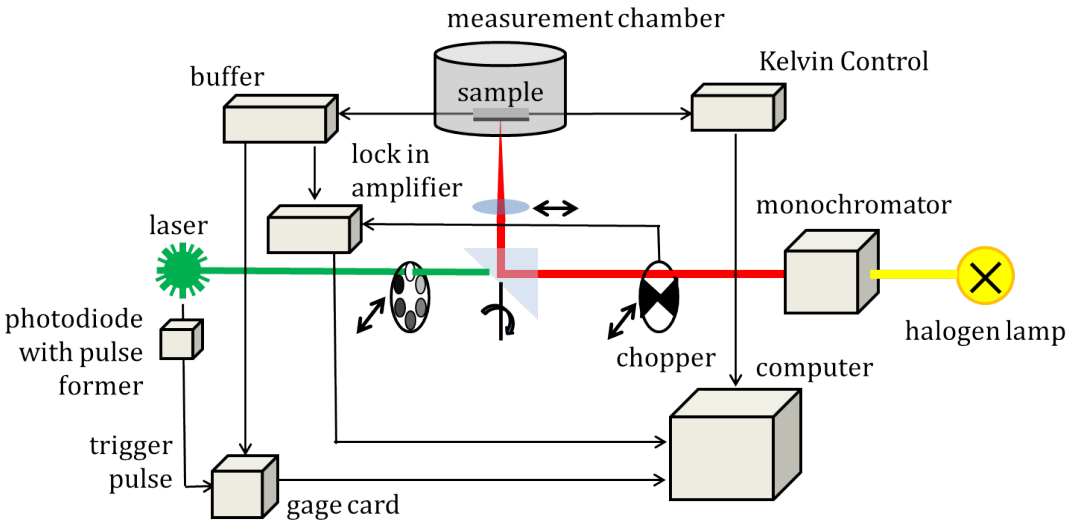

Figure 3.16: Schematic of the SPV setup.

Measurements were done under high vacuum $\approx 1 \times 10^{-5}\,\mathrm{mbar}$. For spectral dependent measurements both the Kelvin probe and the fixed capacitor were used.

In spectral dependent measurements the sample was illuminated with a halogen lamp. The light from the halogen lamp passed through a quartz prism monochromator (Carl Zeiss Jena) and was directed onto the sample by a quartz prism. Before entering the measurement chamber through a quartz window, the light was focused onto the sample with a lens (see figure 3.16). In Kelvin Probe measurements the spot size was between 1 and 3 mm in diameter, for the fixed capacitor the light illuminated the complete area under the quartz cylinder ($d = 7\,\mathrm{mm}$). For Kelvin probe measurements a constant illumination was applied, the measurement was controlled by the Kelvin Control and the CPD signal was read out with a multimeter and registered by a computer.

For modulated SPV measurements in the fixed capacitor arrangement the light was chopped with a frequency of typical 7 Hz. Both, the buffer and the chopper, are connected to a lock in amplifier (EG & G Instruments 7260 DCP). The lock in amplifier measures four different signals. The in phase signal X, the phase shifted signal Y, the amplitude R and the phase Φ. Figure 3.17 illustrates the origin of the X and Y signals. During the measurement there are dark and light phases (figure 3.17 a). The signal (figure 3.17 b) is increasing under illumination and is decreasing in dark. For the X signal the area of the dark phases are subtracted from the illuminated phases. Therefore the signal of the light phase is multiplied by $+1$ and the signal in the dark phase is multiplied by -1 (figure 3.17 c). The resulting signal is displayed in figure 3.17 e). The X signal, measured at the output, is the integral over the product of the measured signal and m_x (figure 3.17 e).

The Y signal is shifted to the illumination by $\pi/2$ (see figure 3.17 d). The signal is multiplied by $+1$ for the second half of the dark phase and for the first half of the light phase. For the second half of the light phase and the first half of the dark phase the signal is multiplied by -1. The resulting signal is displayed in figure 3.17 f). The Y signal measured at the output is the integral over the product of the measured signal and m_y (figure 3.17 f).

A very fast SPV signal, which reaches its maximum instantly during illumination and is also at once zero in the dark phase, has a high X signal and 0 for the Y signal. Whereas a very slow response of charge carrier separation leads to a small or even zero X and a high Y signal. The phase was calibrated with a Si photo

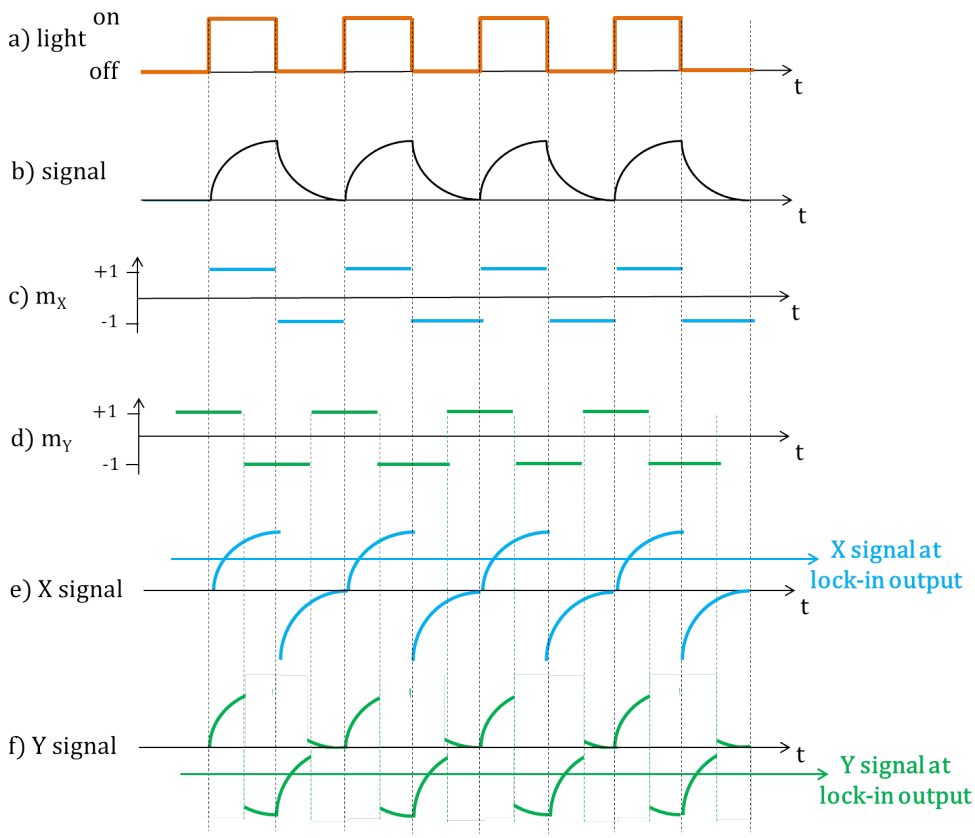

Figure 3.17: Illustration of the origin of the X and Y signal at the lock-in amplifier. a) Shows the dark and illuminated phases, b) the resulting signal. c) and d) show the factors used for multiplication of the signal to obtain the X (e) and Y signal (f), respectively.

diode by setting Y to zero, as the photo diode has a fast response.
The amplitude R is defined as

$$R = \sqrt{X^2 + Y^2} \tag{3.5}$$

The phase Φ gives the relation between X and Y and is defined as

$$\Phi = arctan\frac{Y}{X} \tag{3.6}$$

If a fast charge separation of electrons towards the external surface is present a high negative X signal, a small positive Y signal and a Φ close to 180° were measured. For a slow separation and relaxation of electrons towards the external surface a small negative X and a high positive Y signal were detected, resulting in a phase close to 90°. For separation of electrons towards the internal surface a positive X and a negative Y signal were detected. A fast separation led to a high positive X, a small negative Y signal and a phase approaching 0°. Whereas a slow transport of electrons towards the bulk led to small positive X, a high negative Y signal and a phase close to $-90°$.[92]
SPV transients were measured with a Nd:YAG laser (EKSPLA NT342/1/UVE) in the fixed capacitor arrangement. The Nd:YAG laser was tunable from the UV to infrared range and had a pulse length of 5 ns. Transient measurements were typically recorded with a frequency of 0.2 Hz and averaged over 8 measurements. A high impedance buffer was applied to match the measurement capacitor with the input resistance of the oscilloscope (GAGE oscilloscope compuscope C8-14200) or the lock-in amplifier. The gage card was triggered by the laser through a photo diode and measured 1×10^7 samples with either 10 or 100 mega samples s^{-1}. To reduce the noise of transient measurements a zero illumination transient was recorded before the measurement and subtracted from the measurement afterwards.

3.3.3 Laser intensity and photon density

Typical wavelengths for the excitation of transient SPV were 420, 520, 590 and 640 nm. The intensity of the laser at these wavelengths was both measured with

a laser energy sensor (FieldMax II - P^{TM} from COHERENT) and a pyroelectric detector. Figure 3.18 shows measurements of the laser intensity at 420, 520, 590 and 640 nm with the use of a neutral density filter (NG4, fractional transmission $\approx 10^{-1}$). The measurement was done with a beam splitter and shows fluctuation of light intensity and the differences between the measurement with the laser sensor and the pyroelectric detector. The measurements with the laser energy sensor and the pyroelectric detector did not correlate.

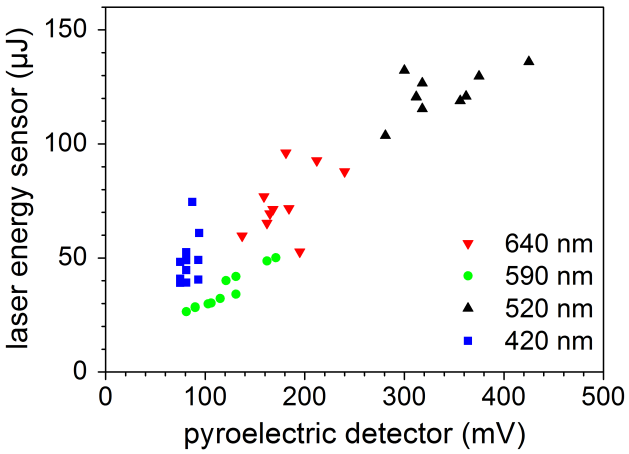

Figure 3.18: Measurement of laser intensity at 420, 520, 590 and 640 nm with the use of the neutral density filter NG4.

The mean laser intensity was determined with the laser sensor, which was placed at the position of the sample and therefore behind the FTO coated cylinder, which served as the electrode during transient measurements. Thus the situation during transient measurements was reproduced and the light intensity at the position of the sample was measured. The laser intensity was varied with the two neutral density filters NG4 (fractional transmission $\approx 10^{-1}$) and NG3 (fractional transmission $\approx 10^{-2}$). To account for the scattering of the laser intensity 10 pulses each were detected. The laser spot on the laser energy sensor had a radius of 3 mm and therefore the following mean values for the laser intensity per pulse were calculated (see table 3.2).

The photon density during spectral dependent measurements was determined by a pyroelectric detector and a Si photo diode. The Si photo diode was placed at the position of the sample under the mica and the electrode and the current at max-

filter	420 nm	520 nm	590 nm	640 nm
no filter	$2.9 \pm 0.5\,\mathrm{mJ/cm^2}$	$4.7 \pm 0.4\,\mathrm{mJ/cm^2}$	$1.5 \pm 0.2\,\mathrm{mJ/cm^2}$	$1.7 \pm 0.3\,\mathrm{mJ/cm^2}$
NG4	$170 \pm 40\,\mu\mathrm{J/cm^2}$	$430 \pm 30\,\mu\mathrm{J/cm^2}$	$130 \pm 30\,\mu\mathrm{J/cm^2}$	$260 \pm 50\,\mu\mathrm{J/cm^2}$
NG3	$12 \pm 2\,\mu\mathrm{J/cm^2}$	$29 \pm 4\,\mu\mathrm{J/cm^2}$	$13 \pm 2\,\mu\mathrm{J/cm^2}$	$17 \pm 4\,\mu\mathrm{J/cm^2}$

Table 3.2: Mean laser intensity with standard deviation measured with laser energy sensor.

imum illumination at 550 nm was measured. From the photo current of 0.73 µA and the area of the photo diode of 4 mm^2 a photon density of 1.1×10^{14} s^{-1}cm^{-2} was determined. The relative intensities were afterwards determined by a pyroelectric detector and calibrated by the known photon density. Figure 3.19 shows that the photon density varies over four orders of magnitude in the measurement range. The highest photon density of over 1×10^{15} s^{-1}cm^{-2} is measured around 1 eV. Above 3.5 eV the photon density drops below 1×10^{12} s^{-1}cm^{-2}. As the SPV signal is not linearly dependent on the photon density, SPV spectra could not be normalized to the photon flux.

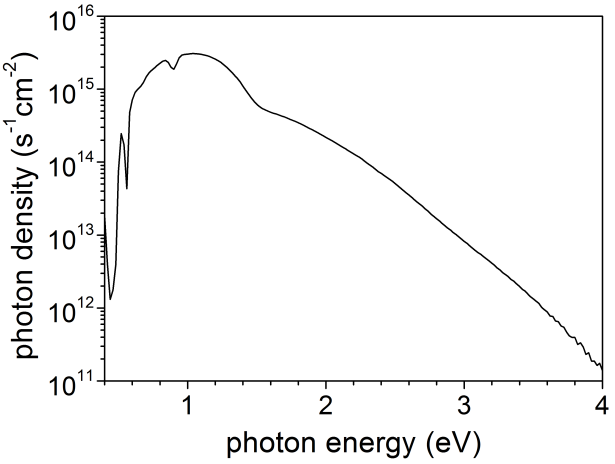

Figure 3.19: Photon density during spectral dependent measurements.

To vary the light intensity two filter wheels with different neutral density filters were combined. Filter wheel 1 had six filters with nominal fractional transmissions of $10^{-0.04}$, $10^{-0.5}$, 10^{-1}, $10^{-1.5}$, 10^{-2} and $10^{-2.5}$. Filter wheel 2 had six filters with nominal fractional transmissions of $10^{-0.04}$, $10^{-0.1}$, $10^{-0.2}$, $10^{-0.3}$, $10^{-0.4}$ and $10^{-0.5}$. The real transmission of the filter combinations were determined at the

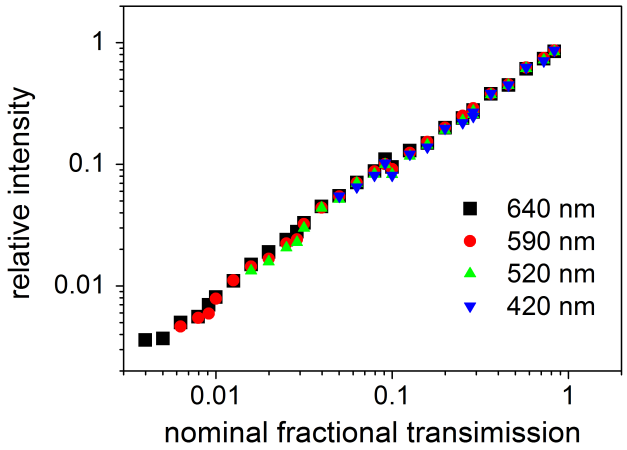

Figure 3.20: Relative light intensity at 640, 590, 520 and 420 nm using the filter wheels.

different wavelengths using the halogen lamp, the monochromator and the pyroelectric detector. Therefore the light intensity used for excitation during SPV measurements was known and tha dependency of SPV amplitudes on photon density could be determined. Figure 3.20 shows the relative light intensities at 640, 590, 520 and 420 nm plotted against the nominal fractional transmission of the filter combinations. For the higher density filters the intensities at higher photon energies were too low to be detected.

3.4 UV-vis absorption spectroscopy

The decrease of the light intensity in an absorbing medium is described by the Lambert Beer law.

$$I_T = I_0 e^{-\alpha d} \tag{3.7}$$

It describes the intensity of the light I_T after crossing a medium with an absorption coefficient α and a thickness d. The law of Lambert Beer can be used to determine either the absorption coefficient α or the thickness d, given that the other constant is known. For the determination of α and d in thin layers we have to consider

reflection next to transmission. The intensity of the light used to excited the sample is defined as one. The light which is not reflected and travels through the sample has an intensity $I_0 = 1 - R$. The ratio of the intensity of the transmitted light I_T, after passing a sample with a thickness d, and the illumination intensity I_0 is equal to the transmission T. Therefore we can calculate the absorption coefficient α from the transmission T and the reflection R[93]

$$\alpha = \frac{1}{d} ln \frac{1-R}{T} \tag{3.8}$$

By measurement of the wavelength dependent absorption coefficient $\alpha(\lambda)$ the electronic states of a material can be determined. Absorption of light takes place only if the energy of the incoming photon is equivalent to an allowed transition of an electron from a ground state to an excited state. Therefore wavelegth of possible transitions can be determined by UV-vis.

UV-vis measurements of thin films were done with an integrating sphere. The inside of the integrating sphere is covered with a white layer which scatters the light in the whole measurement range. Therefore also light that was scattered at the sample reaches the detector and is measured. A halogen lamp and a xenon lamp were used as a light source. The setup was calibrated by measuring in the transmission and reflection mode at 100 % and 0 % intensity. The corrected transmission T was then calculated from the measured transmission T_m the 100 % transmission $T_{100\,\%}$ and the zero transmission $T_{0\,\%}$.

$$T = \frac{T_m - T_{0\,\%}}{T_{100\,\%} - T_{0\,\%}} \tag{3.9}$$

The same procedure was applied for reflection measurements.

UV-vis measurements were performed on thin layers of QDs on SiO_2 and ITO substrates. The transmission, reflection and absorption of the quartz and ITO substrates is shown in figure 3.21. As SiO_2 has no absorption and a reflection below 10 % in the visible range, it is preferentially used as a substrate for absorption measurements. We additionally used ITO substrates for UV-vis measurements as it enabled us to use the substrates both for UV-vis as well as for SPV measurements. As the ITO absorbs strongly at wavelengths lower than 400 nm absorption measurements below 400 nm were not possible on ITO substrates.

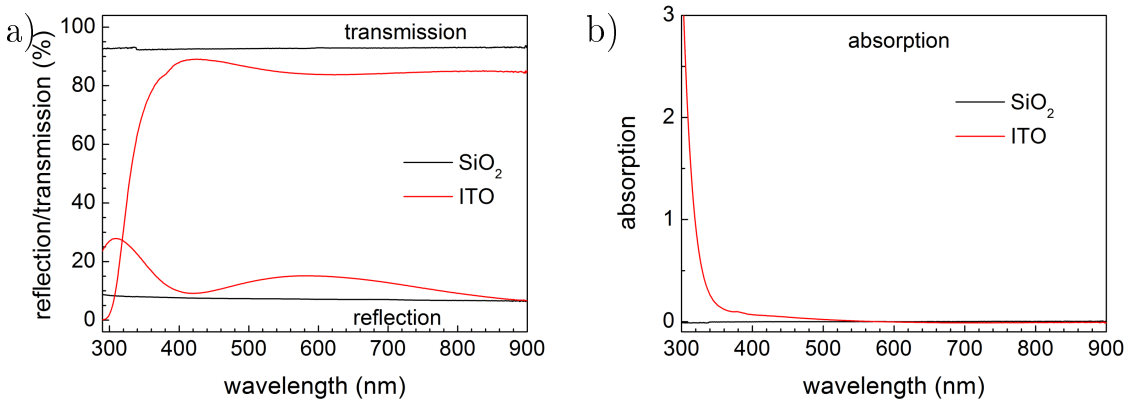

Figure 3.21: Optical properties of SiO_2 and ITO substrate; a) reflection and transmission; b) absorption.

QDs in suspensions were measured in quartz cuvettes. In the case of suspension the reflection was not measured. The transmission was corrected by using a quartz cuvette filled with the corresponding solvent as reference for the 100 % transmission measurement.

3.5 Photoluminescence

Photoluminescence (PL) as a method is complementary to SPV. In SPV only separated charge carriers are measured, whereas in PL those which recombine radiatively are detected. For PL measurements electrons are excited by a laser, with a photon energy higher than the transitions studied and the photons emitted by the sample are detected. In PL both, allowed and forbidden transitions, can be studied. The forbidden transitions require a change in spin and therefore have a longer life time (phosphorescence) than the allowed transitions (fluorescence).

Excitation of electrons is either done by a continouswave or pulsed laser. By using a constant light source the PL is measured in a steady state condition. If a pulsed excitation is used PL transients can be recorded and therefore the dynamics of charge recombination is observed. Additionally the pulsed excitation has the advantage of a high sensitivity, as a laser with a high intensity could be used. The thermal impact of the excitation at the same time was low as a frequency of 1 Hz was applied. Layers of CdSe QDs were measured, by pulsed and constant excitation.

For PL measurements with constant illumination the intensity of the illumination and the temperature could be varied. A temperature of 4 K was used to suppress thermally activated trapping of charge carriers and nonradiative recombination by thermal relaxation. Therefore the intensity of the PL signal was increased and PL could be also measured on quantum dots with a high density of defects, which showed no detectable PL signal at RT.

The setup of the measurement of pulsed PL is illustrated in figure 3.22. A pulsed nitrogen laser (LSI VSL-337ND-S) with an energy density of 1 mJ/cm^2, a pulse length of 5 ns and a wavelength of 337 nm was used for pulsed excitation. The light was focused onto a sample in a high vacuum (1×10^{-5} mbar) measurement chamber. The emitted PL light from the sample was collected by a lens. The PL intensity at a given wavelength was measured with an avalanche photodiode with a preamplifier (bandwidth 15 MHz). The spectral dependent measurements were performed with a quartz prism monochromator detecting the signal at the time of 20 ns (peak maximum).

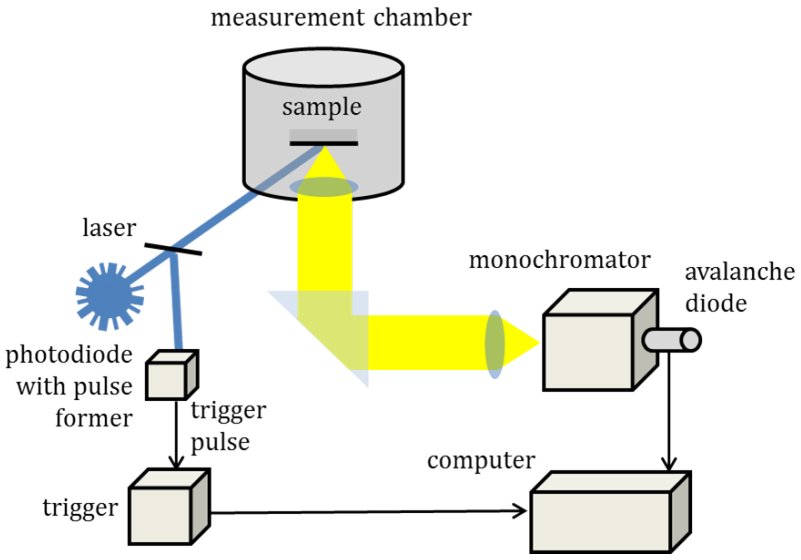

Figure 3.22: Schematic of the pulsed PL setup.

The transmission function of the monochromator was obtained with a halogen lamp and a pyroelectric detector (see figure 3.23 a). The time response of the avalanche diode was in the range of 20 ns (see figure 3.23 b). Therefore only processes that are slower than 20 ns could be time resolved. For pulsed excited PL

measurements three different substrates were used, silicon, ITO and SiO_2 (which was placed on a Si substrate during PL measurements as it was transparent for the laser light). All substrates showed a PL emission in the measurement range (see figure 3.23). Silicon showed a broad peak around 1100 nm, but no signal in the region where the excitonic transition of CdSe QDs was expected. ITO had a broad emission over the complete measurement range. For quartz the detected signal was slightly smaller than for ITO. Additionally the Si peak of the Si substrate underneath the sample was detected.

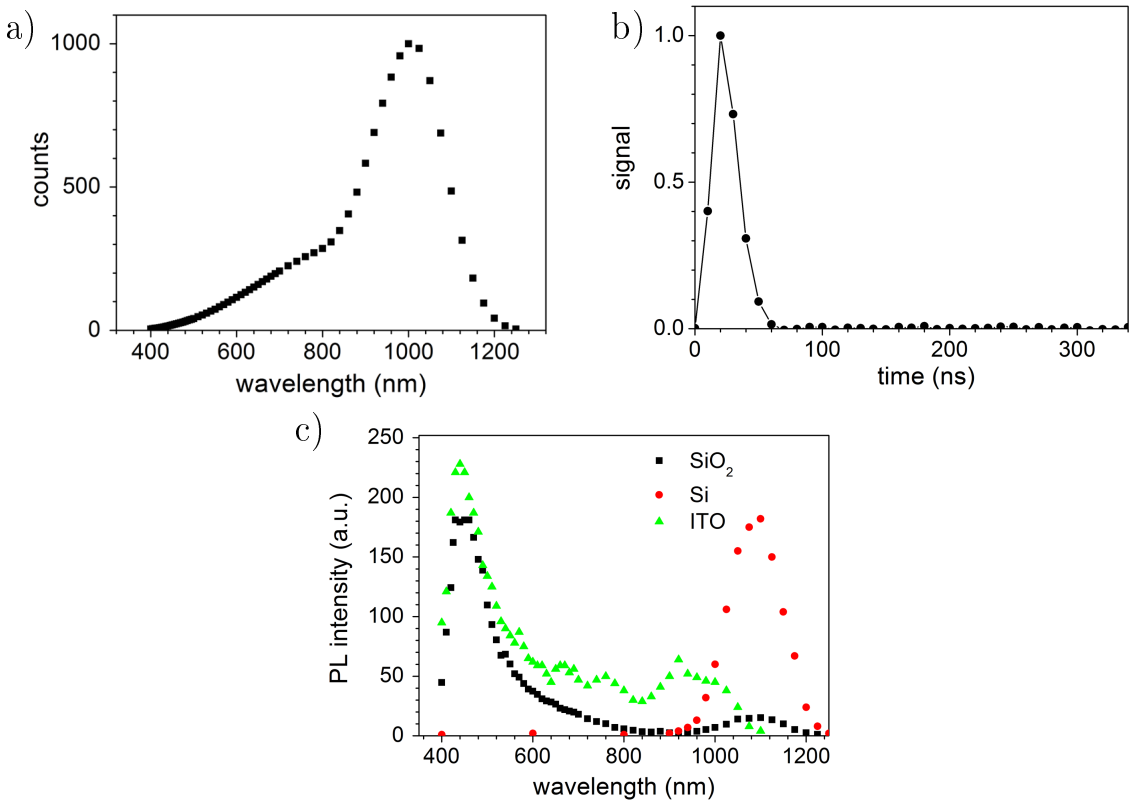

Figure 3.23: Characteristics of the pulsed PL measurements and PL signal of substrates. a) Transmission function of the monochromator. b) Time response of the avalanche diode. c) PL signal of the substrates (these spectra were not corrected to the transmission function).

For the measurements with constant illumination a He-Cd-Laser (KIMMON ELECTRIC IK561R-G) with a wavelength of 325 nm was used. The power of the laser was varied between 0.1 and 7.5 mW. The sample was placed inside a He flow cryostat (Oxford Instruments, Variox) suitable for temperatures down to 4 K.

The focused laser light has a spot size of 300 µm in diameter. The emitted PL light was collected by two off-axis parabolic mirrors where reflected light, arriving from the exciting laser light, was absorbed by an edge filter and the PL light was focused onto a UV-vis optical fiber. The optical fiber was connected to a Czerny-Turner imaging spectrograph (Andor Technologies, Shamrock 303) attached to a Si-CCD camera (Andor iDus DU 401-BR-DD). The spectrograph/detector set-up covered a wavelength range between 200 and 1000 nm and had a spectral resolution of ≈ 0.7 meV.[94,95] For the PL measurements with constant illumination Si substrates were used, as they did not show any PL signal at used cw excitation.

3.6 Rutherford-Backscattering Spectrometry

Rutherford-Backscattering Spectrometry (RBS) was applied to gain information about stoichiometry and absolute amount of Cd and Se atoms in CdSe QD layers. The sample was probed by high energy ions (in the MeV range) which are elastically backscattered by the nuclei in the sample. RBS is a quantitative and nondestructive method without the need of references. It has a high sensitivity towards heavy atoms and a probe depth of up to ≈ 2 µm for incident given He-ions. In RBS the number of backscattered ions at a certain energy is determined to get information about the areal density of a certain element and its depth profile. The energy E_1 of backscattered ions from the surface is given by its incident energy E_0 and the kinematic factor K.

$$E_1(0) = KE_0 \tag{3.10}$$

The kinematic factor results from the conservation of energy and moment of a two-body collision and thus depends on the mass of the projectile M_1 the mass of the target nucleus M_2 and the scattering angle θ. For $M_1 < M_2$ the kinematic factor is given by[96,97]

$$K = \frac{M_1^2}{(M_1 + M_2)^2} \left(cos\theta + \sqrt{\left(\frac{M_2}{M_1}\right)^2 - sin^2\theta} \right)^2 . \tag{3.11}$$

Ions scattered by non-surface atoms loose energy due to interactions with electrons

and nuclei and thus have a lower energy than ions scattered at the surface. For normal incidence, ions scattered from a depth z have an energy of[98]

$$E_1(z) = KE_0 - z\left(S(E_0)K + \frac{S(E_1)}{cos\theta}\right), \tag{3.12}$$

where $S(E_0)$ and $S(E_1)$ are the stopping powers of the ions at the energies E_0 and E_1, respectively. To determine the areal density of an element in a layer the cross-section for backscattering has to be known. The Rutherford cross section σ_R depends on the backscattering angle, the masses and the charges (Z_1 and Z_2) of the projectile and the target nucleus.[96]

$$\sigma_R = 5.1837 \times 10^6 \left(\frac{Z_1 Z_2}{E_0}\right)^2 \frac{\left(\sqrt{M_2^2 - M_1^2 sin^2\theta} + M_2 cos\theta\right)^2}{M_2 sin^4\theta \sqrt{M_2^2 - M_1^2 sin^2\theta}} \tag{3.13}$$

σ_R has the unit $10^{-27} cm^2/sr$ and E_0 is given in keV.

RBS was measured at the Tandetron accelerator JULIA of the University Jena with the help of PD. Dr. Elke Wendler. For the measurements He^+ ions with an energy of 1.4 MeV, a backscattering angle of 168° and a solid angle Ω of 5.45 msr were used. The measurement charge Q and current were 5 µC and 8 nA, respectively.

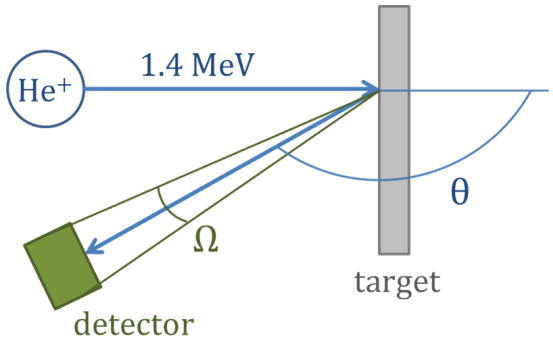

Figure 3.24: Schematic of the RBS setup, showing the backscattering angle θ and the solid angle Ω.

The areal densities were determined by simulation with the WiNDF program.[99] The simulations are based on the equation by Chu et al. which gives an approximation for the backscattering cross section for large backscattering angles and

$M_1 << M_2$[100]

$$\sigma_R \approx 0.02073 \left(\frac{Z_1 Z_2}{4E_0}\right)^2 \left[sin^{-4}\left(\frac{\theta}{2}\right) - 2\left(\frac{M_1}{M_2}\right)^2\right] \tag{3.14}$$

and the relationship between the areal density AD and the area A under the peak[101]

$$A = Q\Omega\sigma_R AD. \tag{3.15}$$

Equation 3.15 was taken into account because it applies for thin samples as was for our case. In the RBS spectra the counts are plotted versus the channels. The conversion from channels (ch) into energy is $E = 2.92\,\mathrm{keV} \cdot (ch + 17.66)$.

4 Results and Discussion

4.1 Morphology, thickness and absorption of QD monolayer systems

The absorption of QD layers depends on the thickness, the morphology and the electronic properties of QD layers. For the analysis of SPV results in the following sections the morphology, thickness and absorption of QD layers needs to be known. The CdSe QD samples differ in two ways, (i) the surfactant and (ii) the thickness of the samples prepared (figure 4.1). By variation of the surfactant different parameters are changed which are (i) the interparticle distance between QDs, (ii) the dielectric surroundings and (iii) the electronic states on the surface of QDs. Whereas the first and the second factor strongly influence the absorption of light the third factor mainly change the charge carrier dynamics of excited electrons and holes. The thickness of the surfactant shell will determine the packing of QDs and therefore the fraction by which the layer consists of CdSe.

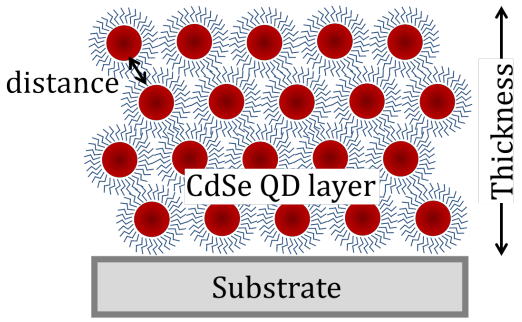

Figure 4.1: Scheme of the factors determining the absorption in CdSe QD layers.

The thickness of the QD layers can differ depending on the concentration of particles in the suspension, the suspension and the substrate used. Thicknesses of

CdSe QD layers were determined in different ways. The absolute thickness was either determined by a step profiler or by SEM cross sections. Both methods are subject to a certain error. In the measurements with the step profiler a tip is pressed onto the sample. As our QD layers are relatively soft the thickness of the layers is thus reduced during the measurement. For the SEM measurement the sample is broken to create a cross section. As the cross section does not break perfectly perpendicular to the substrate, the thickness measured in SEM will be higher than the true thickness. Furthermore only layers prepared on a conductive substrate can be measured in the TEM due to charging of the sample. On the other hand measurement with the step profiler are only possible if the layer is not too soft and the adhesion between substrate and QD layer is high enough.

For the determination of the composition of CdSe in the CdSe QD layers RBS was used. For the measurement of RBS thin layers of CdSe QDs were prepared on Si and SiO_2 as they do not have any additional elements interfering with the Se and Cd peak.

4.1.1 Interparticle distances between CdSe QDs by TEM

The interparticle distance between CdSe QDs in layers with different surfactants was determined by TEM. Figure 4.2 shows transmission electron micrographs of (sub-)monolayers of CdSe QDs stabilized with (i) TOP + OA pristine, (ii) TOP + OA washed, (iii) pyridine and (iv) dithiol molecules. The diameter of QDs measured from TEM images was 4.5 ± 0.5 nm. The micrographs reveal a relative constant interparticle distance for each kind of ligand. Distances between QDs were determined by measuring the distance between centers of QDs. The pristine OA + TOP capped QDs show a regular hexagonal arrangement with a distance of 7.7 ± 0.2 nm between centers of QDs. For the washed TOP + OA QDs the distance was clearly reduced to 6.2 ± 0.2 nm, the hexagonal ordering was still present. In the CdSe pyridine QD layer the distance was further reduced to 5.6 ± 0.3 nm, while hexagonal ordering was lost. For the ligand exchange with dithiol there was no distinct decrease in the average distance compared to pyridine CdSe QDs, but a slightly higher distribution of distances than for the pyridine QDs (5.5 ± 0.4 nm). The dithiol molecule can bind to two neighboring QDs what reduces the interparticle distance of these bridged QDs but also increased the distances between

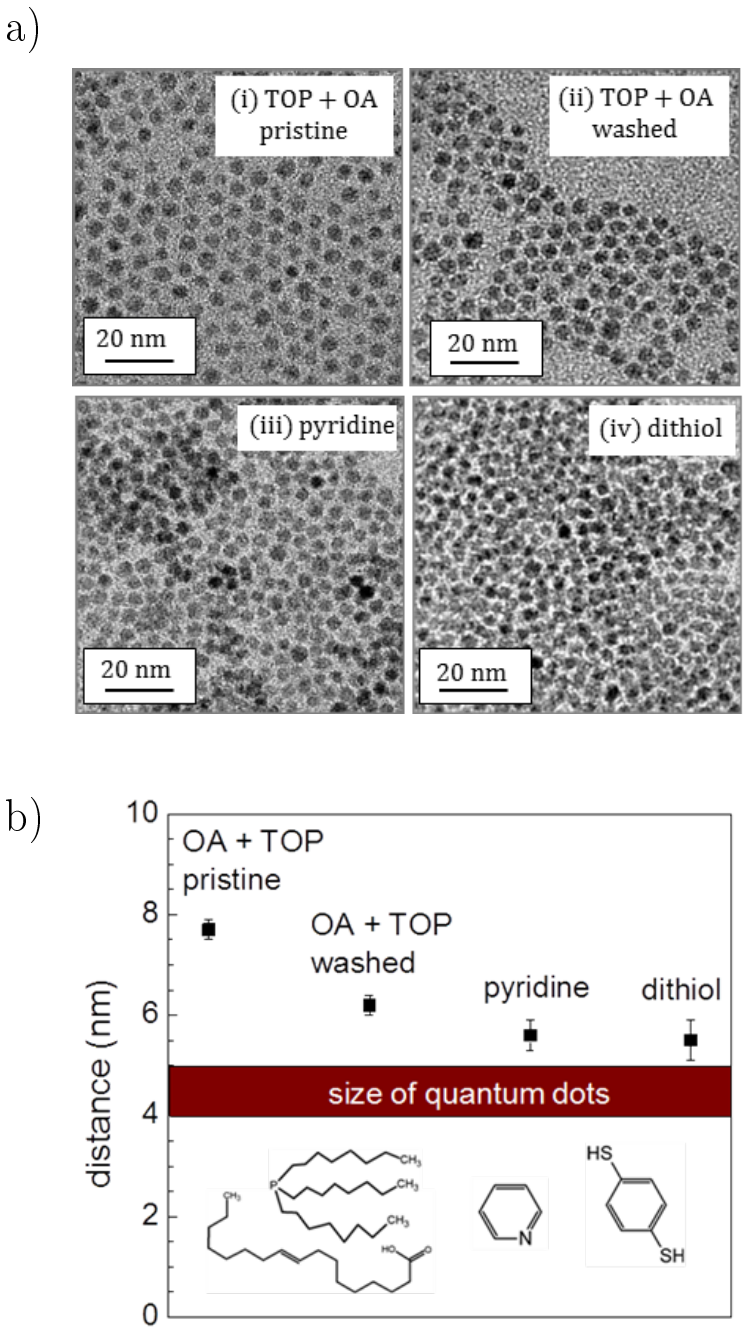

Figure 4.2: a) TEM images of CdSe QD (sub-)monolayers with different surfactants (accelerating voltage 120 kV, Philips CM12/STEM, LaB6 kathode); b) determination of interparticle distances from transmission electron micrographs.

non-bridged QDs. As this exchange was done in a layer, a decrease of interparticle distance in one place must be compensated by an increase of interparticle distance in another place.

4.1.2 Areal densities and number of monolayers determined by RBS

RBS was used to determine the areal density of CdSe in CdSe QD layers. Therefore layers with pyridine capped CdSe QDs from suspensions with different concentrations (5, 10, 15, 20 and 25 mg/g) were prepared on Si and SiO_2. Figure 4.3 a) and b) show the RBS spectra of CdSe QDs on Si and SiO_2. The Cd peak is located between channels 415 and 440, the Se between channels 385 and 414. The Si peak starts around 285.

Figure 4.3 c) and d) displays a zoom in of the RBS measurements of the Cd and Se peak and the corresponding simulations of the spectra for a given density distribution. From the simulations the areal densities were calculated and plotted versus the concentration of QD suspensions (figure 4.3 e). The substrate did not influence the areal density of the CdSe QD layers. The areal densities of Cd and Se were equal. Therefore the QDs have a stoichiometry of Cd:Se of 1:1. At low concentrations (5 to 15 mg/g) the areal densities were linearly dependent on the concentration. Considering only the areal densities at 5, 10 and 15 mg/g an areal density of $(1.3 \pm 0.1) \cdot 10^{15}$ per mg/g was found. At higher concentrations (20 and 25 mg/g) the areal densities are higher than expected from the linear fit (see figure 4.3 e). The increase in thickness could be for example due to a change in viscosity of QD suspensions at high concentrations.

Knowing the average distance between pyridine capped CdSe QDs (see figure 4.2) the number of monolayers can be calculated from the areal density. The areal density per monolayer is

$$AD_{ML} = d_{cp} \cdot \frac{V_{QD}}{V_{QD+S}} \cdot \frac{\rho_{CdSe} \cdot N_A}{M_{CdSe}} \cdot h_{ML} \tag{4.1}$$

where $d_{cp} = \pi/3\sqrt{2}$ is the space filling of closed packed spheres, $V_{QD} = 4/3\pi \cdot (2.25\,\mathrm{nm})^3$ is the volume of the QD core, $V_{QD+S} = 4/3\pi \cdot (2.8\,\mathrm{nm})^3$ is the volume of

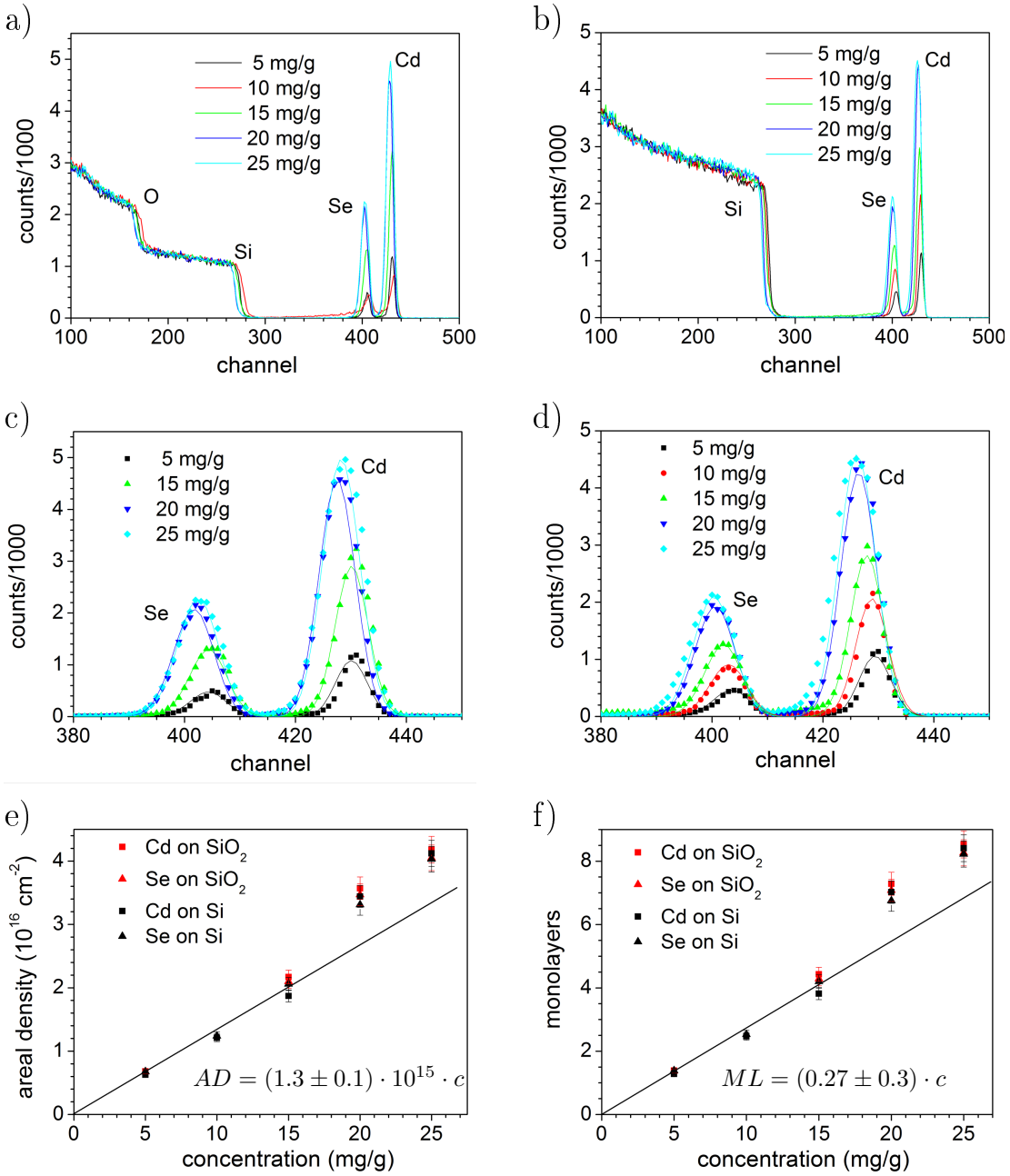

Figure 4.3: RBS measurement of CdSe (pyridine) QDs on a) SiO_2 and b) Si. c) and d) show a zoom in of the RBS measurement of the Cd and the Se peak (scatter) plotted together with the simulation (line) on SiO_2 and Si. The diagrams in e) and f) show the dependence of areal density and number of monolayers on the concentrations of the QD suspension.

the QD including the surfactant shell, $\rho_{CdSe} = 5.81\,\mathrm{g/cm^3}$ is the density of CdSe, $N_A = 6.022 \times 10^{23}\,\mathrm{mol^{-1}}$ is the Avogadro constant and $M_{CdSe} = 191.36\,\mathrm{g/mol}$ the molar mass of CdSe. For h_{ML}, which is the height of a single monolayer, the diameter plus twice the thickness of the surfactant shell was used, which is 5.6 nm. Therefore an areal density of $4.9 \times 10^{15}\,\mathrm{cm^{-2}}$ per monolayer results. In figure 4.3 f) the as calculated numbers of monolayers are plotted against the concentration of the suspensions. The relation of number of monolayers and the concentration of QD suspensions, at low concentration (5 to 15 mg/g), was $ML = 0.27 \pm 0.3$ per mg/g concentration (see figure 4.3 f) The thicknesses of the CdSe QD layers range from 1.4 MLs for a concentration of 5 mg/g up to 8.4 ML for 25 mg/g. Thus layers as thin as a monolayer could be prepared by dip coating.

4.1.3 UV-vis absorption of CdSe QD monolayer systems

The absorption of the CdSe QD layers on SiO_2 was determined by UV-vis spectroscopy. Knowing the areal density and the thickness of these layers in MLs, the absorption per ML could be determined from these layers. CdSe QD layers on ITO were additionally prepared and measured. The determination of absorption and thickness of layers on ITO was important, as ITO was used as substrates for SPV measurements. Figure 4.4 a) and b) show transmission and reflection of CdSe QD layers on SiO_2 and ITO, including the spectra of the substrate. For CdSe QDs on SiO_2 less than 25 % of the light was reflected in the spectral range between 200 nm and 900 nm. In the transmission the first excitonic peak around 600 nm could be seen. The transmission went down to 9 % at 200 nm for the thickest QD layer. For CdSe QD on ITO a more pronounced reflection was observed. The ITO substrate showed reflection peaks around 310 nm and 585 nm. These peaks were shifted to higher wavelength with increasing QD layer thickness. For the thickest layer the peak maxima were located at 410 and 770 nm. In the transmission spectra the first excitonic peak around 600 nm could be seen, as already observed for CdSe QDs on SiO_2. The transmission dropped to zero around 300 nm due to strong absorption by the ITO in this region (see also figure 3.21).

Figure 4.4 c) shows the absorption of the CdSe QD layers on SiO_2 and ITO. All spectra had the maximum of the first excitonic peak at 599 ± 1 nm. For layers prepared from suspension with a low concentration (5 to 15 mg/g) the

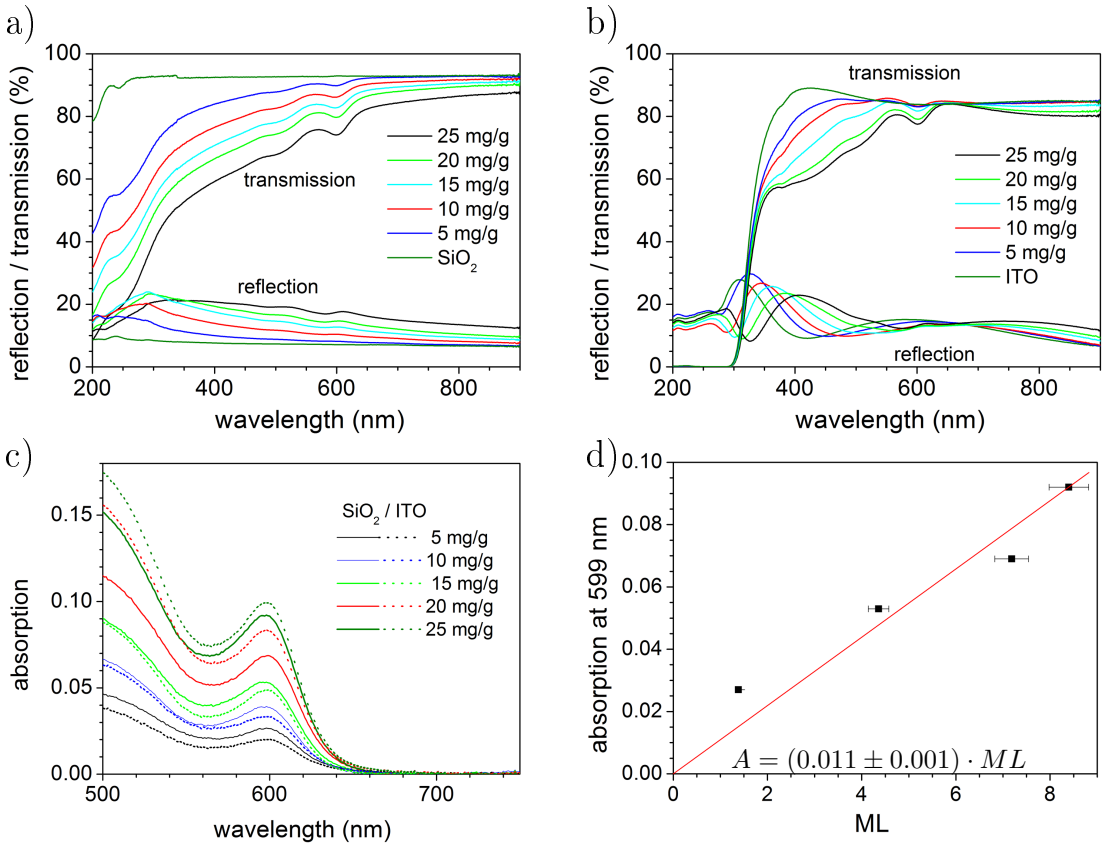

Figure 4.4: UV-VIS measurements of layers of CdSe QDs with different thicknesses. a) transmission and reflection on SiO_2, b) transission and reflection on ITO, c) absorption of CdSe QDs on ITO and SiO_2 (the absorption of the ITO substrate was subtracted) d) correlation of absorption at the first excitonic peak and number of MLs determined by RBS of CdSe QDs on SiO_2.

absorption on SiO_2 was slightly higher, whereas for the higher concentrations (20 and 25 mg/g) the absorption on ITO was higher. The number of monolayers calculated from RBS were plotted against the absorption measured at 599 nm for CdSe QD layer on SiO_2 (see figure 4.4 d). From this plot the absorption per monolayer could be extracted from a linear fit. An absorption of 0.011 ± 0.001 per monolayer at 599 nm was found. Form this factor and the measurement of the absorption (figure 4.4 c) the number of monolayers on ITO were determined. The resulting thicknesses on ITO were 1.8 ± 0.2, 3 ± 0.3, 4.5 ± 0.5, 7.6 ± 0.8 and 9.0 ± 0.9 monolayers for 5 mg/g, 10 mg/g, 15 mg/g, 20 mg/g and 25 mg/g respectively.

4.1.4 Determination of CdSe QD layer thickness by step profilometry

The thicknesses of CdSe QD layers on ITO were determined with a step profiler. For the measurement the samples were scratched with a non hardened steel needle at 2 different places and the thickness was determined at ten different places.

In figure 4.5 the determined thicknesses is plotted against the concentration (a) and the calculated number of monolayers (b). Thicknesses determined from the step profiler were (8 ± 1)nm, (16 ± 1)nm, (26 ± 3)nm, (33 ± 3)nm and (46 ± 3)nm for 5 mg/g, 10 mg/g, 15 mg/g, 20 mg/g and 25 mg/g respectively. Note that the thickness measured with the step profiler might be smaller than the real thickness as a tip was press onto the soft layer during the measurement. From a linear fit of the MLs (determined from UV-vis) versus the step profiler thicknesses a correlation of (5.2 ± 0.2)nm (D_{SP}) per monolayer was derived.

For the comparison of QD layers with different surfactants additional sets of samples on ITO were prepared. In figure 4.6 the thicknesses of layers from TOP + OA washed, pyridine and dithiol capped QDs are plotted against the concentration (5, 12.5, 25 and 50 mg/g). For comparison the thicknesses determined from the samples used for the previous measurement were inserted (pyridine 1). The thicknesses of these samples are approximately 1.5 times higher than those from the new measurements (pyridine 2).

Different factors can lead to this deviation. First the determination of the concentration is problematic. For the three new plots shown in the diagram the

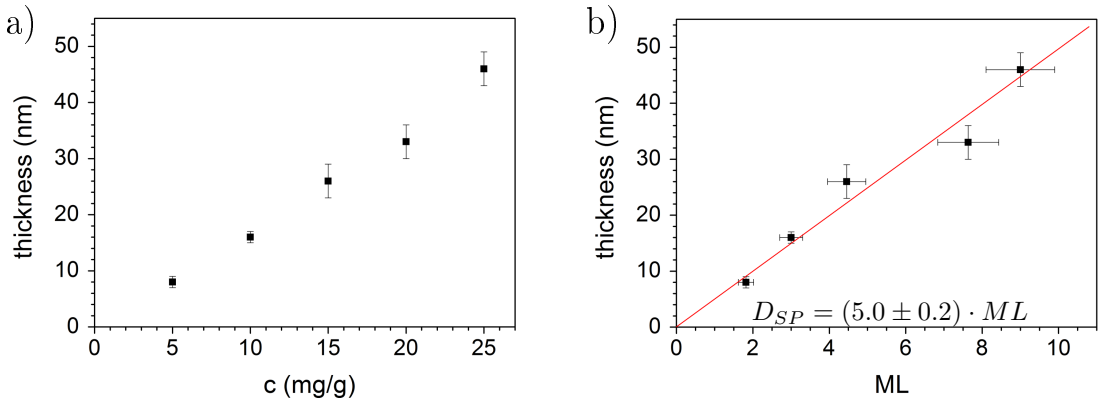

Figure 4.5: Determination of layer thickness of pyridine capped CdSe QDs on ITO by step profiler; a) plotted versus concentrations of the suspensions; b) plotted versus the number of monolayers.

concentration was determined by a gravimetric analysis of dried QDs. For the measurement called pyridine 1 the concentration of CdSe QDs in suspension was determined by UV-vis measurements. Another factor might be the temperature during layer deposition. Deposition was done at room temperature, which varies and influences the evaporation during the deposition and therefore the thickness of the resulting layer. As measurements of multiple samples showed, layers from the same batch (prepared from the same suspension and within a week) could be trusted to have equal thicknesses.

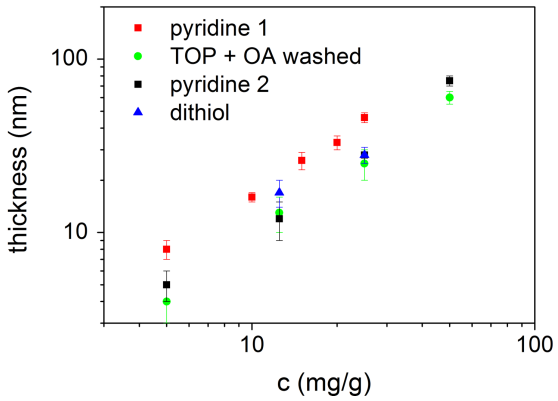

Figure 4.6: Determination of layer thickness of CdSe QDs from different suspension on ITO by a step profiler.

QD layers from pyridine 2 and chlorobenzene showed very similar thicknesses

ranging from ≈ 5 nm to ≈ 70 nm. For pyridine capped QD layers the thicknesses were (5 ± 1)nm, (12 ± 3)nm, (28 ± 3)nm and (75 ± 5)nm for layer prepared from suspensions with concentrations of 5 mg/g, 12.5 mg/g, 25 mg/g and 50 mg/g respectively. For TOP + OA washed CdSe QD layers thicknesses of (4 ± 1)nm (5 mg/g), (13±3)nm (12.5 mg/g), (25±5)nm (25 mg/g) and (60±5)nm (50 mg/g) were found. The determination of TOP + OA pristine QD layers was not possible with this method. This is probably due to the high content of organics which results in a very soft layer. For dithiol QD layers the thickness could only be determined for layers prepared from 12.5 and 25 mg/g. The layers still had the same thickness as before the dithiol ligand exchange ((17 ± 3)nm and (28 ± 3)nm for 12.5 mg/g and 25 mg/g, respectively). Measurement of the thin layer from 5 mg/g suspension was not possible as the layer tended to be scratched from the ITO surface in flakes during the measurement and thus preventing the thickness determination. The adhesion between dithiol capped QDs seems to be stronger than the adhesion to the substrate. This can be explained in terms of linking of QDs. The strong adhesion between dithiol capped QDs was also seen in the SEM. Figure 4.7 shows a SEM cross section of a dithiol capped CdSe QD layer. At some places the QD layer overlaps the ITO. The layer did not break where the ITO substrate broke and is still attached to the layer on top of the substate. This is only possible if there is a strong adhesion between QDs and was not observed for any of the other QD layers.

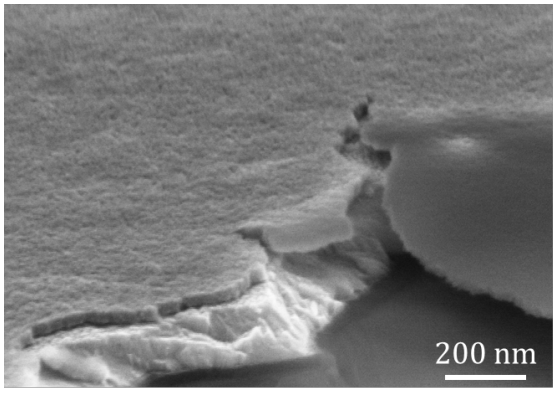

Figure 4.7: SEM cross section of a dithiol capped CdSe QD layer showing the strong adhesion between CdSe QDs (accelerating voltage 8 kV, Zeiss, LEO 1530 GEMINI).

4.1.5 Determination of layer thickness by SEM

The CdSe (pyridine 2) QD layers whose layer thicknesses were determined by the step profiler were also measured by SEM. Figure 4.8 shows cross section of these layers. The SEM picture shows a homogeneous and complete coverage of the ITO.

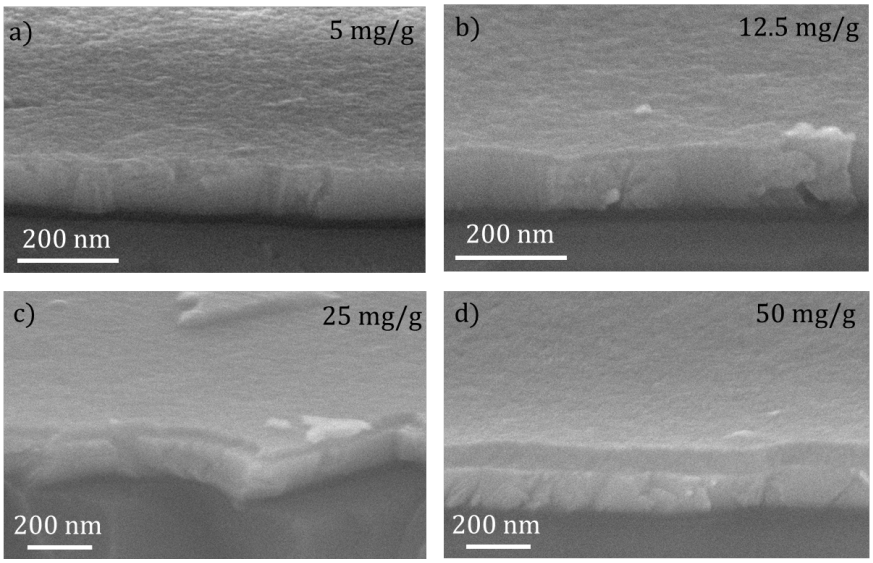

Figure 4.8: SEM cross sections of thin layers of CdSe QDs on ITO from pyridine suspensions with concentrations of a) 5 mg/g, b) 12.5 mg/g, c) 25 mg/g and d) 50 mg/g (accelerating voltage 20 kV, Zeiss, LEO 1530 GEMINI).

The thicknesses determined from the cross sections were (12 ± 3)nm, (22 ± 3)nm, (37 ± 3)nm and (90 ± 5)nm for concentrations of 5 mg/g, 12.5 mg/g, 25 mg/g and 50 mg/g, respectively. Plotting these values against the number of monolayers determined from the step profiler thickness (figure 4.6) and the calibration from figure 4.5 ($D_{SP} = (5.0 \pm 0.2) \cdot ML$) one obtains the correlation between SEM thickness and number of monolayers (figure 4.9). A SEM thickness (D_{SEM}) of 6.1 ± 0.4 nm per monolayer was found.

For the comparison of layers from different suspension SEM cross section of the different QD layers on ITO were measured (figure 4.10). The layers were all deposited from a suspension with a concentration of 25 mg/g. The QDs formed homogeneous layers on the ITO. Thicknesses of 45 ± 5 nm were found for TOP + OA capped QDs (both pristine and washed) and 37 ± 3 nm for pyridine and dithiol. Therefore all samples had comparable thicknesses.

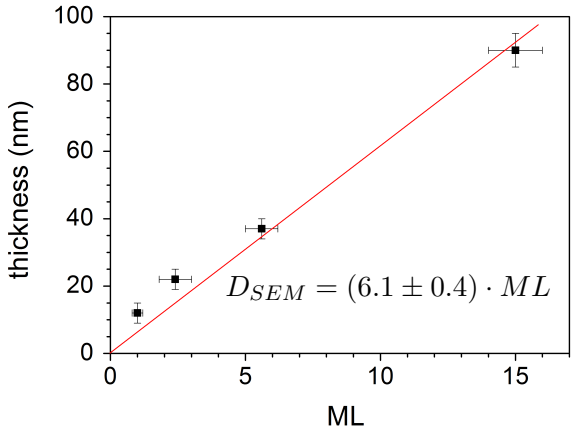

Figure 4.9: Correlation between SEM layer thickness and number of monolayers of pyridine capped CdSe QDs on ITO.

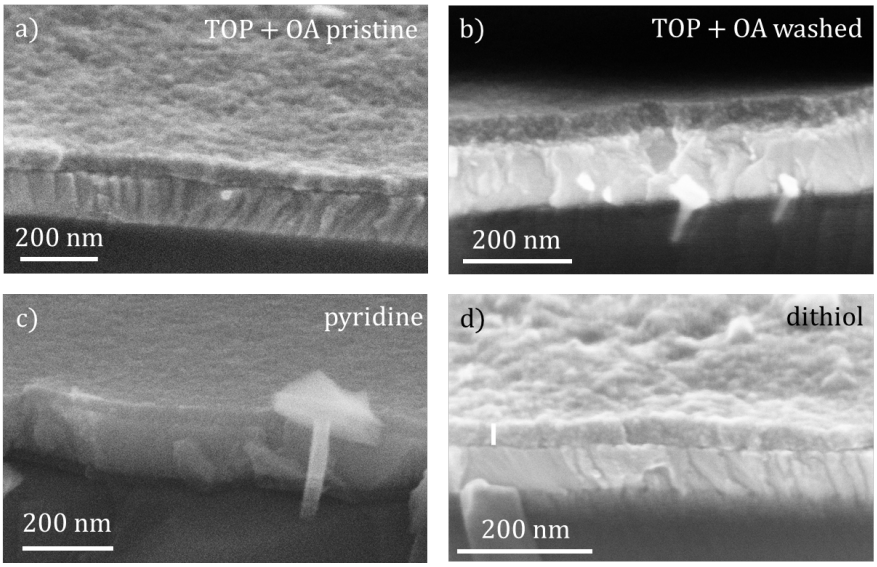

Figure 4.10: SEM cross sections of thin layers of CdSe QDs on ITO from a suspension of 25 mg/g with different surfactants (accelerating voltage 8 kV for a), b) and d) and 20 kV for c), Zeiss, LEO 1530 GEMINI).

The results of the step profiler and SEM measurements (figure 4.6 and 4.10) show that QD layers prepared from different suspensions had equal thicknesses. For CdSe QD capped with pyridine equal thickness on ITO, SiO_2 and Si were measured by RBS and UV-vis (figure 4.3 and 4.4). Additionally the areal density, the absorption at 599 nm and the thickness measured by the step profiler and the SEM per monolayer could be determined for pyridine capped CdSe QD layers (table 4.1).

method	parameter	1ML
RBS	areal density	$4.9 \times 10^{15}\,\mathrm{cm}^{-2}$
UV-vis spectroscopy	absorption	0.011 ± 0.001 (@ 599 nm)
step profilometry	step profiler thickness	5.0 ± 0.2 nm
SEM	SEM thickness	6.1 ± 0.4 nm

Table 4.1: Characterization of CdSe QD layers and determined parameters for 1ML of CdSe QDs.

4.2 Charge separation in the first monolayer of CdSe QDs

In order to gain an understanding about charge separation and transfer processes in CdSe QD layers experiments on CdSe QD layers in the monolayer range were performed. Therefore layers of CdSe (pyridine) QDs on ITO substrates were prepared by dip coating and the influence of photon energy, light intensity and layer thickness on charge separation and recombination was studied. The results of this section were partially published by Zillner et al in 2011[102] and 2012[103]. The chapter ends with a model for the mechanisms of charge separation and recombination in CdSe (pyridine) QD layers.

4.2.1 Spectral dependence of charge separation

The spectral dependence of charge separation was determined by modulated SPV measurements with the fixed capacitor setup. Figure 4.11 shows spectral SPV measurements of a monolayer of pyridine capped CdSe QDs on ITO.

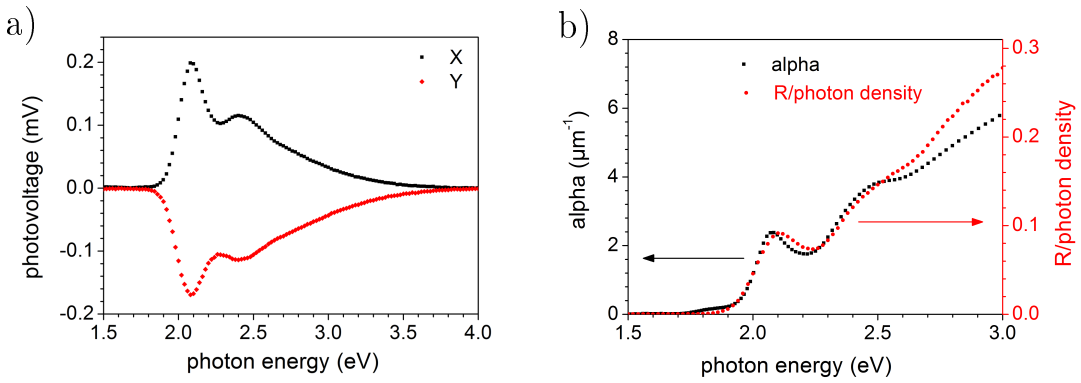

Figure 4.11: SPV spectra of a monolayer of CdSe pyridine QDs measured at 8 Hz, a) X- and Y-signal; b) R signal normalized by the photon density (see figure 3.19) compared with the absorption of a CdSe (pyridine) QD layer.

A positive X- and a negative Y-signal, which were both in the order of 0.2 mV, were measured. Therefore the electrons were separated towards the interface between QD layer and ITO. Separation of charges started around 1.8 eV showing a peak at

$2.1eV$ (first excitonic peak) and a shoulder at 2.4 eV. The SPV signal decreases at higher photon energies as the photon density decreases (see figure 3.19).

To compare the SPV signal with UV-vis absorption measurements the R signal was divided by the photon density (figure 4.11 b). The number of excited charge carriers is proportional to the absorption. Therefore the amount of separated charge carriers (SPV) was compared to the amount of excited charge carriers (absorption). The SPV signal followed the absorption spectrum. Thus the SPV signal of a CdSe QD monolayer was solely dependent on the number of excited charge carriers and independent on photon energy. The modulated charge separation was proportional to the number of excited QDs.

4.2.2 Influence of light intensity on charge separation in a CdSe QD ML

The influence of light intensity on charge separation was measured with transient SPV. Figure 4.12 illustrates the photon energies used for excitation. The red arrows mark the photon energies at the spectrum of the PV amplitude of a CdSe (pyridine) monolayer. At 1.9 eV (640 nm) the excitation is below the first excitonic peak and therefore trap states have to be involved. 2.1 eV (590 nm) is the energy of the first excitonic transition. The excitations at 2.4 eV (520 nm) and 3.0 eV (420 nm) are excitation above the first excitonic peak. Therefore the excitation into different states was studied (figure 4.12b). For the variation of light intensities filter wheels with gray filters with varying density (see section 3.3.3) were used.

Figure 4.13 shows SPV transients of a CdSe QD ML on ITO excited at 640, 590, 520 and 420 nm with varying light intensity. The transients look similar independent of the excitation energy. The transients have a positive signal, thus photo excited electrons were separated towards the ITO/QD interface, as already observed by spectral measurements. The maximum intensity was reached within the resolution time of the system. The maximum SPV signal, was between 100 and 1 mV and increased with increasing light intensities, as more charge carriers were excited. The transients, excited with a laser intensity of more than 1 mJ/cm^2, consisted of a fast decay at short times, followed by a slow decay. Transients

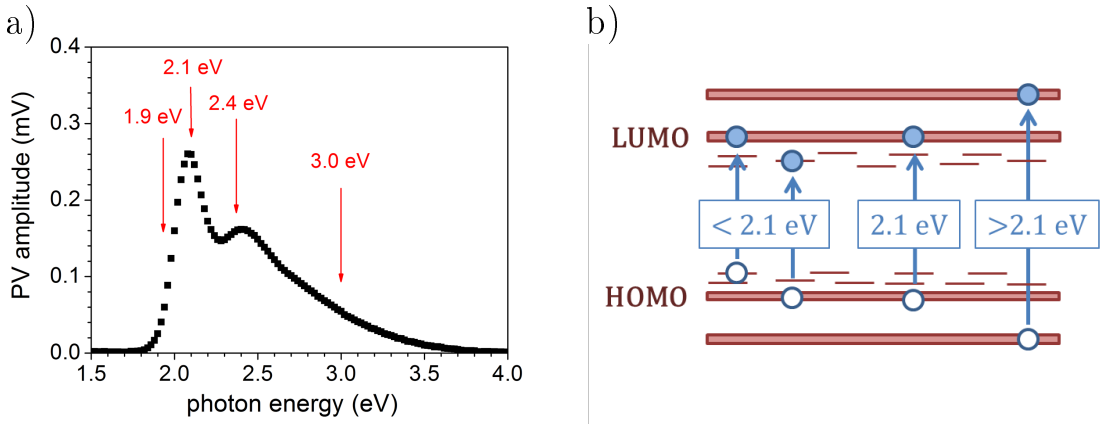

Figure 4.12: Illustration of the photon energies used for transient SPV; a) PV amplitude of a CdSe (pyridine) monolayer, measured with the fixed capacitor setup at 8 Hz, the red arrows indicate the photon energies 1.9, 2.1, 2.4 and 3.0 eV (640, 590, 520 and 420 nm) used for excitation. b) Excitation of charge carriers in a CdSe QD with different photon energies.

excited with lower intensities only showed the slow decay. The SPV signal dropped to zero around 50 to 100 ms.

As all transients have equal characteristics independent on excitation energy the processes of charge separation and recombination were the same. For excitation at 640 nm at least one charge carrier was trapped (see figure 4.12). Therefore charge carrier separation, also for excitation at higher energies, was via trap states.

To see the dependence of charge separation on the number of absorbed photons, the maximum SPV signal was plotted versus the absorbed photon density (figure 4.14). The absorbed photon density (δ) was defined as the product of pulse intensity (I), the effective absorber layer thickness (D) and the absorption coefficient α, and divided by the photon energy (E).

$$\delta = \frac{IDa}{E} \tag{4.2}$$

As the layers were optically thin, the absorption can be assumed to be linearly dependent on the absorption coefficient and the thickness. The values for α were extracted from figure 4.11 b) and were 0.23, 2.3, 3.3 and 5.3 μm^{-1} for 640, 590, 520 and 420 nm, respectively. The maximum SPV signal was independent of the photon energy used for excitation. A linear dependency of the maximum SPV

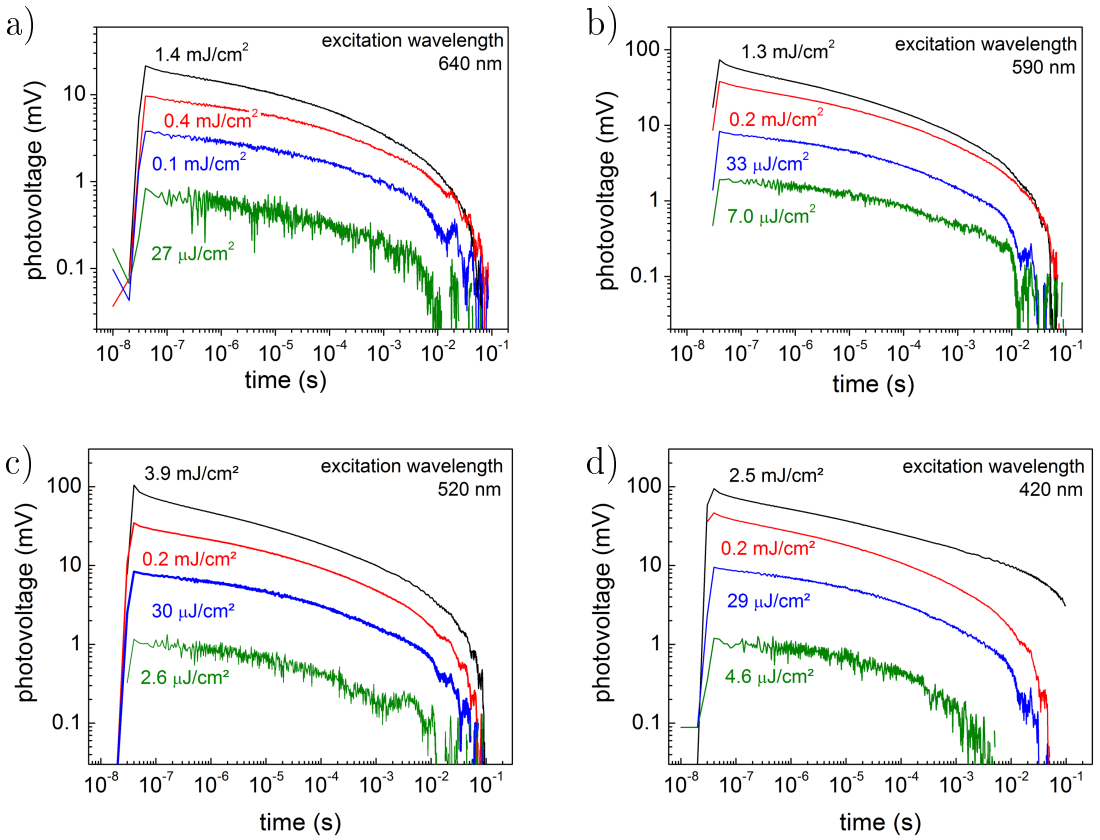

Figure 4.13: SPV transients of a CdSe (pyridine) ML excited at 640, 590, 520 and 420 nm with varying light intensities.

on absorbed photon density (independent on photon energy) was observed for photon densities below $10^{12}\,\mathrm{cm}^{-2}$. For higher photon densities the ratio between SPV signal and photon density was decreasing with increasing photon density. The maximum SPV signal measured was around 100 mV.

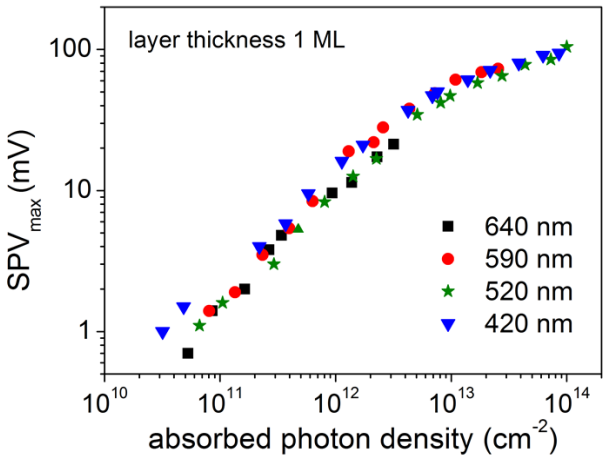

Figure 4.14: Dependence of the maximum SPV signal on absorbed photon density.

The immediate rise of the SPV signal shows that charges were separated in the ns range or faster. The slow decay of the SPV signal, which was in the ms range, indicated a mechanism of charge recombination including trap states and/or diffusion of charge carriers. The maximum SPV signal was only dependent on the number of excited charge carriers in the sample. A linear dependency was present for an absorbed photon density up to $10^{12}\,\mathrm{cm}^{-2}$. The density of CdSe (pyridine) QDs in a monolayer is $\approx 4.5 \times 10^{12}\,\mathrm{cm}^{-2}$. Therefore the saturation of the SPV signal started in a range where the probability of more than one excited charge carrier pair per QD became high, which is a condition for the onset of Auger recombination.[104] As Auger recombination takes place in the ps range, it is a lot faster than radiative recombination. Auger recombination limits the number of charge carriers which are separated as it is faster than the charge separation process.

The maximum of the number of separated charge carriers can be estimated in the picture of a parallel plate capacitor (see equation 3.3). The maximum SPV signal measured was $\approx 100\,\mathrm{mV}$. As only a single monolayer was present, the charge separation can be assumed to be in the range of the diameter of the QDs. The

position of the hole on the QD surface is arbitrary. Therefore an average charge separation length of 3 nm was chosen, as the average distance is the radius of the QD plus the QD/ITO distance. The CdSe QD layer consists of a mixture of CdSe and organic molecules. Therefore a relative effective dielectric constant of 5 was chosen. For these assumptions a density of separated charge carriers in the order of $1 \times 10^{12}\,\mathrm{cm}^{-2}$ was calculated. Therefore charge separation took place in approximately 20 % to 25 % of the QDs in the first monolayer. Comparing the maximum number of separated charge carriers with the maximum of absorbed photon density 1 out of 100 charge carrier pairs, which were excited was separated at the highest light intensity. At lower absorbed photon densities (10^{11} to $10^{12}\,\mathrm{cm}^{-2}$) 1 out of 10 excited charge carrier was separated.

4.2.3 Influence of layer thickness on charge separation

The influence of layer thickness on charge separation was measured with transient and spectral SPV. For a complete picture not only charge separation (SPV) was measured but also the radiative recombination of non separated charge carriers (PL). To monitor the slow processes of charge separation at constant illumination SPV spectra were also measured with the Kelvin probe setup.

In transient measurements (figure 4.15) the maximum SPV signal was independent of layer thickness. For all transients the maximum amplitude was reached within 40 ns. The transients however differed at longer times. The transients of thicker layers tended to decay slower. Half times of 8.8×10^{-7}, 5.4×10^{-6}, 2.0×10^{-6} and 2.7×10^{-5} s were measured for thicknesses of 1, 2 5 and 15 ML, respectively.

As the amplitude of the SPV signal was independent on the layer thickness, initial charge separation only occurred in the first monolayer of QDs. Thus the interface to the ITO played an important role in the process of charge separation. The slow decay of thicker layers showed that the layer thickness influenced the process of charge carrier diffusion and recombination. Charge carriers, which were initially separated in the first monolayer of QDs, diffuse into neighboring QDs and thus slow down the process of recombination.

The transients in figure 4.15 were measured by averaging 8 transients. The very first transient which was measured on CdSe (pyridine) QD layers was different

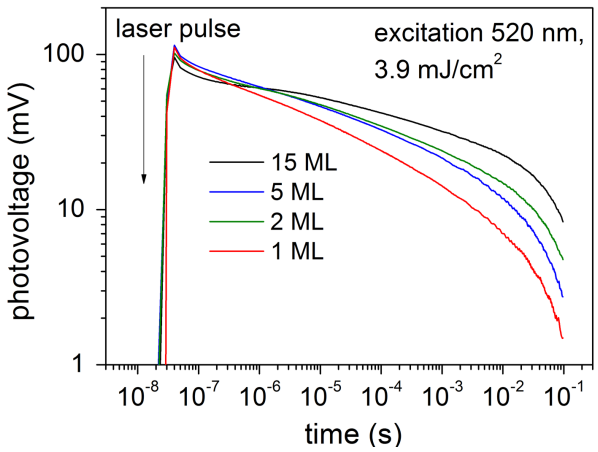

Figure 4.15: Transient SPV measurments of CdSe (pyridine) QD layers with varying thickness, with a 520 nm laser pulse.

from the following transients. Therefore samples changed due to excitation. Figure 4.16 shows two examples of single transients on CdSe QD layers with a thickness of 2 and 15 MLs. The first transients had longer half times, or in the case of the 15 ML thick layer it even rose after the fast decay at the beginning. During the measurement of the first transient separated charge carriers occupied trap states and the holes from the first monolayer traveled into the neighboring layers. Some charge carriers remained in trap states, additionally an internal field was built up as holes moved towards the surface. These two effects led to a decrease of the half times of following transients. First, some trap states were already occupied and charge carriers remained untrapped or were trapped in higher lying defects. Second, the internal field which was build up during the previous transient hindered charge separation. The effect was stronger for thicker layers as holes could travel further into neighboring layers and less charge carriers recombined before the next transients were measured.

The spectral measurements (figure 4.17 a) show a dependency of SPV amplitude on layer thickness. A maximum SPV signal of 0.82, 0.48, 0.45 and 0.26 mV was detected at 2.1 eV for 15, 5, 2 and 1 ML, respectively. The spectra were measured with a frequency of 8 Hz and therefore the slow decay of thicker layers influenced the SPV amplitude. The thickness of the layers did not influence the spectral behavior.

The SPV phase, shown in figure 4.17 b) was between −80° and −37°. Therefore

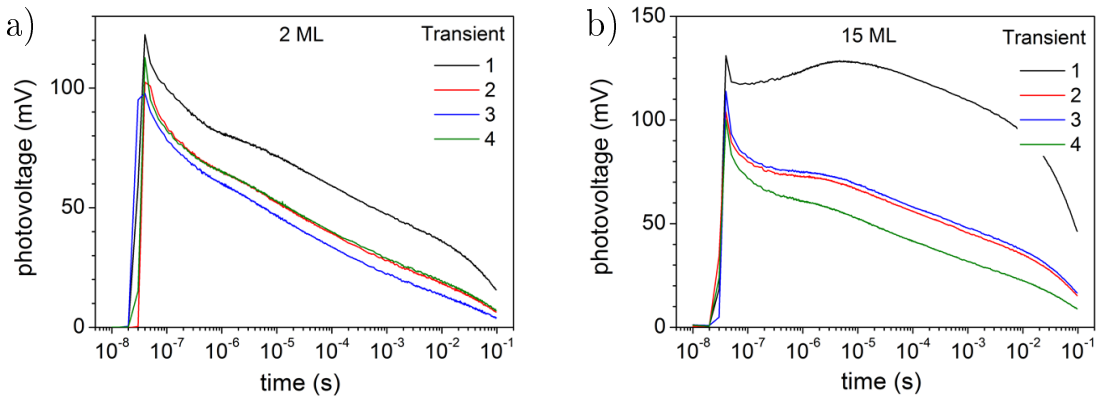

Figure 4.16: Single transient SPV measurements on a a) 2ML and b) 15 ML thick CdSe (pyridine) QD layer, excited with a 520 nm laser pulse.

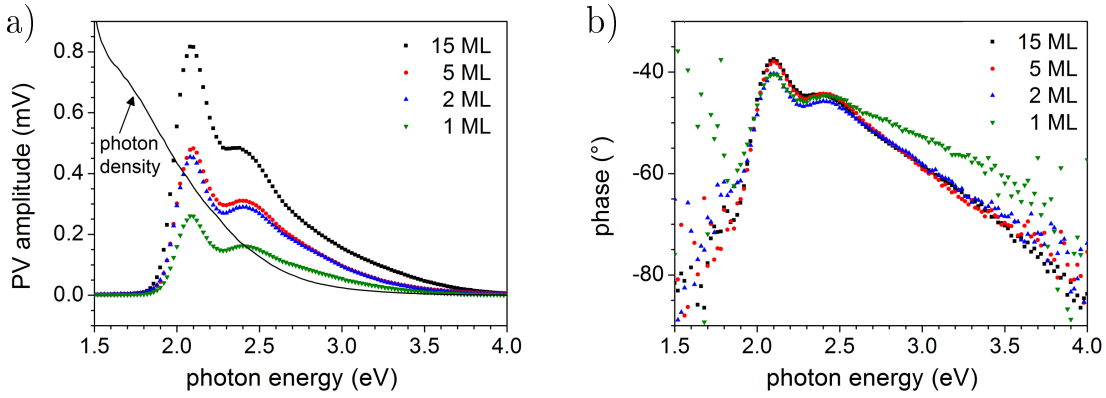

Figure 4.17: Spectral SPV measurments of CdSe (pyridine) QD layers with varying thickness, measured at 8 Hz, a) shows the amplitude, b) the phase.

a separation of electrons towards the QD/ITO interface and holes towards the external surface was present (see section 3.3.2). The phase was, except for the 1 ML layer at high energies, only weakly dependent on layer thickness and followed the PV amplitude. The phase was approximately $-80°$ at 1.5 eV and increased to $-40°$ and $-37°$ at 2.1 eV for the 1 ML/2ML and the 5/15 ML thick CdSe QD layer. Thus charge separation and/or recombination became faster with increasing PV amplitude. At a higher number of excited charge carriers, more traps were filled. Therefore some charge carriers remained untrapped and charge separation and recombination became faster.

Additionally to SPV measurements PL spectra were measured on CdSe QDs layers on ITO. In PL radiative recombination is measured. Trapping of photo-excited electrons on the ITO should quench the PL. Therefore PL is complementary to SPV. Figure 4.18 shows PL spectra in the region of the first excitonic peak of CdSe (pyridine) QD layers with varying thickness on ITO. A broad background from the ITO was present. The maximum of the first excitonic peak was at 630 nm and was therefore shifted by 30 nm, or 90 meV to lower energies, relative to the excitonic peak in UV-vis absorption. The highest signal was measured for a layer thickness of 5 ML. The signal decreased by about 4 times for the 3 ML thick layer and vanished completely for the thinnest layer of 1.5 ML. For larger thicknesses of 7 and 9 ML the signal decreased by approximately 30 % as compared to the 5 ML layer.

The shift of the first excitonic peak in PL compared to the absorption spectrum was due to the splitting of the first excitonic transition and the Förster energy transfer (see section 2.1.3). According to Efros et al[58] CdSe QD in suspension with a diameter of 4 nm have a Stokes shift of 55 ± 5 meV due to the splitting of the conduction band. The remaining 35 ± 5 meV are due to Förster energy transfer from smaller CdSe QD into larger ones with a smaller bandgap. It is reasonable to assume a Föster energy transfer as our QDs have an interparticle distance of ≈ 1 nm, what is close enough for an electronic energy transfer.

The PL signal was strongly dependent on the layer thickness. To describe the dependence of the PL signal on the layer thickness, a model which considers multiple reflections at the surface and interfaces of the layer would be required. This is out of the scope of this work. However the complete quenching of the PL

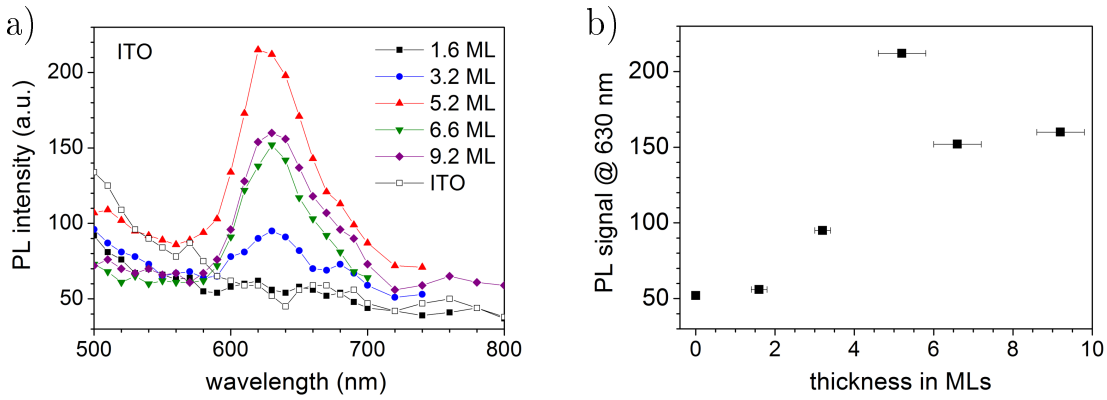

Figure 4.18: a) PL spectra of CdSe (pyridine) QD layers with varying thickness, excited with a 337 nm laser pulse (see section 3.5) ; b) shows the dependence of the PL signal on the layer thickness. The spectra were not corrected by the transmission function of the optical system.

signal from the thinnest layer is an important observation. The PL from the first monolayer was completely quenched due to the ITO. This points towards a fast (< 1 ns) electron transfer from QDs towards the ITO surface. As only the charge carriers from the first monolayer were dissociated, exciton diffusion between QDs was inefficient. This is in line with observations of Talgorn et al.[105]

To study charge separation in CdSe QD layers on ITO at constant illumination SPV was also measured with the Kelvin Probe setup (see figure 4.19). Using the Kelvin Probe we can get information about the workfunction of the sample in the dark and about slow processes of charge separation under constant illumination. In the dark a decrease of the contact potential difference (ΔCPD) with increasing layer thickness was measured. The ΔCPD increased from -190 to -125, -90 and -47 mv for 1, 2 5 and 15 ML thickness respectively.

Under illumination the CdSe QD layers had a negative SPV signal, which did not correlate with the thickness of the CdSe QD layers. The maximum of the SPV signal was around photon energies of 2.1 eV and was -151, -162, -122 and -119 mV for the 1, 2, 5 and 15 ML thick CdSe QD layer, respectively. A strong increase in SPV signal began around 1.7 eV for all layers. An additional, weaker signal below 1.7 eV was present for thicker layers. This defect related signal correlated with the QD layer thickness. A signal of -3, -6, -8 and -17 mV was measured for the 1, 2, 5 and 15 ML thick QD layer, respectively.

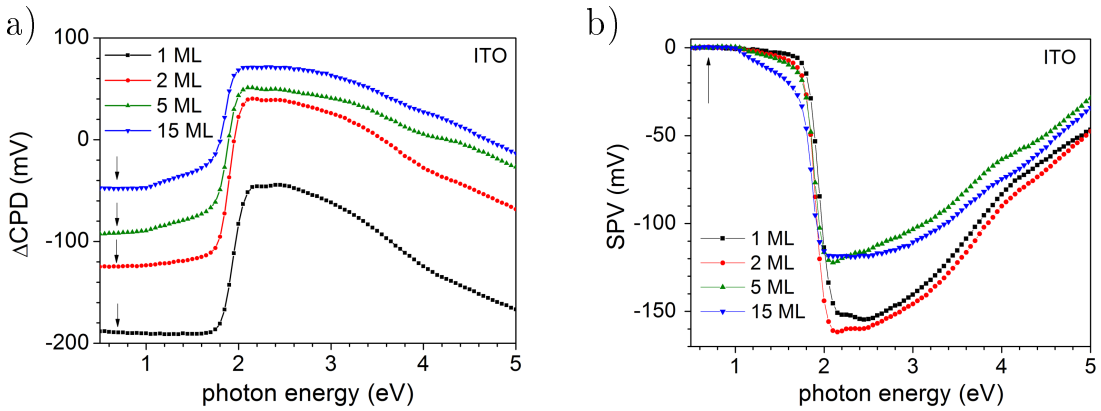

Figure 4.19: ΔCPD (a) and SPV (b) spectra of CdSe QD (pyridine) layers with varying thicknesses on ITO.

For thinner CdSe QD layer a smaller ΔCPD in the dark and therefore a smaller workfunction was measured. This points towards a positive charged ITO surface, inducing a dipole in the QD. The dipole in the QDs at the surface was stronger for thinner layers.

For Kelvin probe spectra on CdSe QD layers on ITO no correlation between layer thickness and PV signal could be found. The PV signal from the Kelvin measurements had the opposite sign of PV signals from the fixed capacitor measurements (see figure 4.17, page 73). Therefore charge separation at constant illumination was opposite to modulated charge separation. The fast charge separation measured with the fixed capacitor was explained by trapping of electron, excited in the CdSe QDs on the ITO surface. Both, charge separation and charge recombination at the CdSe QD/ITO interface, were fast enough that they could be modulated in the range of 0.1 s. The negative SPV signal measured at constant illumination could be explained in terms of a second process of charge separation. This separation of electron towards the external surface (negative SPV signal), or the recombination of the separated charge carriers was too slow for the modulated and transient measurements. This mechanism could be for example trapping of electrons at the external QD layer surface. This mechanisms dominated separation of charge carriers at constant illumination, over the possibly limited trapping of electrons on the ITO surface.

4.2.4 The process of charge separation in CdSe (pyridine) QDs on ITO

Taking the results of SPV and PL into account a first model of the processes of charge separation and diffusion in CdSe (pyridine) QD layers on ITO could be created. Figure 4.20 illustrates the involved processes. Free charge carriers are created in CdSe QDs by absorption of light (figure 4.20 a). The excited charge carriers relax from excited states above the band edges into the lowest excitonic state. If there is more than one electron pair present the charges recombine via Auger recombination. Electrons photo-excited in the first monolayer of QDs are trapped on the ITO surface, whereas the charge carriers photo-excited in the other QD layers recombine radiatively or non radiatively without dominant direction of charge separation. (figure 4.20 b) From the PL measurements it followed that practically all electrons photo-excited in the first monolayer are trapped on the ITO, as quenching of PL from the first monolayer of QDs was practically complete. In SPV however only 1 % to 10 % of excited charge carriers are detected. Therefore, non-radiative recombination of electrons trapped at the ITO and holes at QDs, which was shorter than the resolution time of SPV, that means within 10^{-8} s, took place.

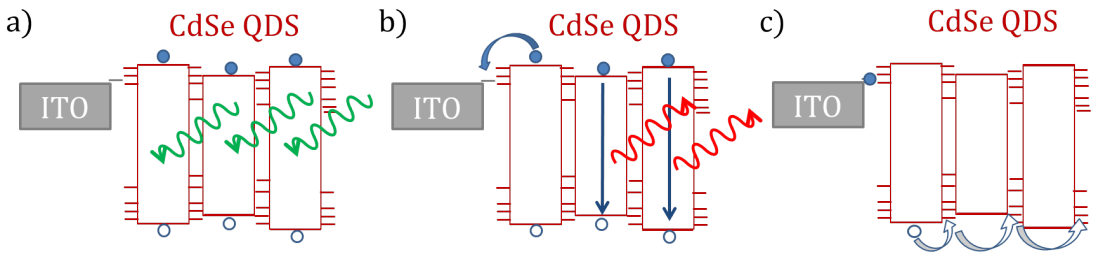

Figure 4.20: Processes of charge separation in CdSe QDs on ITO (a) photon absorption, (b) charge carrier recombination and trapping of electrons of the first QD monolayer on ITO (c) trapping of holes on the QD surface and diffusion into neighboring QDs.

The remaining free holes of the first monolayer are subsequently either trapped on the CdSe QD surface or diffuse into neighboring QDs, while the diffusion process is trap limited (figure 4.20 c). It is reasonable to assume trapping of charge carriers as half times in the μs range were measured. Lifetimes of free, untrapped charge carriers in CdSe QDs are in the range of 100 ns or less, as measured by microwave

conductivity by Talgorn et al.[106] The traps on the surface of QDs can be either caused by non saturated Se dangling bonds or by the π-ring of the pyridine (see section 2.1.3).

The long times of separation and/or recombination led to a filling of trap states and created an internal field. Therefore the transients at samples which were photo-excited of the first time had longer half times than following ones and charge separation and/or recombination became faster at higher excited charge carrier densities due to saturation of the deepest trap states.

Under constant illumination, measured with the Kelvin Probe setup the sign of the SPV signal changed. The dominant mechanism at constant illumination was a separation of electrons towards the external surface. Trapping of photo-excited electrons on the external QD surface took place. The charge separation and/or recombination in this process was too slow to be measured at modulated and transient SPV but dominated for longer times at constant illumination. Figure 4.21 illustrates the separation of charge carriers in a CdSe QD layer on ITO at constant illumination.

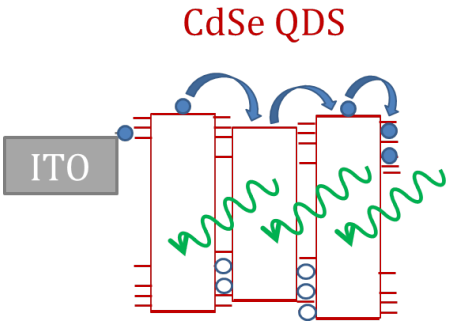

Figure 4.21: Scheme of charge separation in the CdSe QD layer on ITO.

4.3 Role of ligand exchange at CdSe QD layers for charge separation

In the following section the influence of different surfactants on charge separation and recombination in CdSe QD layers is studied. By the exchange of surfactants the electronic properties of the layer change due to a change of the dielectric constant of the surrounding medium, a change of trap states on the surface of CdSe QDs and due to a variation in interparticle distance and thus changing the coupling between QDs. The variation of interparticle distance is described in section 4.1.1. In this section the optical properties of CdSe QD layers are measured by UV-vis and compared to the absorption of CdSe QDs in suspensions. The change in trap states is measured by PL. PL is an indicator for the number of trap states in a sample, as a high density of traps leads to nonradiative recombination. Furthermore radiative recombination from trap states was observed. Transitions from defects are measured by low temperature PL. The influence of the changes induced by ligand exchange is determined by spectral and transient SPV. Most of the results described in this section were published by Zillner et al.[103]

4.3.1 Optical properties of CdSe QD layers by UV-vis spectroscopy

Absorption of CdSe QDs in suspension and CdSe QD layers was measured by UV-vis spectrometry. Figure 4.22 shows the spectra of the absorption of CdSe QDs with varying surfactants in the region of the first excitonic peak. Both spectra of highly diluted suspensions (dots) and layers (lines) were measured. Agglomeration of dithiol capped QDs prevented measurements in a stable suspension. The spectra of suspensions and layers were identical for the three samples measured. Layers of QDs stabilized by OA and TOP had identical absorption spectra. The maximum of the first excitonic peak was located at 607 nm for the layers and suspensions. The exchange with pyridine led to a blueshift of the first excitonic peak by 24 meV (maximum at 598 nm). Ligand exchange at CdSe pyridine QDs with dithiol resulted to a redshift relative to the pyridine QDs by 14 meV (maximum at 602 nm).

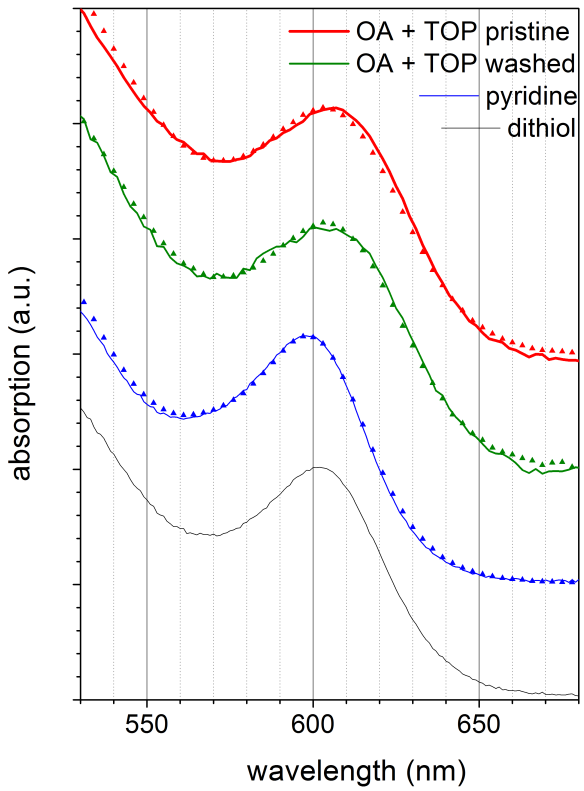

Figure 4.22: UV-vis absorption spectra of CdSe QDs with varying surfactants in the region of the first excitonic peak. The lines are the spectra of the layers, the dots the spectra of the suspension of CdSe QDs.

The position of the first excitonic peak is dependent on the radius of CdSe QDs and the dielectric constant of the surrounding medium, as described in section 2.1.2. Equation 2.9 gives an approximation of the position of the first excitonic peak.[47,48] As discussed in section 2.1.2 different factors can lead to a change in the position of the first excitonic peak.

The ligand exchange with pyridine led to a blueshift of 24 meV, for layers and highly diluted suspension. Coupling between QDs would result (i) in a redshift and (ii) in different spectra for layers and suspensions, as the distance between QDs in suspension is too large to enable electronic coupling between QDs. Therefore the shift in the first excitonic peak is attributed to the change in dielectric environment when exchanging TOP and OA with pyridine. A similar shift of the first excitonic peak of CdSe QDs due to ligand exchange with pyridine was described by Lefrançois et al.[55]

The ligand exchange of pyridine with dithiol led to a redshift by 14 meV. As ligand exchange with dithiol resulted in agglomeration of CdSe QDs in suspension the absorption could only be measured in layers. The bathocromic shift observed can be attributed to different factors. (i) Electronic coupling between dithiol capped QD is possible. (ii) Again a change in the dielectric constant could cause the shift. (iii) An increase of the effective radius of CdSe QDs, as measured for CdSe/CdS core/shell QDs is possible.[56]. Electrons or holes might be extended into the surfactants shell and therefore increase the effective radius of QDs.

4.3.2 Quenching of the PL by ligand exchange

Increase of trap states leads to lower PL signals as nonradiative recombination via trap states if favored. Therefore PL was used as an indicator to measure changes of trap states in CdSe QD layers due to ligand exchange. Figure 4.23 shows PL spectra of the bare Si substrate and of CdSe QD layers on Si substrates stabilized with varying surfactants. The PL spectrum of the bare Si substrate had a typical peak with a maximum around 1150 nm. No PL signal was observed for the Si substrate in the spectral range where the first excitonic peak of CdSe QDs is expected. We also expect no signal from the ligands as they absorb and emit light only at higher energies.

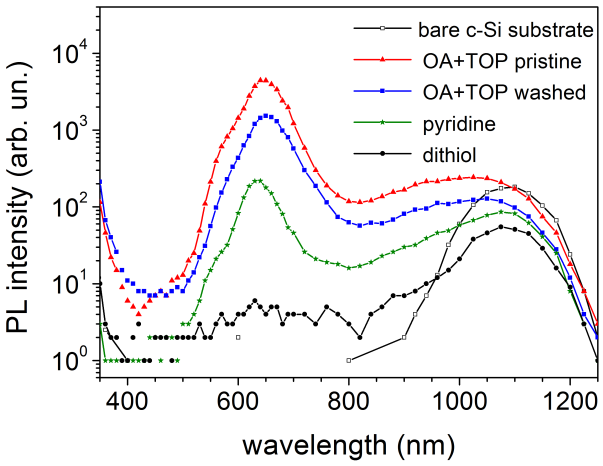

Figure 4.23: PL spectra of CdSe QD layer with varying surfactants on Si, excited with a 337 nm laser pulse. The spectra were not corrected by the transmission function of the optical system.

A large PL signal, which could be assigned to the first excitonic peak, with a maximum at 640 nm, was observed for the layer of pristine CdSe QDs (TOP+OA). A pronounced shoulder at 570 nm was present. The excitonic peak of the PL appeared at lower energies by about 100 meV in comparison to the absorption spectra. A high PL intensity was also observed at wavelengths above the first excitonic peak at which the PL signal of the Si-substrate was not yet pronounced. This PL signal, which is due to radiative recombination via defect states, was about 20 times lower (values at 620 and 800 nm were compared) than that at the first excitonic peak.

After washing both, the PL signal in the excitonic peak and the PL related to radiative recombination via defect states, decreased by a factor of approximately 3 and 2, respectively. In comparison to the PL of washed CdSe QDs, the PL signal of pyridine treated CdSe QDs was reduced by a factor of ≈ 8 and ≈ 4 for the PL from the excitonic recombination and via defects, respectively. By the post-treatment with dithiol the PL signal in the first excitonic peak and in the defect range decreased by about 50 and 5 times in comparison to the pyridine treated CdSe QDs.

The redshift of the first excitonic peak in CdSe QDs layers compared to the

position of the first excitonic peak in absorption spectroscopy was caused by the splitting of the lowest excitonic state and the Förster energy transfer (see also section 2.1.3 and section 4.2.3). Assuming a shift of (55 ± 5)meV due to the splitting of the conduction band[58] a shift of (45 ± 5)meV due to Förster energy transfer can be calculated. This was, in the margin of the errors, in agreement with the values determined for pyridine capped CdSe QDs (see section 4.2.3).
The quenching of the PL signal is an indicator for the number of trap states on the surface of QDs. In addition to radiative recombination from the band edges, photoexcited charge carriers can also relax into trap states and from there might either recombine radiatively (forming the defect peak at lower energies in the PL) or relax nonradiatively. A high density of trap states increases the probability of nonradiative recombination and thus reduces the PL signal (see also section 2.1.3).

As the layer of pristine CdSe QDs had the highest PL signal measured for our samples, the pristine TOP + OA capped QDs had the smallest density of traps on the QD surface. The PL signal originated mainly from the first excitonic transition around 640 nm. Thus most charge carriers recombined radiatively from the band edges without further relaxation into trap states. Additionally radiative recombination from a broad distribution of states at lower energies was also observed. Thus there were trap states present deep in the band gap at the surface of the CdSe QDs. This could be for example nonsaturated Se dangling bonds (see chapter 2.1.3).

Washing led to less radiative recombination. This could be interpreted in terms of an increasing number of nonsaturated dangling bonds. The decrease in radiative recombination and therefore increase in nonradiative recombination due to pyridine ligand exchange pointed toward an even higher number of trap states. Electrons could be stabilized in the π ring of the pyridine and radiative recombination was suppressed.[68] Additionally an increase in the number of trap states due to nonsaturated dangling bonds created by the exchange procedure is possible. The post-treatment with dithiol reduced the PL to almost zero. Sionnest et al.[68] and Wuister et al.[69] described trapping of holes in the lone pairs of the sulfur atom, which forms a covalent bond with Cd and thus a quenching of radiative recombination. Additionally trapping in the π ring of the benzenedithiol is possible.

Figure 4.24 illustrates the relaxation possibilities of photo-excited electrons and holes into the triplet state, Cd and Se dangling bonds, the HOMO of pyridine and 1-4-benzenedithiol and the sulfur bond.

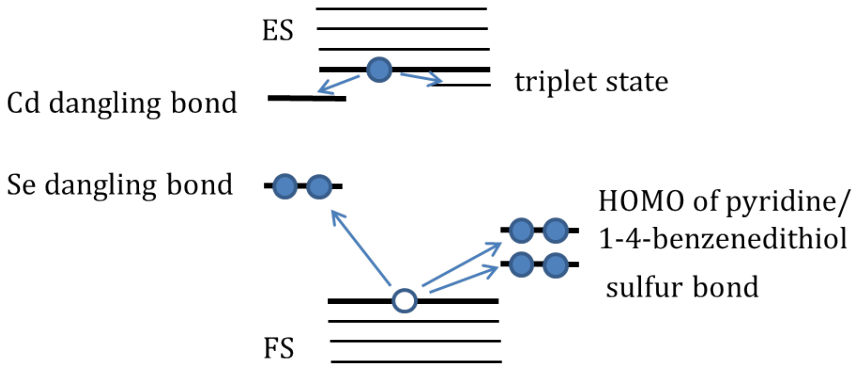

Figure 4.24: Relaxation mechanisms of photo-excited electrons and holes in CdSe QDs. (ES and FS denote empty and filled states.)

4.3.3 Determination of defect states by PL measurements at low temperature

In order to gain more information about defect states in CdSe QD layers, PL experiments at low temperature were performed. By decreasing the temperature in the system, the probability for thermally activated trapping and nonradiative recombination was decreased. Therefore more charge carriers recombine radiatively and trap states can be observed. The measurements at low temperature were done under constant illumination, whereas at room temperature charge carriers were excited by pulsed excitation (see section 3.5).

Figure 4.25 a) shows the PL spectra of CdSe QD layers with varying surfactants at 4.5 K. The spectra were corrected to an energy scale. Comparing the low temperature spectra with those at room temperature a similar trend was observed. Again the highest PL signal was present for the pristine QDs. The signal from the first excitonic peak decreased by approximately 2 orders of magnitude due to washing and another two orders due to the ligand exchange with pyridine. No signal in the region of the first excitonic peak was observed after the post treatment with dithiol. For the TOP + OA capped CdSe QD layers a broad

signal at low energies was measured. The shape of the spectra was similar to the room temperature PL measurements. For pyridine and dithiol capped CdSe QD layers the defect peak was at higher energies, around 1.7 eV. The peak from trap states in pyridine capped CdSe QDs was distincly higher than the excitonic peak.

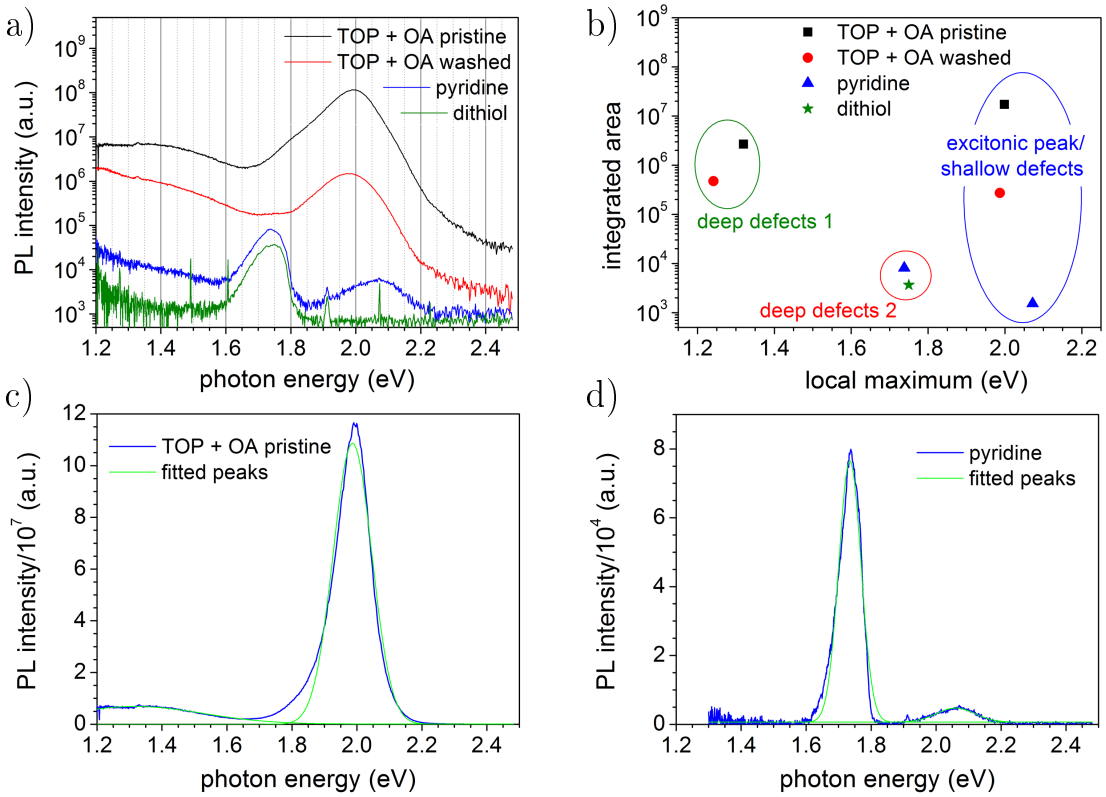

Figure 4.25: PL measurements of CdSe QD layers with varying surfactants on Si at 4.5 K, excited with a He-Cd-laser at 325 nm with a light intensity of 7 mW. The spectra were corrected by the response function of the setup and to the energy scale. a) Shows a comparison of the PL spectra of CdSe QDs with different surfactants; b) gives an overview of the maxima of the peaks and their area; c) and d) show the fit of OA+TOP pristine and pyridine CdSe QDs with single Gaussian peaks.

Compared to room temperature PL measurements, the energy of the first excitonic peak at 4.5 K was shifted to higher energy, for all samples. The maxima in the region of the first excitonic peak were at 2.00, 1.98 and 2.07 eV for TOP + OA pristine, washed and pyridine capped CdSe QDs and were therefore shifted by 60, 40 and 100 meV as compared to room temperature PL measurements, respectively.

According to Valerini et al. a blue shift of $\approx$ 60 meV due to the temperature dependence of the CdSe band gap takes place when going from room temperature to 4.5 K.[107] On the other hand a more effective Förster energy transfer at lower temperature is expected, which should shift the peak to lower energies.[60] The Förster energy transfer, which goes with $(1/R_{DA})^6$, for washed CdSe QDs should be approximately 4 times as effective as the energy transfer for pristine QDs, as the average center-to-center distance between QDs decreases from 7.7 to 6.2 nm (see section 4.1.1 and 2.1.3). Therefore the shift from 2.00 to 1.98 eV for pristine and washed CdSe QDs at 4.5 K can be explained.

The signals in the spectra could not be fitted by single Gaussian peaks, as the peaks were slightly asymmetric. In figure 4.25 c) and d) a fit of the spectra of TOP + OA pristine and pyridine capped CdSe QDs illustrates the asymmetry of the signals. At least two Gaussian peaks per signal would be required for a reasonable fit. The asymmetry in the peaks was either due to recombination from different states and/or due to the size distribution of QDs in the sample. Different states in the region of excitonic recombination could be explained in two different ways. First the peaks originated probably from the different states formed by the splitting of the first excitonic peak (see section 2.1.3). A second explanation could be states close to the band gap as for example Cd atoms with nonsaturated dangling bonds, or Se atoms with a single nonsaturated dangling bond (see also figure 4.24 and section 2.1.3).

The broad peaks of the deep defects in the TOP + OA capped CdSe QD layers were located around 1.3 eV. The broad defect peak was associated with radiative recombination from or into Se atoms with two dangling bonds, which served as hole traps (see figure 4.24 and section 2.1.3). The defect peaks of the pyridine and dithiol capped QDs were narrower and at a higher energy than those of TOP and OA capped QDs. The maxima of the peaks were at 1.74 and 1.75 eV for pyridine and dithiol capped CdSe QDs respectively. These peaks were associated with radiative recombination via the π ring of the ligands, or the lone pairs of the sulfur atom (see figure 4.24 and section 2.1.3). The asymmetry of these peaks can also be explained by the size distribution of the QDs and different defect states.

As the reason for the asymmetry of signals was not clear the signals were not fitted with multiple Gaussian peaks. The area of the peaks was determined by

integration over a certain region. The area of the excitonic peak of the TOP + OA capped CdSe QD layers was determined by an integration between 1.7 and 2.5 eV, the defect area was determined by integration between 1.2 and 1.7 eV. The area of the excitonic peak of pyridine capped CdSe QD layers was determined by integration between 1.85 and 2.5 eV, while the defect area of pyridine and dithiol capped CdSe QD layers was determined by integration between 1.5 and 1.85 eV. The integrated areas and the maxima of the peaks are plotted in figure 4.25 b).

The area of the excitoninc peak of TOP + OA pristine CdSe QDs was approximately 5 times as high as the determined area of the defects. Note that the area of the defect peak was probably higher, as it could only be measured down to an energy of 1.2 eV. The area of the excitonic peak was reduced to around 2 % after washing of the CdSe QDs. For washed CdSe QDs the area of the defect peak was approximately twice that of the excitonic peak. For pyridine capped CdSe QDs the area of excitonic peak was only approximately 0.1 % of that of pristine QDs. The area of the defect peak was five times that of the excitonic peak. For dithiol capped CdSe QDs no excitonic peak could be detected. The defect peak was in the same region as the defect peak of pyridine capped CdSe QDs and had approximately half of the area.

The decreasing PL intensity with surface modification was in line with PL measurements at room temperature and showed an increase in defect density. The PL measurements at 4.5 K showed different energies for radiative defect recombination for TOP + OA ($\approx$ 1.3 eV) and pyridine and dithiol capped CdSe QDs ($\approx$ 1.7 eV). Therefore a new type of defect was present in pyridine and dithiol capped CdSe QDs which could be assigned to recombination via the π ring of the aromatic ligands pyridine and 1-4-benzenedithiol and the sulfur bond of dithiol with Cd.

By variation of light intensity further information about charge carrier dynamics can be found. A variation of light intensity was possible for TOP + OA capped QD layers as the PL signal for these layers was relatively large. Figure 4.26 a) and c) show PL spectra of pristine and washed CdSe QD layers on Si. The excitation intensity was varied between 7 and 0.01 mW and 7 and 0.03 mW for pristine and washed CdSe QD layers, respectively.

The areas of the excitonic and the defect region were determined by integration

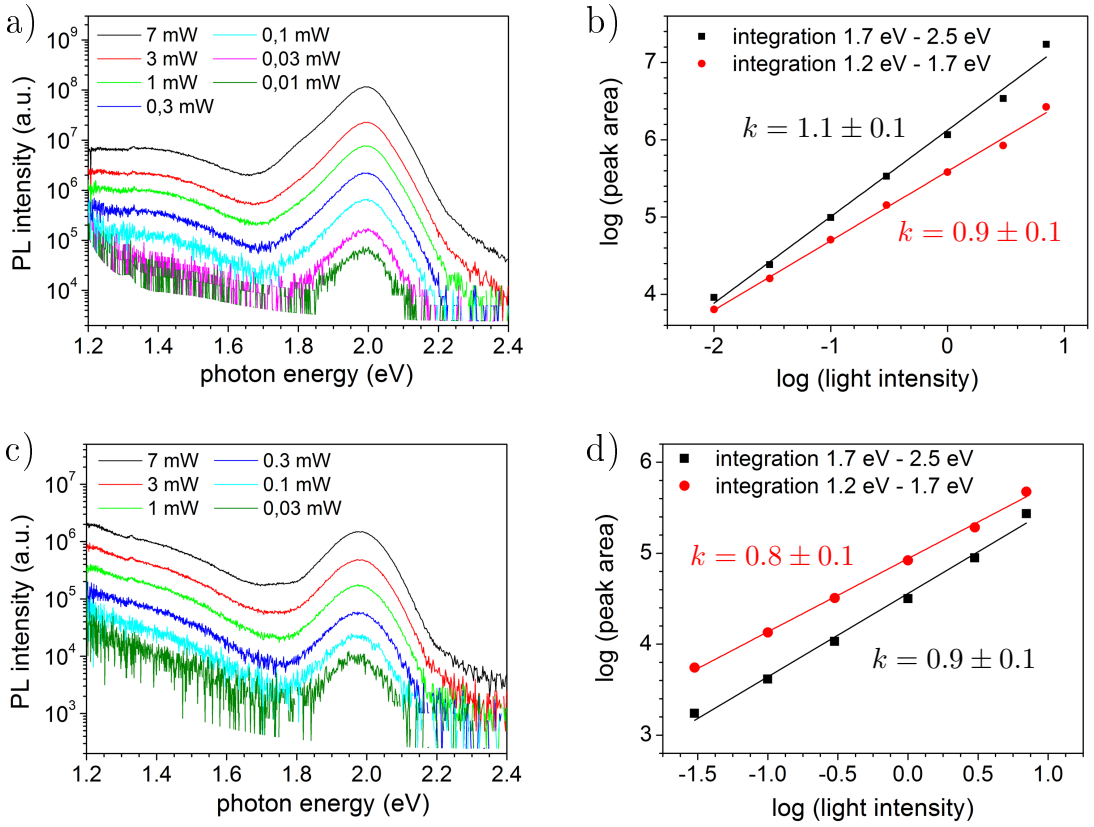

Figure 4.26: PL measurements of CdSe QD layers on Si with TOP + OA surfactants, with varying light intensity, at 4.5 K, excited with a He-Cd-laser at 325 nm. The spectra were corrected by the response function of the setup and to the energy scale. a) and c) Show PL spectra of pristine and washed CdSe QDs layers with varying light intensity, respectively; b) and d) are plots and linear fits of the logarithm of the peak areas against the logarithm of the light intensity, obtained from the spectra in a) and c), respectively. k is the slope from the linear fits.

from 1.7 to 2.5 eV and 1.2 to 1.7 eV, respectively. The logarithm of the areas, received from the fit was plotted against the logarithm of the excitation intensity (figure 4.26 b and d). By a linear fit of these plots the slope k was determined. Table 4.2 gives an overview of the positions of PL peaks (E), their area excited with a light intensity of 7 mW (a) and their k value.

	excitonic peak			defect peak		
ligands	E(eV)	a (a.u.)	k	E(eV)	a (a.u.)	k
TOP + OA pristine	2.00	1.72×10^8	1.1 ± 0.1	1.32	2.66×10^6	0.9 ± 0.1
TOP + OA washed	1.98	2.72×10^5	0.9 ± 0.1	1.24	4.73×10^5	0.8 ± 0.1
pyridine	2.07	1.53×10^4		1.74	8.06×10^4	
dithiol				1.75	3.65×10^4	

Table 4.2: Overview of the photon energy of the peak positions (E), the integrated peak areas (a) and the k values determined from PL spectra at He temperature.

By the slope (k) of the linear fit of these plots one can determine the dependence of PL signal (I_{PL}) on light intensity (I_L).

$$I_{PL} \sim (I_L)^k \tag{4.3}$$

A slope of 1.1 ± 0.1 and 0.9 ± 0.1 was found in the region of excitonic recombination of pristine and washed CdSe QDs. The slopes in the defect region were 0.9 ± 0.1 and 0.8 ± 0.1, respectively. A slope of 1 represents a linear dependence of PL intensity on light intensity. For slopes smaller than 1 less radiative recombination per excited electron hole pair with increasing light intensity was measured. For excitons in isolated QDs, which do not interact with each other, a linear dependence is expected in a region where less than one electron-hole pair per QD is exited. Therefore the number of charge carriers at maximum excitation intensity was estimated. Assuming a long exciton lifetime of 0.1 µs and having an absorption of 0.45 at 325 nm for a 5 ML thick CdSe QD layer a charge carrier density of approximately $1 \times 10^{13}\,\mathrm{cm}^{-2}$ at 7 mW results. Having a density of $\approx 2.3 \times 10^{13}\,\mathrm{cm}^{-2}$ of QDs in a 5 ML CdSe QDs layer, even at the highest light intensity there was less than one charge carrier per QD excited within 0.1 µs. Therefore a k value of 1 is

expected if the QDs do not interact and lifetimes of $\leqslant 0.1\,\mu s$ are present.

The energy of excitons can be transferred to neighboring QDs by Förster energy transfer. The transfer rate for washed CdSe QDs was approximately 4 times as high as for pristine QDs (see calculation above). Therefore the probability of two excitons being transfered into the same QD was higher for washed CdSe QDs, increasing with light intensity. The increased Förster energy transfer also resulted in the shift of the first excitonic peak to lower energies. The PL of a QD occupied by two electrons was quenched by Auger recombination. Thus we received lower k values for washed CdSe QDs. Charge carriers in defect states have a longer lifetime than excitons. The longer lifetime increased the probability that an exciton was transfered into a QD, where defect states were already occupied. Thus lower k values were measured for defect than for exciton recombination.

The PL measurements at low temperature confirmed the result of room temperature PL measurements. The intensity of the PL signal decreased with surface treatment showing an increase of trap states in the QDs. Furthermore different defect states were found for TOP + OA capped CdSe QDs ($\approx 1.3\,eV$) and pyridine and dithiol capped CdSe QDs ($\approx 1.7\,eV$). Therefore a different defect was created in pyridine and dihtiol capped CdSe QD, which is assigned to the HOMO of the ligands. Due to variation of light intensity different k values were determined for pristine and capped CdSe QDs. The k values for pristine CdSe QDs were generally higher than those of washed QDs. This points towards less coupling and Förster energy transfer in pristine CdSe QD layers. The lower k values of defect assigned radiative recombination could be explained in terms of longer life times.

4.3.4 Charge separation and recombination in CdSe QD layers with varying surfactants

The influence of ligand exchange on charge separation was measured with spectral modulated and transient SPV. Figure 4.27 shows modulated SPV spectra of (a) PV amplitudes and (b) the phase for thin films (4 ML) of CdSe QDs on ITO. With proceeding ligand exchange an overall increase in PV amplitude was observed. For the pristine TOP + OA sample no surface photovoltage signal could be measured. For the surface treated samples the maximum of PV amplitude was detected at

2.1 eV and was 0.07 mV for the TOP + OA washed QDs, 0.5 mV for the pyridine and 2 mV for the dithiol QDs. Whereas for the pyridine and the washed sample charge separation only occurred above 1.6 eV, a signal below 1.5 eV was observed for the dithiol sample.

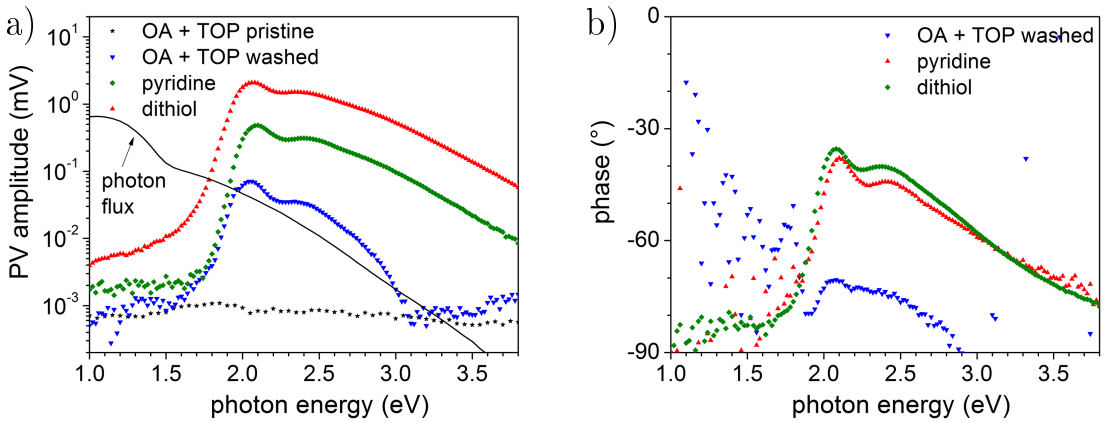

Figure 4.27: SPV spectra of CdSe QD layers (4 ML) with varying surfactants, measured with the fixed capacitor setup at a frequency of 7 Hz; a) shows the amplitude and b) the phase.

Charge separation did not occur in the CdSe OA + TOP pristine sample, which was characterized by a low number of defects and a thick stabilizing shell of 1.6 nm. The increase of modulated SPV signal was due to a more effective charge separation due to ligand exchange. The maximum at 2.1 eV is at the position of the first excitonic peak, where the absorption is high. The decrease in photon density at higher energies led to the decrease in SPV signal. The signal below 1.5 eV in dithiol capped QDs points towards a high density of deep defects states and an effective charge separation from these states.

The phase of the SPV signal (see figure 4.27 b) depended on the PV amplitude. The noise of the phase was high in the regions where the SPV signal was close to zero. The phase was between −80° and −35° and had the same shape as the SPV amplitude. For pyridine and dithiol capped CdSe QD layers the phase was around −80° at 1.5 eV and increased to −38° and −35° at 2.1 eV for pyridine and dithiol capped QD layers, respectively. For the washed CdSe QDs the trend was less obvious but still to be seen. The phase was around −80° at 1.9 eV and increased to −70° at 2.1 eV.

Generally under modulated illumination separation of photo-excited electron towards the internal surface and thus towards the ITO took place (see also section 3.3.2). At low photon energy, where only few electron hole pairs are created, the phase was close to $-90°$ and therefore a slow separation and/or recombination of charge carriers (in relation to the modulation period) took place. As only few charge carriers were separated in this region, they were mainly trapped in defect states and the recombination of charge carriers was slow. At higher photon energies a higher number of charge carriers was created and the deepest traps were filled. Therefore charge carriers were trapped in more shallow defects, charge separation and/or recombination became faster and the phase increased. The phase of the OA + TOP washed CdSe QD layer is lower as generally a lower number of charge carriers were separated.

SPV transient measurements were performed on the same samples as shown in figure 4.27. Figure 4.28 a) shows SPV transients of 4 ML thick QD layers excited with a 520 nm laser pulse. The measurements were in agreement with the SPV spectra. Again no signal was observed for the TOP + OA pristine QDs. The SPV amplitude increased with proceeding surfactant exchange up to 95 mV for the TOP + OA washed QDs, 114 mV for the pyridine QDs and 137 mV for the dithiol QDs. The maximum, which was reached within the system resolution time, was only weakly depended on post treatments. Furthermore the transients became longer with proceeding ligand exchange; the half time increased from 4.6×10^{-7} s for TOP+OA washed QDs to 1.9×10^{-6} s for pyridine and 9.0×10^{-6} s for dithiol capped QDs.

Figure 4.28 b) shows transients of layers of the same QDs but with a thickness of only 1 ML. In section 4.2 we showed that the amplitude of transients depended only weakly on the QD layer thickness for pyridine capped QDs. Figure 4.28 b) shows that the same is also true for TOP+OA and dithiol capped QDs. A slight decreas in the amplitudes to 65 mV for TOP+OA washed QDs and 74 mV for pyridine and dithiol capped QDs was observed. The half times for TOP+OA and pyridine QDs monolayers were in the same range as for the multilayers (4.2×10^{-7} s and 1.0×10^{-6} s for washed and pyridine capped QDs, respectively). The half time for the monolayer of dithiol capped QDs was considerably higher (1.2×10^{-4} s).

Charge separation in surface treated CdSe QDs on ITO took place within 10^{-8} s

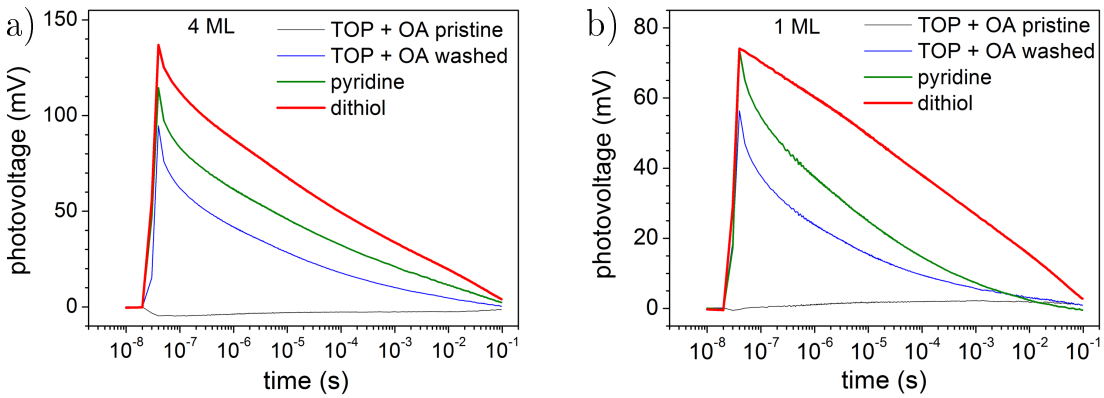

Figure 4.28: SPV transients of CdSe QD layers with varying surfactants, excited at 520 nm, a) layers with a thickness of 4 ML, b) layers with a thickness of 1 ML.

by trapping of the photo-excited electron on the ITO. As the SPV amplitude was only weakly dependent on surface treatment and layer thickness charge separation happened mainly from the first monolayer of CdSe QDs on ITO. Increasing life times with ongoing ligand exchange were either caused by increasing trap densities or a more effective transport of holes into neighboring QDs with decreasing interparticle distance.

4.3.5 The single QD approximation model

The exchange of ligands on CdSe QDs does not only change the interparticle distance between CdSe QDs in layers (see section 4.1.1) but also the electronic properties and the density of trap states. The position of the first excitonic state was shifted due to ligand exchange, as shown by UV-vis and the number of traps increased with ongoing ligand exchange, as radiative recombination decreased. Different defect states due to dangling bonds and surfactants could be distinguished via low temperature PL. SPV spectra showed a trend which was opposite to PL. The amplitude of modulated SPV spectra, which was zero for the pristine CdSe QD layers, increased with ongoing ligand exchange.

Charge separation took place in all but the pristine QD layers. The amplitude of SPV transients, of surface modified CdSe QD layers, depended only weakly

on surface treatment and layer thickness. As the initial SPV signal was close to independent of the thickness of QD layers, charge separation is mainly happening in the first monolayer of QDs (see also section 4.2). Electrons were trapped on the ITO surface within a short time ($< ns$) as PL from a monolayer was completely quenched. For the pristine QD layers the distance between ITO and QD, created by the thick surfactant shell, was probably too high for the trapping of the electron on the ITO surface.

Whereas the surface treatment only weakly influenced the initial charge carrier separation, the decay times depended strongly on surface treatment. The decay times varied with surface treatment. Therefore the surfactants influenced the process of charge recombination which was in the range from several hundreds of ns (TOP+OA) to several hundreds of μs (dithiol). The SPV transients were much longer than photoconductivity transients, which have decay times of 100 ns or less.[105] The difference between microwave conductivity measurements and SPV is that in microwave conductivity measurements free charge carriers are detected, whereas SPV measures charge carriers separated in space which can be mobile or trapped in localized states. Therefore trapping of charges prolongs SPV transients, but reduces the photoconductivity. The long lifetime, the strong influence of surfactants and the difference to photoconductivity measurements points towards a trap influenced recombination process. In the following it is reasonable to assume that free holes were trapped within the resolution time of transient SPV measurements on QD surface states caused for example by Se dangling bonds or the surfactants. From this position the hole could tunnel into neighboring trap states, also on QDs which were not directly on the ITO. Additionally the hole could be excited into the delocalized state of the QD. For the recombination of the hole and electron, the hole had to tunnel into the state occupied by the electron. A higher number of traps and a smaller interparticle distance decreased the probability of this process and led to a slower recombination of charge carriers.

On the basis of these results the single QD approximation model was developed to simulate SPV transients measured at a monolayer of CdSe QD dots. The starting point for the simulation was the trapped electron at the ITO surface and the hole trapped at the surface of the CdSe QD. For a monolayer of weakly coupled CdSe QDs the consideration of an isolated QD in contact with the ITO surface was sufficient (single QD approximation). To simplify the analysis of the system

only hopping of holes to unoccupied donor states at the QD surface as well as to the occupied acceptor state at the ITO surface (recombination) were considered. Additionally, the hole could be excited into the first delocalized state in the QD from which it could be trapped again at a surface state or recombine.

The charge transfer in the single QD approximation was controlled by tunneling processes and was described by Miller-Abrahams hopping. In this case charge transport between traps states and the delocalized state of a single QD and not between QDs was considered. Transitions to states where the final energy was higher than the initial one $E_i^c < E_f^c$ are thermally activated. The tunneling rate is given by the following equation in case of Miller-Abrahams tunneling.

$$\tau^{-1} = \begin{cases} \tau_0^{-1} e^{-2\alpha R_{if}} e^{-(E_f^C - E_i^C)/k_b T}, & \text{for } E_i^C < E_f^C \quad (4.4a) \\ \tau_0^{-1} e^{-2\alpha R_{if}}, & \text{for } E_i^C > E_f^C, \quad (4.4b) \end{cases}$$

where τ_0 denote the elementary time, α, the inverse tunneling length R_{if} the distance between the initial and final state of tunneling, k_B the Boltzmann constant and T the temperature. E_i^c and E_f^c are the Coulomb interaction corrected energy positions of the initial and the final state of a tunneling process. The correction for the Coulomb interaction was achieved by shifting the energy of the hole states j depending on their distance to the trapped electron.

$$E_j^c = E_j + \frac{e}{4\pi\varepsilon\varepsilon_0 R_{ej}} \quad (4.5)$$

(3) where e, ε, ε_0 and R_{ej} are the elementary charge, the relative dielectric constant, the dielectric constant of vacuum and the distance between the electron and the hole trap state.

The geometric and energetic parameters in the model are illustrated by figure 4.29 a) and b), respectively. The fluctuation of the geometric parameters was not considered in the model. However the energetic distributions, due to fluctuations of the QD radius, were considered in the width of energy levels. The radius was set to the average radius of QDs, to a value of 2.25 nm. The ITO-QD distance was inserted into the simulation as a free parameter and was fitted in the range of the values measured by TEM for distances between QDs.

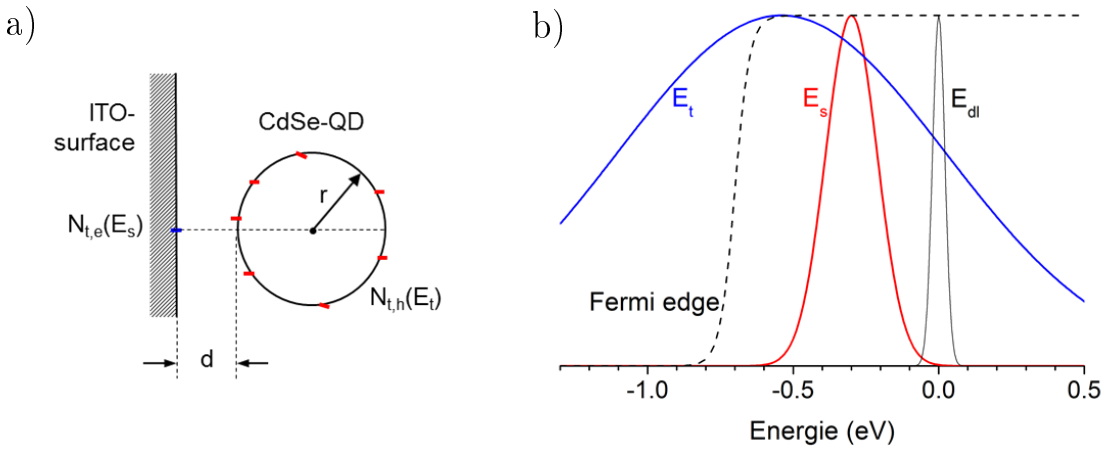

Figure 4.29: Illustration of geometric (a) and energetic (b) parameters in the single QD approximation model.

The energetic parameters in the model, which are illustrated in figure 4.29 b) were the energy level of the delocalized state (E_{dl}), the energy level for the electron state on the surface of the ITO (E_s) and the energy level for hole traps at the surface of the QD (E_t). E_s acted as recombination state for the hole. A Gaussian distribution of energy states with a certain standard deviation was chosen. For simplicity the same distributions of energy for the QDs with varying surfactants were used. E_{dl} was fixed as the reference energy at 0 eV with a standard deviation σ_{dl} of 0.03 eV, accounting for the fluctuations in QD radii. The energy of the traps (E_t) was set at 0.5 eV below the delocalized state with a broad standard deviation σ_p of 0.8 eV. The maximum of E_t was therefore set at a value which was approximately the average of the energies found for trap states in QD layers by PL. The results from PL measurements cannot be directly transfered to the simulation as only radiative transitions were measured. Therefore it is reasonable to assume a broad distribution of trap states. The Fermi level, which was optimized to fit the transients, defines the energy level of up to which the traps states were filled. Only the deepest traps were influenced by the Fermi level. These traps create longer decay times, than can be measured by the SPV set up. As the RC-time constant of the setup was considered in the simulation of transients, the position of the Fermi level became less critical. The state E_s, which was located on the ITO surface, was set at -0.3 eV and thus between E_p and E_{dl}. E_s had a standard

deviation σ_s of 0.125 eV. E_s was set to a higher energy than E_t as the holes had to overcome an energy barrier for recombination.

For the dielectric constant ε an effective dielectric constant was used. It is reasonable to use an effective dielectric constant as the hole was mainly trapped at the surface of the QD and thus experiences both the influence of the QD and the surfactant. The effective dielectric constant (ε_{eff}) was derived by Maxwell-Garnett (equation 4.6)[108] from the dielectric constant of the inclusion (CdSe, ε_i) and the surrounding media (surfactant, ε_m).

$$\varepsilon_{eff} = \varepsilon_m \frac{\varepsilon_i(1+2\delta_i) - \varepsilon_m(2\delta_i - 2)}{\varepsilon_m(2+\delta_i) + \varepsilon_i(1-\delta_i)} \tag{4.6}$$

OA, TOP and pyridine have a relative static dielectric constant of 2.5, 2.2 and 12.6.[109] Using a dielectric constant of 5.8 for CdSe[49] and assuming a volume fraction (δ_i) of 0.5 for the surfactants, an effective dielectric constant of 3.8 and 8.8 for OA+TOP and pyridine capped QDs, was found. There are additional uncertainties in the determination of ε_{eff} of dithiol CdSe QDs as (i) the ε of 1,4-benzenedithiol is not known and (ii) both dithiol and pyridine were present on the QD surface with a fraction of approximately one half (see section 3.1.2). 1,4-benzenedithiol should have a relatively low dielectric constant, due to its symmetry. Taking the relative large dielectric constant of pyridine and the low dielectric constant of dithiol the effective dielectric constant should be smaller than the one of pyridine capped CdSe QDs, but larger than the one for TOP+OA capped QDs. As there are uncertainties in the values of the effective dielectric constants, screening the Coulomb interaction, the values of the dielectric constants were fitted in a certain range of 2.8 to 4.8 for $\varepsilon_{eff}^{OA+TOP}$, 7.5 to 9.5 for $\varepsilon_{eff}^{pyridine}$ and 5 to 7 for $\varepsilon_{eff}^{dithiol}$.

The number of traps, which were randomly distributed at the QD surface, was a free parameter which was fitted. For the given simulations, the energetic position of each defect state was chosen randomly with regard to the Gaussian defect distribution. For the inverse tunneling length α and the elementary time values of $0.9\,\mathrm{nm}^{-1}$ and $10^{-13}\,\mathrm{s}$ were chosen. The length of the exciting laser pulse was considered by randomly changing the starting time of the simulation with respect to the shape of the laser pulse. The simulation of SPV transients was done by adding several thousand independent samples of relaxation (N) of one photo-

generated electron trapped at the ITO surface and one hole trapped at the QD surface. The equation for the simulation was derived from equation 3.3:

$$SPV(t) = \frac{e}{\varepsilon\varepsilon_0} \cdot ANF \cdot \sum_{i=1}^{N} \left(x_{e,i}\left(t\right) - x_{h,i}\left(t\right)\right) \tag{4.7}$$

ANF is a normalization factor and $x_{e,i}$ and $x_{h,i}$ are the projection of positions of the electron and of the hole perpendicular to the electrode surface at a given time t of sample i. Therefore the sum in equation 4.7 gave the distance of charge centers perpendicular to the electrode.

Figure 4.30 compares the measured and simulated transient of MLs of CdSe QDs on ITO with different surfactants (see also figure 4.28 b). Measurements and simulations show a close fit.

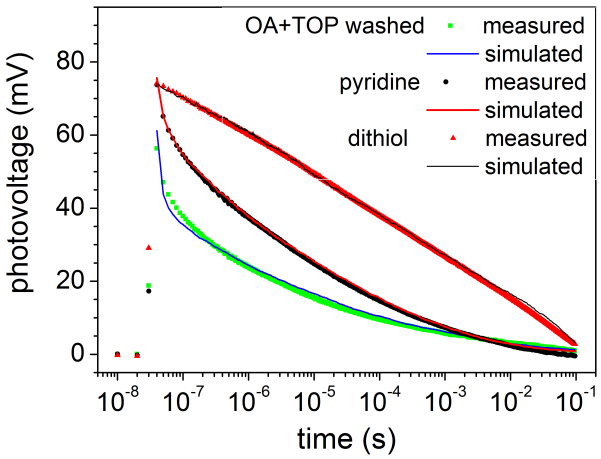

Figure 4.30: Measured and simulated transients of monolayers of CdSe QDs with varying surfactants.

The optimized parameters resulting from the fit are displayed in table 4.3. The ITO-QD distance decreased from 1.8 (OA+TOP washed) to 0.5 (pyridine) and 0.4 nm (dithiol) with ongoing ligand exchange. This agrees well with the change in interparticle distance measured with TEM (see figure 4.2). The distance between QD and ITO surface determined the probability of the final recombination of the hole and the electron on the ITO surface. Thus by decreasing the ITO-QD distance, the probability for the recombination of charge carriers was increased

and SVP transients became faster.

The number of trap states increased from 2 traps per QD, to 10 and 15 for OA+TOP, pyridine and dithiol surfactants, respectively. This result was in line with the decrease in radiative recombination measured by PL. The traps at the surface of QDs strongly influenced the relaxation behavior of charge carriers. Therefore the number of traps was a decisive parameter for the fit of SPV transients. Charge carriers recombined mainly by tunneling of the hole from the delocalized state into the ITO, and only to a minor rate by tunneling from the trap states into the ITO. The hole, which was trapped in a defect state at the beginning of the fit could either tunnel into another trap state, could be excited into the delocalized state or coukd recombine with the electron. If more trap states are available the probability for tunneling into another trap state is higher than the recombination or excitation into the delocalized state. Less holes recombined or were excited into the delocalized state. If the hole is excited into the delocalized state it could be either trapped on the surface, or recombine in the next step. The probability for trapping was increased with the number of trap states. Therefore a higher number of traps led to a longer lifetime of charge carriers and thus to longer transients.

	OA + TOP washed	pyridine	dithiol
number of traps	2	10	15
distance (nm)	1.8	0.5	0.4
effective dielectric constant	4.1	8.7	6.3
Fermi edge (eV)	-0.6	-0.6	-0.7

Table 4.3: Optimized parameters of simulated transients.

Transients of CdSe QD monolayers on could be well described by the single QD model and could be fitted with realistic parameters. The distance between QDs and ITO surface is in line with results from TEM measurements. The trend of an increasing number of traps correlated with PL quenching after ligand exchange. However one needs to be careful with the quantitative interpretation of the results as different solutions in terms of energy distributions and numbers of traps are possible. Yet the trend of an increase of traps with ligand exchange and the high influence of traps on charge carrier dynamics in CdSe QD layers is quite clear.

4.4 Charge separation in CdSe QD layer systems

In section 4.2 and 4.3 the mechanisms of charge separation and recombination in a CdSe QD layer were discussed. A central aspect was the contact to the substrate - the ITO - as charge separation was initiated by trapping of photo excited electrons on the ITO surface. In solar cells the separation of charges at interfaces and the transport into neighboring layers is crucial to collect charges at the contacts. Therefore the influence of different substrates on charge carrier dynamics and the separation of charges at different CdSe QD heterojunctions was studied.

4.4.1 Quenching of radiative recombination by different substrates

In figure 4.18 (page 75) PL quenching of the first monolayer of CdSe (pyridine) QDs by an ITO substrate was shown. Quenching of PL was explained in terms of a fast trapping of photo excited electrons from the first QD ML on the ITO surface. ITO is a highly doped (10^{20} - $10^{21}\,cm^{-3}$) n-conducting semiconductor. Due to its high doping its properties are metal like. Electrons can be trapped on the ITO surface. PL was also studied for CdSe (pyridine) QD layers on Si and SiO_2 (figure 4.31). The PL spectra of CdSe QD on Si (figure 4.31 b) resemble those on ITO (figure 4.31 a). Only a very small signal, being close to zero could be measured for the thinnest (1.3 ML thick) layer on Si. The highest signal was detected for the thickest (8.3 ML) QD layer. The signal decreased to approximately two third for the 6.9 ML thick sample. For the 4 ML thick sample a slightly higher signal was measured. Going to the 2.5 ML thick sample the PL signal was around one third than that of the 8.3 ML sample. The signal from the thinnest sample was around 3 percent of the highest signal and close to the noise level of the measurement. No signal from the Si substrate was present in this range.

CdSe QDs on SiO_2 showed a clear PL signal also for the thinnest layer (1.4 ML) studied (figure 4.31 c). The signal was distinctly higher than that of 1.6 ML and 1.3 ML on ITO and Si (see figure 4.31 d). It indeed was in the range of the signal measured for a 2 to 4 ML thick layer on ITO and Si. The highest signal on SiO_2 was detected for the 7.2 ML thick sample. The 8.4, 4.4 and 1.4 ML thick samples

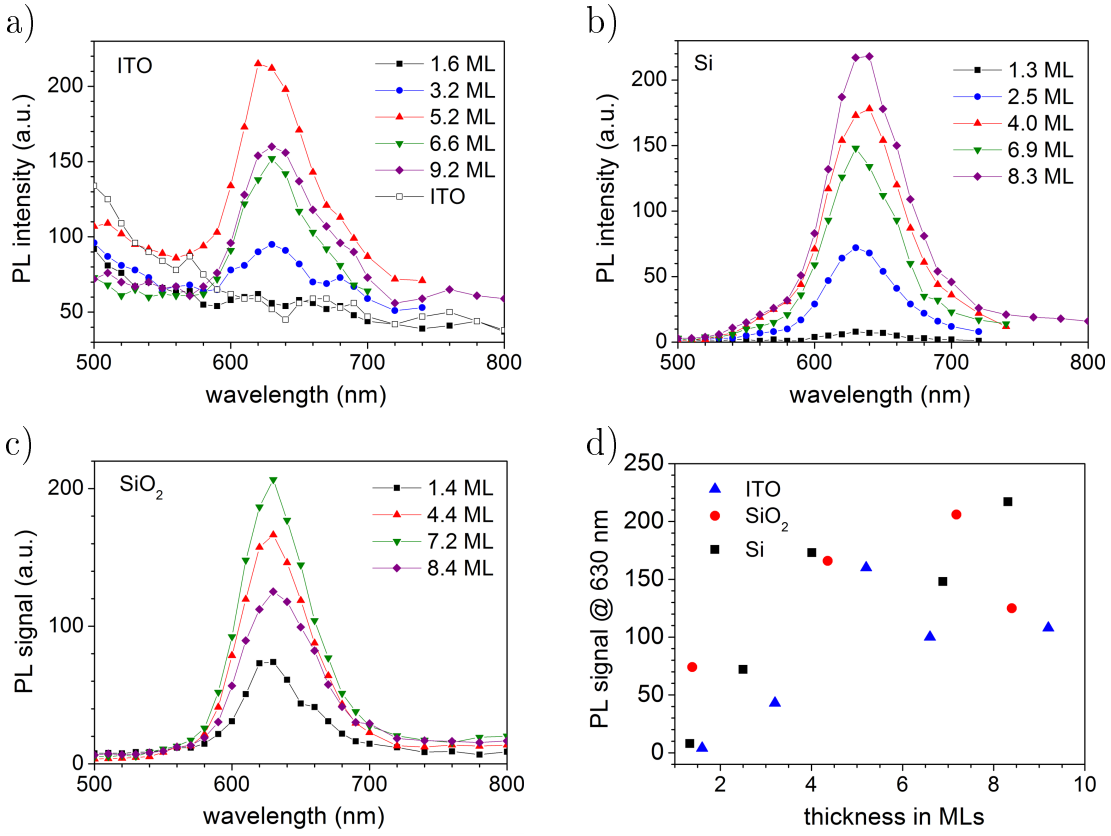

Figure 4.31: PL spectra of CdSe (pyridine) QD layers with varying thickness on (a) ITO (b) Si and (c) SiO_2, excited with a 337 nm laser pulse (see section 3.5); d) shows the dependence of the PL signal on the layer thickness. For the signals on ITO, the signal of the ITO substrate was subtracted. The spectra were not corrected by the transmission function of the optical system.

had signals of around 60 %, 80 % and 36 % compared to the highest signal. The thickness of CdSe QD layers was determined by RBS (on Si and SiO_2) and by a step profiler (on ITO). For details of determination of layer thicknesses see section 2.1.2.

Both Si and ITO caused quenching of PL from the first ML of CdSe QDs, whereas SiO_2 did not quench the PL signal. Therefore ITO and Si in contrast to SiO_2 had surface states which served as trap states (see figure 4.32). ITO being highly n-doped can be treated as a metal. Photo excited electrons can be trapped in unoccupied defect states which are below the energy of the first excitonic state of CdSe QDs. Si has a bandgap of 1.1 eV and unless it is strongly p-doped its valence band is lower in energy than the first excitonic state of CdSe QDs. Thus also in case of Si, electrons can be trapped on Si surface states or in the valence band of Si. SiO_2 has a band gap of 8.9 eV and therefore it is an insulator. The unfilled electronic states are far above the first excitonic state of CdSe QDs. Therefore no trapping of electrons on the SiO_2 takes place and the PL is not quenched. The quenching of PL is clearly dependent on the substrate and thus trapping of charge carriers is decisive for charge separation.

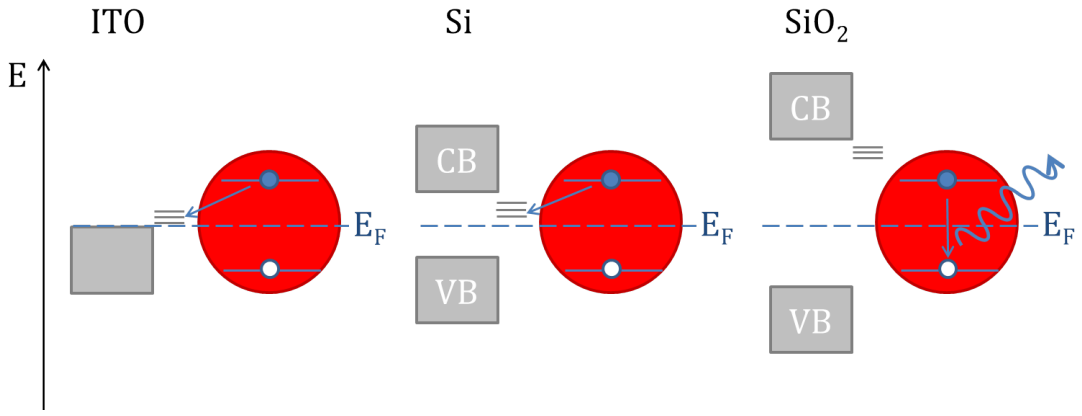

Figure 4.32: Model of quenching of PL from CdSe QDs due to ITO and Si and radiative recombination of charges in CdSe QDs on SiO_2.

4.4.2 Charge separation at the CdSe QD/CdS layer heterojunction

For an effective separation of charge carriers in a solar cell a charge selective contact is required. A charge selective contact was prepared by depositing CdSe QD layers on a CdS layer. The CdS layer had been prepared by a chemical bath deposition (CBD) process.[110] Separation of charge carriers across the CdSe-QD/CdS interface was studied by spectral SPV, both in the Kelvin and the fixed capacitor arrangement. The results of CdSe QD layers on CdS were compared with the measurements of CdSe QDs on ITO (see section 4.2 and 4.3).

Layers of CdSe QDs (pyridine) with varying thickness on CdS were prepared by dip coating (see section 3.2). Figure 4.33 shows the amplitude (a) and the phase (b) of SPV spectra measured with the fixed capacitor setup at a chopping frequency of 20 Hz. The CdS spectra had a maximum PV signal of 3.9 mV at 2.6 eV. The PV signal started around 1.5 eV and increased strongly around 2.2 eV. As CdS has a band gap of 2.4 eV[111] both tail states and deep defects were involved in the charge separation process.

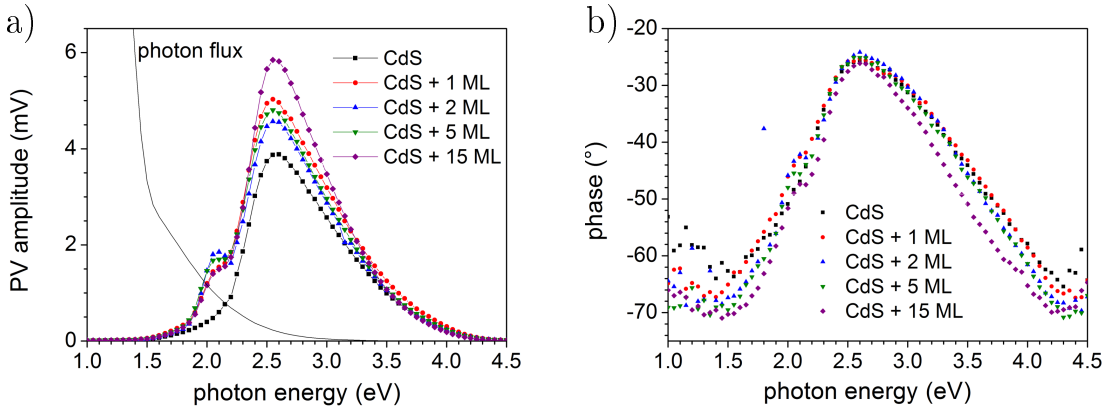

Figure 4.33: SPV spectra of CdSe (pyridine) QD layers with varying thicknesses on a CdS layer, measured with the fixed capacitor setup at a frequency of 20 Hz; a) shows the amplitude and b) the phase.

The layer of CdSe QDs on CdS generally increased the SPV signal. A maximum PV amplitude of 5.0, 4.6, 4.8 and 5.8 mV was measured for a 1, 2, 5 and 15 ML thick layer of CdSe QDs on CdS, respectively. No correlation between PV

amplitude and CdSe QD layer thickness could be found. Additionally to the increase in the overall SPV signal a shoulder around 2.1 eV, due to generation of photo-excited charge carriers in CdSe QDs appeared. The signal measured around 2.1 eV was between 1.5 and 1.9 mV for CdSe QDs on CdS. Again no correlation with CdSe QD layer thickness was observed.

The phase of the SPV measurement was between -70 and −25°. Therefore a separation of electrons towards the CdS and of holes towards the CdSe QDs was found (see section 3.3.2). As was also observed for CdSe QDs on ITO (figure 4.27) the phase increased with increasing PV amplitude. An increase from −63° (at 1.5 eV) to −24° (at 2.6 eV) was observed for the pure CdS layer. The CdSe QD/ CdS double layers had slightly lower phases, which decreased with increasing layer thickness. The effect was more pronounced in the regions where the PV amplitude was low.

In the sole CdS layer as well as in the double layer system electrons were separated towards the internal and holes towards the external surface. Therefore the CdS layer was, as would be expected an n-conductor with a positive band bending at the surface and holes were separated towards the external surface (see figure 4.34 a). The overall SPV signal increased when a CdSe QD layer was added onto the CdS layer. The increase of SPV signal could be explained in two ways. (i) More charge carriers were created as there were additional charge carriers created in the CdSe QDs and (ii) the charge separation length was increased due to the additional layer. A combination of both effects is most likely. The shoulder around 2 eV, which appeared in the CdSe QD/CdS double layers, was due to photo excited charge carriers in the CdSe QDs. Both the signal intensity of the shoulder and the general increase in PV amplitude could not be correlated with the QD layer thickness. What could be correlated with the CdSe QD layer thickness was the decrease in the phase. Separation and/or recombination of charge carriers became slower with increasing layer thickness.

The general increase in PV amplitude and the slower separation and/or recombination processes pointed towards a separation of charges over the CdSe QD/CdS interface. Holes created in the CdS layer were injected into the CdSe QD layer and electrons created in the CdSe QDs were injected into the CdS layer, a heterojunction was created. The conduction and the valence band in CdS was lower in energy

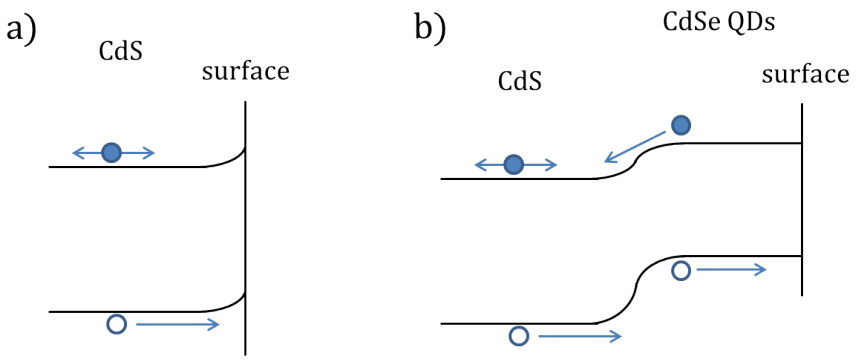

Figure 4.34: Scheme of energetic positions and charge separation in (a) the CdS layer and (b) the CdSe QD/CdS layer heterojunction.

than the first excitonic state and the ground state in CdSe QDs, respectively (see figure 4.34 b). Once charge carriers passed the interface the recombination process was slowed down. As already discussed for CdSe QDs on ITO initial charge separation, at short illumination times (0.05 s) only happened from the first monolayer, hence the independence of PV amplitude on CdSe QD layer thickness. Diffusion of holes from the CdS layer and CdSe QDs into the remaining top QD layers still took place, which resulted in a smaller phase for thicker QD layers.

Additional to the measurements with the fixed capacitor arrangement, SPV measurements with the Kelvin probe were performed. Unlike the fixed capacitor measurements, the Kelvin probe measurements are done at constant illumination and slow processes are monitored (see section 3.3.2). In figure 4.35 ΔCPD spectra and the SPV spectra derived from the ΔCPD spectra of CdSe QD layers on CdS are shown. The SPV signal is equal to the negative ΔCPD. The arrows at 0.7 eV in figure 4.35 indicate where the illumination of the samples started. The CPD signal at energies below 0.7 eV, thus shows the ΔCPD in the dark. The workfunction of the sample decreased between 200 and 300 mV when depositing CdSe QDs on the CdS layer (see figure 4.35 a). The change in work function could not be correlated with the thickness of the CdSe QD layer. Workfunctions of CdSe QDs on ITO (see figure 4.19 on page 76) were generally smaller than the workfunctions of CdSe QDs on CdS. Therefore no, or at least a weaker dipole was present in CdSe QDs on CdS compared to CdSe QDs on ITO.

The positive SPV signal showed separation of electrons towards the internal and holes towards the external surface for CdSe QD layers on CdS. Two peaks were

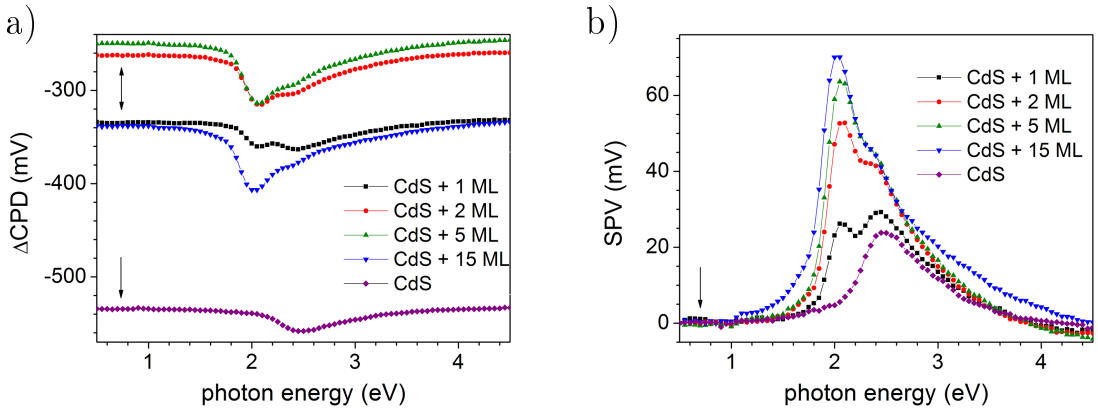

Figure 4.35: ΔCPD (a) and SPV (b) spectra of CdSe QD (pyridine) layers with varying thicknesses on CdS.

present in the spectra, one at 2.05 eV from charge carriers excited in CdSe QDs and one at 2.45 eV where the absorption in CdS became high. In contrast to modulated SPV measurements the spectra at constant illumination were dominated by charge separation at 2.05 eV and therefore by charge carriers excited in the CdSe QD layers . SPV signals measured at 2.05 eV were 6, 26, 53, 64 and 70 mV for CdS and CdS + 1 ML, 2 ML, 5 ML and 15 ML of CdSe QDs, respectively. The onset of the spectra was shifted to lower energies for thicker CdSe QD layers.

In figure 4.36 The PV signals at 2.05 eV are plotted against the QD layer thickness for QDs on CdS and ITO. The thickness dependence of PV signal on CdSe QD thickness on CdS becomes clear.

The influence of CdSe QDs in Kelvin probe measurements differs clearly from the measurements with the fixed capacitor arrangement. For CdSe QDs on CdS the ΔCPD signal, from charge carriers excited within the CdSe QDs dominated the spectra. This is opposite to what was observed by the fixed capacitor measurements, where electrons excited in the CdS layer dominated the spectra. Kelvin probe measurements were done under constant illumination at times > 10 s, whereas for the measurement with the fixed capacitor only modulated charge separation within the range of the 0.1 s was measured. Therefore charge separation from CdSe QDs dominates at constant illumination and long times, whereas charge separation from the CdS layer is faster and can be modulated within 0.1 s. The ΔCPD signal was also strongly dependent on layer thickness. Therefore

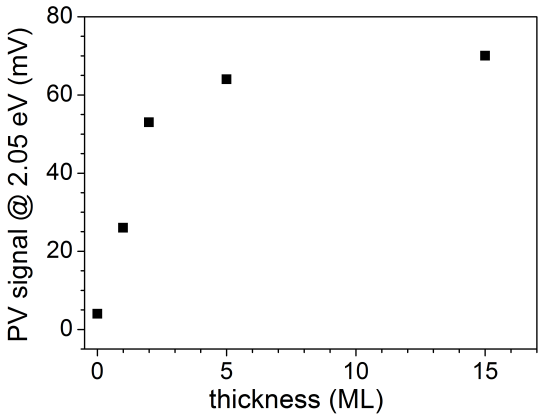

Figure 4.36: Correlation between Kelvin-Probe PV signal at 2.05 mV and CdSe QD layer thickness on CdS.

charge separation also took place in the upper CdSe QD layers. From figure 4.36 we can estimate a diffusion length of 2 to 3 ML. A CdSe QD/CdS layer heterojunction was created, where the CdS layer served as an electron acceptor and photo-excited electrons from the first 3 MLs of CdSe QDs were separated.

4.4.3 Charge separation at the CdSe QD/CdTe nanoparticle heterojunction

In the last section a CdSe QD/CdS layer heterojunction was formed for separation of charge carriers. In this section a heterojunction between two nanoparticle layers, CdSe QDs and CdTe nanoparticles (NPs), is formed. Parts of the results of this section were published by Zillner et al. in 2012.[112]

For the formation of a heterojunction CdSe (pyridine) QDs and CdTe NPs were used. The CdTe NPs were provided by Bayer Technonolgy Services and had a diameter of 8 nm. The surface treatment was equal to the surface treatment of CdSe (pyridine) QDs. The CdTe NPs were capped with pyridine molecules. The nanoparticle layers were prepared by electrophoretic deposition (EPD) from pyridine suspensions inside a glovebox. A volume of 1 mL suspension with a concentration between 0.075 and 0.175 mg/g was used for the deposition of NPs on SnO_2-F (FTO) and ITO. A NP layer with a thickness between 100 and 300 nm was formed, while the suspension was depleted of all nanoparticles. For details

about EPD see Zillner et al.[112] To see the effect of heat treatment some layers were annealed to 200 °C under nitrogen atmosphere.

To ascertain the formation of homogeneous, separated layers of nanoparticles cross sections of CdTe NPs and CdSe QDs layers were analyzed by TEM, SEM and energy-dispersive x-ray spectroscopy (EDX). Figure 4.37 a) shows a scanning electron microscope (SEM) image of a cross section of a CdTe NP layer on ITO, deposited from a solution with a concentration of 0.175 mg/g. The SEM layer thickness was 290 ± 20 nm. The CdTe NP layer in the TEM image in figure 4.37 b) was annealed at 200 °C. The particles were not sintered and still had a size of around 7 nm. TGA-MS measurements on pyridine capped CdSe QDs (figure 3.6, section 3.1.2) showed that the outer shell of pyridine surfactants is removed around 200 °C and therefore the surface and the distance between NPs is changed, during annealing.

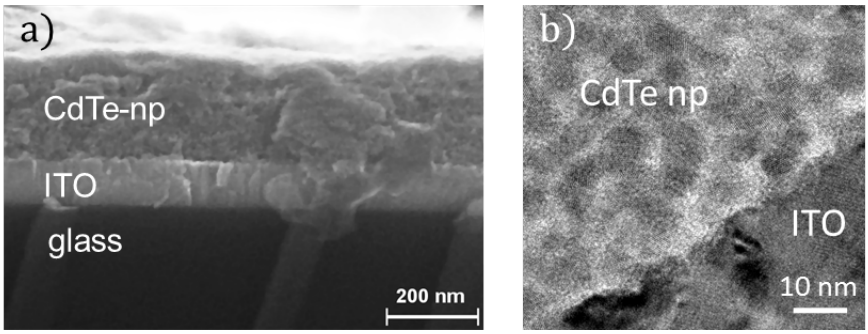

Figure 4.37: Cross sections of a CdTe nanoparticle layer deposited on ITO. a) Scanning electron microscopy image of an as deposited layer (accelerating voltage 18 kV, Zeiss, LEO 1530 GEMINI) and b) transmission electron microscopy image of a layer annealed at 200 °C (accelerating voltage 120 kV, Philips CM12/STEM, LaB6 kathode).

Intermixing of CdSe QDs and CdTe NPs in double layers was determined by EDX mapping and line scans. Figure 4.38 shows an EDX mapping and an EDX line scan of a CdTe NP/CdSe QD layer system, which was deposited via multiple EPD on a FTO substrate. Two consecutive EPDs, first with a suspension of CdTe NPs and second with a suspension of CdSe-NPs, were performed. For the EDX mapping the energy of the electron beam was 10 keV. A continuous cadmium signal was present over the CdTe NP and CdSe QD layers. The Se and Te signals showed a slight mixing of CdSe QDs and CdTe NPs at the interface, as well some

penetration of CdSe-QDs in the CdTe-NP layer. When the suspension for the second EPD is filled in the EPD cell, solving of already deposited CdTe NPs took place and led to some mixing of CdTe NPs and CdSe QDs. The carbon signal, observed in the CdTe NP and CdSe QD layers, is due to the organic surfactants on the NPs.

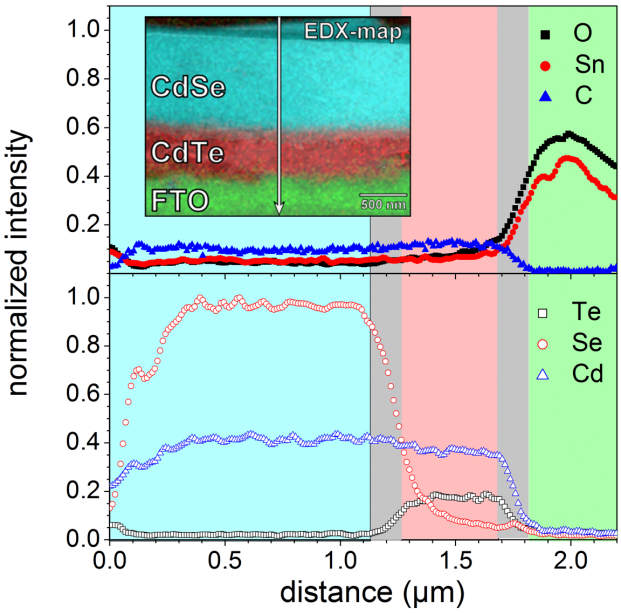

Figure 4.38: EDX measurements on a cross section of a CdTe NP/CdSe QD double layer on FTO: Element line scans of C K (blue triangles), O K (black squares), Sn L (red circles) and Se L (red circles), Cd L (blue triangles), and Te L (black squares) edges. The insert shows the element distributions of Se (blue), Te (red) and Sn (green) in the scanning electron microscopy cross section of the investigated sample (acceleration voltage of 7 kV).

Separation of charge carriers was measured by spectral dependent SPV under constant (Kelvin) and modulated (fixed capacitor) illumination. Figure 4.39 shows (i) ΔCPD and (ii) the SPV spectra, derived from the ΔCPD measurements of electrophoretically deposited nanoparticle layers. The CPD in the dark changed clearly due to annealing (figure 4.39 i). For CdSe QDs the CPD increased from -0.61 to −0.13 V and therefore a decrease in workfunction due to annealing was measured. The CPD of CdTe NPs decreased from 0.15 to −0.06 V and thus an increase in workfunction was observed. For the double layer one would expect the same values as measured for CdSe QDs and CdTe NPs for the CdTe NP/CdSe

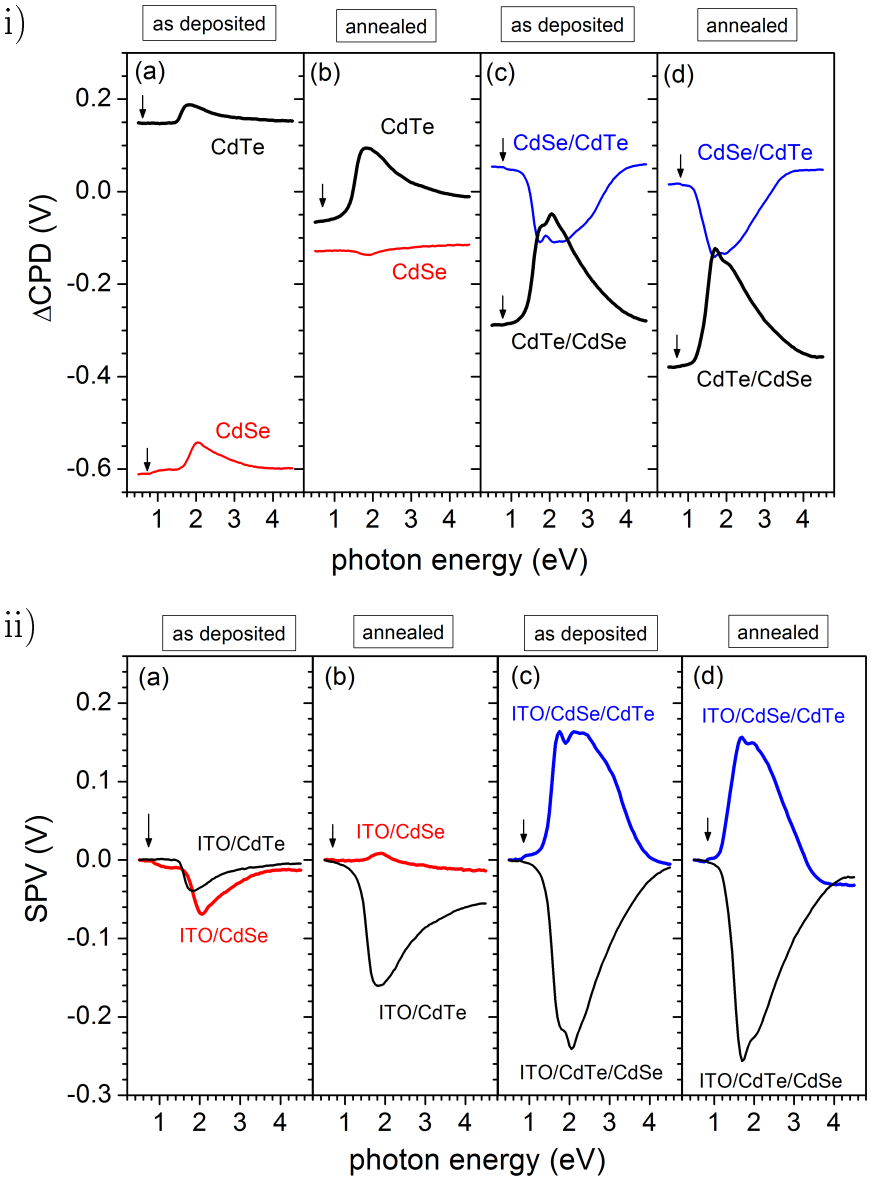

Figure 4.39: ΔCPD (i) and SPV (ii) spectra for single layers of CdTe NPs and CdSe QDs (black and red lines, respectively, in a and b) and for double layers of ITO/CdTe NPs/CdSe QDs and ITO/CdSe QDs/CdTe NPs (black and blue lines, respectively, in c and d) before (a, c) and after (b, d) annealing at 200 °C under N_2 inside the glove box. The arrows mark the photon energy at which the slit of the monochromator was opened.

QD and CdSe QD/CdTe NP double layers, respectively. The CPD of the pristine CdTe NP/CdSe QD double layer was −0.29 mV and therefore between the values measured for the pristine and the annealed CdSe QD layer. Heating of the double layer shifted the CPD only slightly to −0.38 V. The CPD for the pristine CdSe QD/CdTe NP layer was at 0.05 V and was shifted to 0.02 V due to heating. Both values were between the CPD of the pristine and annealed CdTe NP layer.

For the as deposited CdSe QD layer a positive ΔCPD and therefore a negative SPV signal was observed (figure 4.39 ii, a). A relative high signal below the band gap occurring from both, deep defect and tail states, was observed. The quality of the spectra is the same as the spectra of dip coated CdSe QD layers (see figure 4.35), yet the maximum signal of the EPD layer of 70 mV at 2.05 eV is clearly smaller than the maximum signal of dip coated samples, which varied between 120 and 170 mV. After annealing of the EPD layer a change in signal sign occurred for photon energies below 2.2 eV (figure 4.39 ii, b). Below 2.2 eV charge separation happens mainly from or into trap states. Thus the defect states on the CdSe QDs were changed by annealing, which influenced the whole spectrum.

For the pristine CdTe NP layer a relatively small positive signal, with a maximum of 40 mV at 1.8 eV, was observed (figure 4.39 ii, a). The ΔCPD signal started at photon energies above 1.5 eV, and thus above the band gap. No SPV signals induced by charge separation from defect states were detected. The ΔCPD signal increased by more than four times due to annealing at 200 °C (figure 4.39 ii, b). Additionally a signal below the band gap appeared. Therefore charge carriers from band gap states contributed to the SPV signal after annealing and led to an overall increase in the signal. For both, the CdSe QD and the CdTe NP sample, defect states influenced the separation of charges. Heating of the nanoparticle layers changed the surface of nanoparticles and the trap states.

For the CdTe NP/CdSe QD double layers similar spectra with inverted signs were measured for inverted stacking orders (figure 4.39 ii, c and d). Annealing did not change the ΔCPD spectra significantly at higher photon energies but increased the signal below the band gap (figure 4.39 ii, d). The mirror inverted signal pointed towards a dominating charge separation over the common CdTe NP/CdSe-QD interface. Further the SPV signal changed sign for the annealed ITO/CdSe QD/CdTe NP layer at photon energies above 3 eV. Therefore the exter-

nal surface of the CdTe NP layer became dominant at high absorption coefficients, when photons did not reach the CdSe QD/CdTe NP heterojunction.

The results of the Kelvin measurements show that a heterjunction between CdSe QDs and CdTe NPs was created. The CdSe QDs served as electron acceptor, the CdTe NPs as donors. Separation of charge carriers at constant illumination over the heterojunction was already dominating for pristine layers. Annealing of the layer did not change the mechanism of charge separation.

With Kelvin measurements the slow processes of charge separation at constant illumination are observed. Measuring of the same samples with the fixed capacitor under modulated illumination gives information about the fast processes. Figure 4.40 shows the X-signal and the phase of modulated SPV spectra. The as deposited CdSe QD layer on ITO had a negative X-signal with a maximum of 0.72 mV at 2.0 eV (figure 4.40 i, a). At energies above 2 eV the X-signal dropped rapidly and became positive for photon energies above 2.9 eV. No signal from deep defects was detected. In the region from 1.75 eV to 2.0 eV the phase increased from 100° to 155° showing a separation of electrons towards the external surface, which became faster with increasing photon energy (figure 4.40 ii, a). Between 2.0 eV and 3.0 eV the phase dropped to −90° showing a change from fast charge separation of electrons towards the external surface to slow separation of electrons towards the internal surface.

After annealing of the CdSe QD layer, the X-signal became positive in the complete measurement range (figure 4.40 i, b). Both, the X-signal and the phase, resembled the spectra measured at dip coated CdSe QD layers (see figure 4.17, page 73). A maximum signal of 1.4 mV was detected at 2.0 eV. In the range from 1.2 eV to 2.0 eV the phase increased from −80° to −33° and therefore charge separation of electrons towards the interface became faster (figure 4.40 ii, b).

CdTe NPs on ITO had a negative X-signal before and after annealing (figure 4.40 i, a and b). The spectra before and after annealing were quite similar. The SPV onset was at 1.45 eV, no contribution of deep defects was measured. Both CdTe NP layers had a maximum at 1.7 eV of -0.37 and −0.32 mV for the pristine and the annealed sample, respectively. The non annealed sample had an additional peak at 2.0 eV and a higher X-signal for photon energies above 1.6 eV. The phase increased for photon energy between 1.45 and 1.7 eV for both layers, showing a

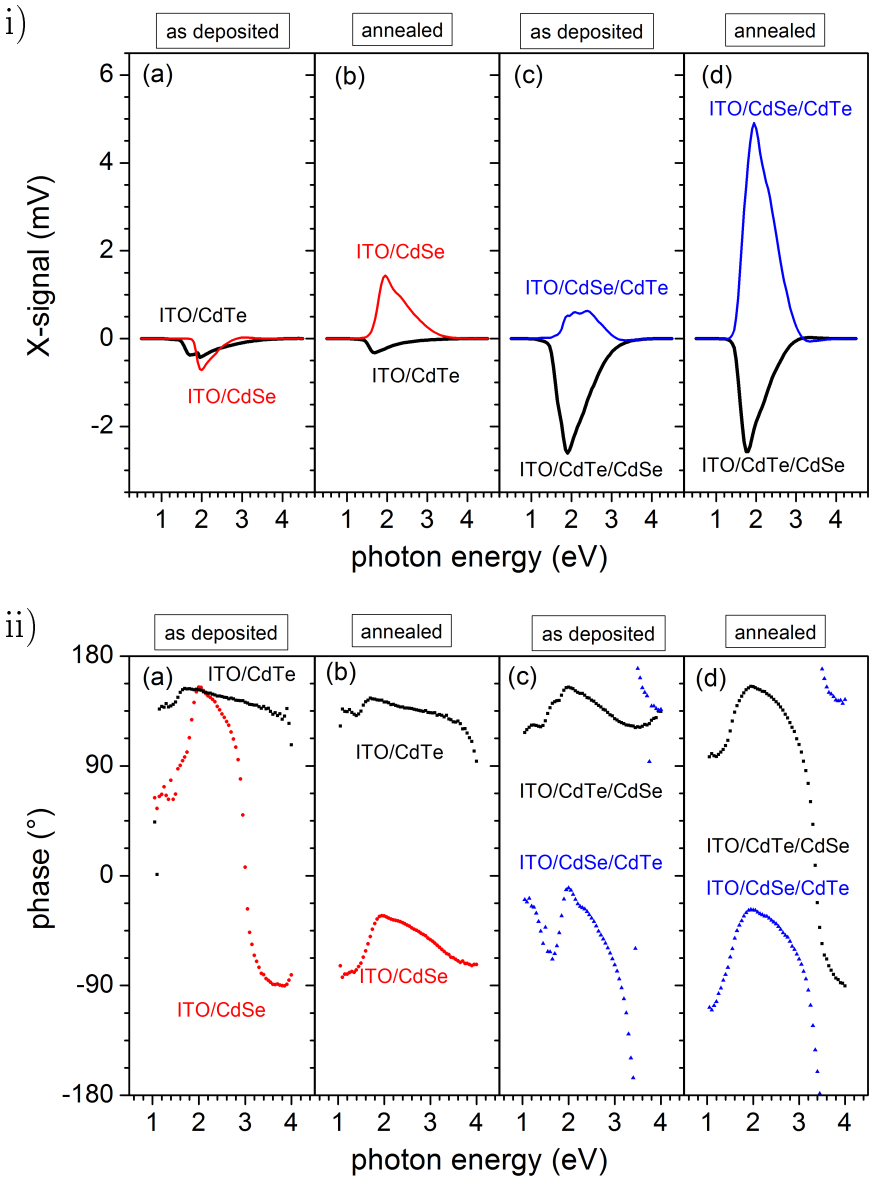

Figure 4.40: X-signal (i) and phase (ii) of SPV spectra for single layers of CdTe NPs and CdSe QDs (black and red lines, respectively, in a and b) and for double layers of ITO/CdTe NPs/CdSe QDs and ITO/CdSe QDs/CdTe NPs (black and blue lines, respectively, in c and d) before (a, c) and after (b, d) annealing at 200 °C under N_2 inside the glove box. The spectra were measured at a chopping frequency of 20 Hz

faster charge separation at higher SPV signals. Charge separation in the annealed sample was slightly slower (figure 4.40 ii, a and b).

For the CdSe QD/CdTe NP double layer a clear change in the spectra due to annealing took place (figure 4.40 i, c and d). In the region below 1.7 eV, where only the CdTe NPs absorbed, the X-signal of the pristine sample was smaller than 0.1 mV and the phase decreased in this region. At photon energies above 1.7 eV where the CdSe QDs started to absorb the X-signal and the phase increased strongly (figure 4.40 ii, c and d). The X-signal became negative for photon energies above 3.2 eV. Annealing increased the X-signal in the complete measurement range. The maximum X-signals were 0.6 mV at 2.4 eV and 4.9 mV at 2.0 eV for the pristine and annealed sample, respectively. A clear signal was also detected for photon energies below 1.7 eV, where only the CdTe NPs absorbed the light.

The SPV spectra of the CdTe NP/CdSe QD layers had a negative X-signal (figure 4.40 i, c and d). The maximum X-signal of the pristine layer was −2.6 mV and was located at 1.9 eV. The onset of the SPV signal was around 1.45 eV. Annealing of the layer led to a shift of the maximum to 1.8 eV and positive X-signals at photon energies above 3.1 eV (figure 4.40 i, d). The phase of the pristine and the annealed sample was equal between 1.5 and 2.6 eV (figure 4.40 ii, c and d). For energies above 2.6 eV the phase of the annealed sample decreased strongly to a value of −90° at 4 eV (figure 4.40 ii, d).

The annealed double layers showed mirror inverted X-signals (figure 4.40 i, d). The X-signal of the CdSe QD/CdTe NP double layer was nearly twice that of the CdTe NP/CdSe QD sample. The phase of the layers was shifted by 180° but otherwise equal for both samples (figure 4.40 ii, d). Therefore equal mechanisms of charge separation took place, only in the opposite direction. Therefore charge carriers were separated over the CdTe/CdSe interface, a CdTe NP/CdSe QD heterojunction was created. The CdSe QDs acted as electron acceptors, whereas the CdTe NPs acted as electron donors.

Measurements with the fixed capacitor give results similar to Kelvin probe measurements. Both measurements show dominant separation of charge carriers over the heterocontact between CdTe NPs and CdSe QDs. However charge separation over this interface was slow for pristine layers and was therefore only dominating in Kelvin probe measurements. After annealing charge separation over the interface

became faster and dominated in both measurements. The formation of a CdTe NP/CdSe QD heterojunction with CdSe QDs as electron acceptors and CdTe NPs as electron donors is in accordance with the description of a charge selective NP heterojunction by Gur et al.[113] Figure 4.41 shows an energy diagram which illustrates the charge separation processes as derived during SPV measurements.[113]

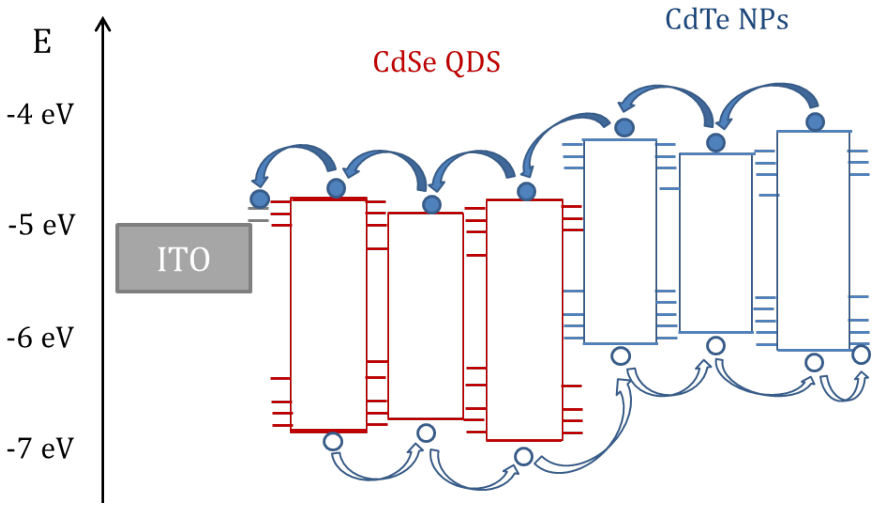

Figure 4.41: Energy diagram of the ITO/CdSe/CdTe heterojunction to illustrate charge separation processes as derived from SPV measurements. (The work function of the ITO depends strongly on surface treatment[114,115] and therefore remains unclear.)

In addition charge separation at the interface with the ITO and the external surface could not be excluded and probably caused the difference in the SPV amplitudes for different layer ordering. For the Kelvin probe measurements the CdTe NP/CdSe QD heterojunction was already dominating without annealing, whereas for the fixed capacitor measurements annealing was necessary. Thus the separation over the heterojunction was slow for the pristine samples and became faster for annealed double layers.

5 Summary and Outlook

In this thesis charge separation and recombination processes in CdSe QD thin films and the influence of surface modifications and substrates were studied. Thin films of CdSe QDs were prepared by dip-coating under an inert atmosphere. Values for the areal density, the absorption coefficient and the thickness, measured by step profiler and SEM cross sections for a monolayer of CdSe QDs, were determined. Therefore the thickness of CdSe QD layers could be measured with different methods and was controlled.

Modulated and transient SPV measurements on CdSe (pyridine) QD layers on ITO showed that initial charge separation took place within the first monolayer of QDs. Electrons excited in the first monolayer were trapped on the ITO surface within a nanosecond, as PL from this layer was completely quenched. Charge carriers in the remaining layers of QDs recombined without directed charge separation. The SPV signal was linearly dependent on the absorbed photon density for densities up to $10^{12}\,\mathrm{cm}^{-2}$. For higher photon densities the ratio between SPV signal and photon density was decreasing with increasing photon density. The maximum SPV signal measured was around 100 mV. The ratio between SPV signal and photon density started to decrease at a value where the probability for more than one excited charge carrier pair per QD became high, which is the condition for the onset of Auger recombination. Auger recombination limited the number of electrons which were trapped on the ITO surface as it takes place in the ps range. Assuming a charge separation length of 3 nm (initial charge separation only in the first monolayer) a density of separated charge carriers in the range of $10^{12}\,\mathrm{cm}^{-2}$ was found. As a density of 4.5×10^{12} QDs per cm^2 was present charge separation happened in about 20 % to 25 % of the QDs in the first monolayer of QDs.

SPV transients of thicker CdSe QD layers had a slower decay than SPV transients

of the ML. Thus the free holes which remained in the QDs of the first monolayer partially diffused into neighboring QD layers. The long decay times, which were in the range of ms, also pointed towards trapping of holes.

At constant illumination the sign of the SPV signal , measured with the Kelvin probe setup changed, pointing towards a separation of electrons towards the external surface. This process dominated as charge carriers were accumulated and trap states were filled.

By exchange of surfactants, both the distance between QDs in layers and the passivation of defects, was varied. SEM images showed a decrease of interparticle distance (between QD centers) from (7.7±0.2)nm, to (6.2±0.2)nm, (5.6±0.3)nm and (5.5±0.4)nm due to washing, ligand exchange with pyridine and dithiol. At the same time a decrease in PL intensity, indicating an increase of trap states due to surface modifications, was measured. Low temperature PL measurements additionally show a shift of the surface peak from $\approx$ 1.3 eV to $\approx$ 1.7 eV after ligand exchange with pyridine and dithiol. Therefore trap states were created due to the π-ring of the ligands and the sulfur bond of the dithiol. While the PL intensity decreased an increase in SPV signal due to surface modifications was measured. For the pristine QDs, characterized with a thick surfactant shell and a low number of defects, no SPV signal was detected. For the remaining QDs the amplitude of SPV transients was only weakly dependent on the surfactant, but the decay times strongly increased. Initial charge separation took place only in the first monolayer of CdSe QDs, independent of surface modification. However the decay time increased with an increasing number of trap states and decreasing QD-ITO distance.

The single QD approximation model was developed to describe the recombination of separated charge carriers in a monolayer of CdSe QDs on ITO. The model is based on Miller-Abrahams tunneling of holes into defect states on the QD surface, the delocalized state of the QD and the filled state on the ITO surface. The simulation describes the relaxation of a hole trapped at the QD surface towards a fixed electron at the ITO surface. By fitting SPV transients of CdSe QD monolayers information about trap density and ITO-QD distance were obtained, which were in line with PL and TEM measurements. The separation and recombination of charges was dominated by trap states. A higher number of trap states increased

the probability of tunneling from a trap state towards another trap states. Therefore charge carriers took longer to recombine and decay times of SPV transients increased.

PL measurements of CdSe QDs on varying substrates were measured to determine the influence of the substrate on charge carrier separation. The measurements revealed quenching of recombination from the first monolayer if CdSe QDs were deposited onto ITO and Si. However quenching was not detected if the QDs were deposited on SiO_2, where no trap states for photo-excited electrons were available. Therefore trap states on the surface of the substrate are decisive for the separation of charge carriers.

By deposition of CdSe QDs on a CdS layer a CdSe QD/CdS heterojunction was created. Electrons excited in CdSe QDs were injected into CdS and hole excited in the CdS layer were injected into CdSe QDs. The separation of charges over the interface led to a slower recombination of separated charge carriers. The SPV sign stayed positive for Kelvin probe measurements and therefore also under constant illumination injection of electrons into the CdS layer was still the dominating process. As the CdS layers served as an electron acceptor a direct dependence of SPV signal on CdS layer thickness was found. The carrier diffusion length in CdSe QDs was in the range of 2 to 3 ML.

A CdSe QD/CdTe nanoparticle heterojunction was created by successive electrophoretic deposition of CdSe QDs and CdTe nanoparticles. CdTe NPs served as electrons donors and CdSe QDs as electron acceptors. A mirror inverted SPV signal was detected after annealing at 200 °C for inverted stacking of CdSe QDs and CdTe nanoparticles for measurements under constant and modulated illumination. Therefore charge separation was dominated by the CdSe QD/CdTe interface.

The results show that extraction of charge carriers from CdSe QD is possible if the thick surfactant shell from the synthesis is exchanged. However pyridine and dithiol capped CdSe QDs were characterized by a high density of defects leading to charge carrier trapping. The effectiveness of charge carrier extraction from trapped charge carriers is under debate. At the CdSe QD/CdS heterojunction exciton diffusion length in the range of 2 to 3 ML were found and a CdSe QD/CdTe nanoparticle heterojunction was realized. Taking these results into account a solar

cell with these CdSe QDs as absorbers should not have a layer thickness of more than 2 to 3 MLs of CdSe QD. For reaching a reasonable absorption a charge selective contact with a high surface area is required. This could be for example a porous layer of CdTe nanoparticles. Also a blend of CdSe QDs and CdTe nanoparticles is imaginable. Another approach would be the deposition of CdSe QDs on highly porous wide band gap semiconductors like TiO_2 or nanorods for example from ZnO serving as the heterocontact. To enable the use of thicker CdSe QD layers a higher exciton diffusion length is required. This could be possibly achieved by a better passivation of surface defects.

List of Abbreviations, Constants and Symbols

abbreviation	**description**
ac	alternating current
BTS	Bayer Technology Services
CB	conduction band
CPD	contact potential difference
C_{60}	fullerene
dc	direct current
dithiol	1-4-benzenedithiol
EDX	energy-dispersive X-ray spectroscopy
EPD	electrophoretic deposition
FF	fill factor
FTO	fluorine-doped tin oxide
FWHM	full width at half maximum
HOMO	highest occupied molecular orbital
ITO	indium tin oxide
LUMO	lowest unoccupied molecular orbital
ML	monolayer
NG3	neutral density filter with fraction transmission of $\approx 10^{-2}$
NG4	neutral density filter with fraction transmission of $\approx 10^{-1}$
NP	nanoparticle
OA	oleic acid
PCP-DTBT	poly[2,6-(4,4-bis-(2-ethylhexyl)-4H-cyclopental[2,1-b;3,4-b‘]-dithiophene)-alt-4,7-(2,1,3-benzothiadiazole)]
PL	photo luminescence

abbreviation	**description**
PV	photovoltage
P3HT	Poly(3-hexylthiophen)
QD	quantum dot
RBS	Rutherford-Backscattering Spectrometry
SEM	scanning electron spectroscopy
SPV	surface photovoltage
TEM	transmission electron spectroscopy
TGA-MS	thermo-gravimetric analysis with mass spectrometry
ToF-MS	time of flight mass spectrometry
TOP	trioctylphosphine
TOPO	trioctylphosphine oxide
UV-vis	ultraviolet-visible
VB	valence band
0D	0-dimensional
1D	1-dimensional
2D	2-dimensional
3D	3-dimensional

constant	**value**	**description**
d_{cp}	$\pi/3\sqrt{2}$	space filling of closed packed spheres
e	$1.602\,176\,565 \times 10^{-19}\,\mathrm{c}$	elementary charge
ε_0	$8.854 \times 10^{-12}\,\mathrm{As/Vm}$	dielectric constant of vacuum
g	$6.673\,84 \times 10^{-11}\,\mathrm{N(m/kg)^2}$	gravity constant
h	$4.135\,667\,516 \times 10^{-15}\,\mathrm{eVs}$	Planck constant
$\hbar$	$6.582\,119\,28 \times 10^{-16}\,\mathrm{eVs}$	reduced Planck constant
k_B	$8.617\,332\,4 \times 10^{-5}\,\mathrm{eV/K}$	Boltzmann constant
N_A	$6.002 \times 10^{23}\,\mathrm{mol}^{-1}$	Avogadro constant
u	$1.660\,538\,921 \times 10^{-17}\,\mathrm{kg}$	atomic mass

symbol	**unit**	**description**
A		absorption in context with UV-vis
A	cm^2	area

symbol	unit	description
AD	$1/cm^2$	areal density
α	$1/cm$	absorption coefficient in context with UV-vis spectroscopy
α	$1/nm$	inverse tunneling length in context with Miller-Abrahams tunneling
c	M / mg/g	concentration
C	$farad$	capacitance
ch		channel
γ	N/m	surface tension
Γ	s^{-1}	tunneling rate
d	nm	diameter
D	nm	layer thickness
δ	cm^{-2}	absorbed photon density
δ_i		volume fraction
E	eV	Energy
E_A	eV	activation energy
E_B	eV	energy of the barrier
$E_{Coulomb}$	eV	Coulomb energy
E_F	eV	Fermi Energy
E_{gap}	eV	energy of the band gap
E_{kin}	eV	kinetic energy
E_{Sol}	eV	solvation energy
ε	8.854×10^{-12} As/Vm	relative dielectric constant
θ	Rad	polar angle in quantum mechanics
θ	Rad	backscattering angle in RBS
j		Bessel function
K		kinematic factor
k_{DA}	s^{-1}	rate of electronic energy transfer (Förster transfer)
l		orbital quantum number
λ	nm	wavelength
λ	eV	reorganization energy in context with Marcus Theory

symbol	unit	description
m		orbital magnetic quantum number
m_e	9.11×10^{-31} kg	effective electron mass
m_h	9.11×10^{-31} kg	effective hole mass
M	g/mol	atomic mass
η	$kg/(s \cdot m)$	viscosity
φ	Rad	azimuth angle
Q	cm^{-2}	density of charges
R		reflection in context with UV-vis
R	nm	width of the barrier in context with electron transport
R_0	nm	Förster distance
R_{DA}	nm	distance between donor and acceptor (Förster transfer)
ρ	g/cm^3	density
S	$keV/\mu m$	stopping power
σ	10^{-27} cm^2/sr	Rutherford cross section
T		transmission in context with UV-vis
T	K	temperature
τ^{-1}	s^{-1}	tunneling rate
τ_D	s	lifetime of donor (Förster transfer)
U	J	potential energy
V	nm^3	volume
V_{OC}	V	open circuit voltage
V_S	mV	surface photovoltage signal
υ	m/s	withdrawal speed
W	eV	work function
Y_{lm}		spherical function
Ω	Rad	solid angle in RBS
$\triangle$		Laplace operator

Bibliography

[1] Tao, C. S.; Jiang, J.; Tao, M. *Solar Energy Materials & Solar Cells*, **2011**, *95*, 3176–3180.

[2] US Department of Energy, Basic Research Needs for Solar Energy Utilization, 2005, p. 3.

[3] Hoffert, M.; Caldeira, K.; Jain, A.; Haites, E.; Harvey, L.; Potter, S.; Schlesinger, M.; Schneider, S.; Watts, R.; Wigley, T.; Wuebbles, D. *Nature*, **1998**, *395*, 881–884.

[4] Wadia, C.; Alivisatos, A. P.; Kammen, D. *Environ. Sci. Tehcnol.*, **2009**, *43*, 2072–2007.

[5] Alivisatos, A. P. *Science*, **1996**, *271*, 933–937.

[6] Nozik, A. J.; Beard, M. C.; Luther, J. M.; Law, M.; Ellingson, R. J.; Johnson, J. C. *Chem. Rev.*, **2010**, *110*, 6873–6890.

[7] Semonin, O. E.; Luther, J. M.; Choi, S.; Chen, H.-Y.; Gao, J.; Nozik, A. J.; Beard, M. C. *Science*, **2010**, *334*, 1530–1533.

[8] Tisdale, W. A.; Williams, K. J.; Timp, B. A.; Norris, D. J.; Aydil, E. S.; Zhu, X.-Y. *Science*, **2010**, *328*, 1543–1547.

[9] Shokley, W.; Queisser, H. J. *J. Appl. Phys.*, **1961**, *32*, 510–519.

[10] Pattantyus-Abraham, A. G.; Kramer, I. J.; Barkhouse, A. R.; anf G. Konstantatos, X. W.; Debnath, R.; Levina, L.; Raabe, I.; Nazeeruddin, M. K.; Grätzel, M.; Sargent., E. H. *ACS Nano.*, **2010**, *4*, 3374–3380.

[11] Skompska, M. *Synthetic Metals*, **2010**, *160*, 1–15.

[12] Luther, J. M.; Law, M.; Beard, M. C.; Song, Q.; Reese, M. O.; Ellingson, R. J.; Nozik., A. J. *Nano Lett.*, **2008**, *8*, 3488–3492.

[13] Ma, W.; Luther, J. M.; Zheng, H.; Wu, Y.; Alivisatos., A. P. *Nano Lett.*, **2009**, *9*, 1699–1703.

[14] Choi, J. J.; Lim, Y.; Santiaho-Berrios, M. B.; Oh, M.; Hyun, B.; Sun, L.; Bartnik, A. C.; Goedhart, A.; Malliaras, G. G.; Abruña, H. D.; Wise, F. H.; Hanrath, T. *Nano Lett.*, **2009**, *9*, 3749–3755.

[15] Leschkies, K. S.; Beatty, T. J.; Kang, M. S.; Norris, D. J.; Aydil, E. S. *ACS Nano*, **2009**, *3*, 3638–3648.

[16] Johnston, K. W.; Pattantyus-Abraham, A. G.; Clifford, J. P.; Myrskog, S. H.; MacNeil, D. D.; Levina, L.; Sargent, E. H. *Appl. Phys. Lett.*, **2008**, *92*, 151115.

[17] Klem, E. J. D.; MacNeil, D. D.; Cyr, P. W.; Levina, L.; Sargent, E. H. *Appl. Phys. Lett.*, **2007**, *90*, 183113.

[18] Koleilat, G. I.; Levina, L.; Shukla, H.; Myrskog, S. H.; Hinds, S.; A. G, P.-A.; Sargent, E. H. *ACS Nano*, **2008**, *2*, 833–840.

[19] Debnath, R.; Tang, J.; Barkhouse, D. A.; Wang, X.; A. G, P.-A.; Brzozwski, L.; Levina, L.; Sargent, E. H. *J. Am. Chem. Soc*, **2010**, *132*, 5952–5953.

[20] Szendrei, K.; Gomulya, W.; Yarema, M.; Heiss, W.; Loi, M. A. *Appl. Phys. Lett.*, **2010**, *97*, 203501.

[21] Barkhouse, A. R.; Debnath, R.; Kramer, I. J.; Zhitomirsky, D.; Pattantyus-Abraham, A. G.; Levina, L.; Etgar, L.; Grätzel, M.; Sargent., E. H. *Advanced Materials*, **2011**, *23*, 3134–3138.

[22] Ip, A. H.; Thon, S. M.; Hoogland, S.; Voznyy, O.; Zhitomirsky, D.; Debnath, R.; Levina, L.; Rollny, L. R.; Carey, G. H.; Fischer, A.; Kemp, K. W.; Kramer, I. J.; Ning, Z.; Labelle, A. J.; Chou, K. W.; Amassian, A.; Sargent, E. H. *Nat. Nanotech. Lett.*, **2012**, *7*, 577–582.

[23] Gao, J.; Perkins, C. L.; Luther, J. M.; Hanna, M. C.; Chen, H.-Y.; Semonin, O. E.; Nozik, A. J.; Ellingson, R. J.; Beard, M. C. *Nano Lett.*, **2011**, *5*, 3263–3266.

[24] Kramer, I. J.; Zhitomirsky, D.; Bass, J. D.; Rice, P. M.; Topuria, T.; Krupp, L.; Thon, S. M.; Ip, A. H.; Debnath, R.; Kim, H.-C.; Sargent, E. H. *Adv. Mater.*, **2012**, *24*, 2315–2319.

[25] Liu, H.; Zhitomirsky, D.; Hoogland, S.; Tang, J.; Kramer, I. J.; Ning, Z.; Sargent, E. H. *Appl. Phys. Lett.*, **2012**, *101*, 151112.

[26] Tang, J.; Liu, H.; Zhitomirsky, D.; Hoogland, S.; Wang, X.; Furukawa, M.;

Levinab, L.; Sargent, E. H. *Nano. Lett.*, **2012**, *12*, 4889–4894.

[27] Hardin, B. E.; Snaith, H. J.; McGehee, M. D. *nature photonics*, **2012**, *6*, 162–169.

[28] Benehkohal, N. P.; González-Pedro, V.; Boix, P. P.; Chavhan, S.; Tena-Zaera, R.; Demopoulos, G. P.; Mora-Seró, I. *J. Phys. Chem. C*, **2010**, *116*, 16391–16397.

[29] Tachan, Z.; Shalom, M.; Hod, I.; Rühle, S.; Tirosh, S.; Zaban, A. *J. Phys. Chem. C*, **2010**, *15*, 6162–6166.

[30] Jovanovski, V.; González-Pedro, V.; Giménez, S.; Azaceta, E.; Cabañero, G.; Grande, H.; Tena-Zaera, R.; Mora-Seró, I.; Bisquert, J. *J. Am. Chem. Soc.*, **2011**, *133*, 20156–20159.

[31] Li, L.; Yang, X.; Gao, J.; Tian, H.; Zhao, J.; Hagfeldt, A.; Sun, L. *J. Am. Chem. Soc.*, **2011**, *133*, 8458–8460.

[32] Salant, A.; Shalom, M.; Tachan, Z.; Buhbut, S.; Zaban, A.; Banin, U. *Nano Lett.*, **2012**, *12*, 2095–2100.

[33] Celik, D.; Krueger, M.; Veit, C.; Schleiermacher, H. F.; Zimmermann, B.; Allard, S.; Dumsch, I.; Scherf, U.; Rauscher, F.; Niyamakom, P. *Sol. Energy Mater. Sol. Cells*, **2012**, *98*, 433–440.

[34] Dayal, S.; Kopidakis, N.; Olson, D. C.; Ginley, D. S.; Rumbles, G. *Nano Lett.*, **2010**, *10*, 239–242.

[35] Huynh, W. U.; Dittmer, J. J.; Alivisatos, A. P. *Science*, **2002**, *295*, 2425–2427.

[36] Radychev, N.; Lokteva, I.; Witt, F.; Kolny-Olesiak, J.; Borchert, H.; Parisi, J. *J. Phys. Chem. C*, **2011**, *115*, 14111–14122.

[37] Gur, I.; Fromer, N. A.; Chen, C.-P.; Kanaras, A. G.; Alivisatos, A. P. *Nano Lett.*, **2007**, *7*, 409–414.

[38] Gyot-Sionnest, P.; Wang, C. *J. Phys. Chem B*, **2003**, *107*, 7355–7359.

[39] Yu, D.; Wang, C.; Guyot-Sionnest, P. *Science*, **2003**, *300*, 1277–1280.

[40] Zhang, S.; Cyr, P. W.; McDonald, S. A.; Konstantatos, G.; Sargent, E. H. *Appl. Phys. Lett.*, **2005**, *87*, 233101.

[41] Jeong, K. S.; Tang, J.; Liu, H.; Kim, J.; Schaefer, A. W.; Kemp, K.; Levina,

L.; Wang, X.; Hoogland, S.; Debnath, R.; Brzozowski, L.; Sargent, E. H.; Asbury, J. B. *ACS Nano*, **2012**, *6*, 89–99.

[42] Gross, D.; Mora-Sero, I.; Dittrich, T.; Belaidi, A.; Mauser, C.; Houtepen, A. J.; Como, E. D.; Rogach, A. L.; Feldmann, J. *J. Am. Chem. Soc.*, **2010**, *132*, 5981–1983.

[43] Feynmann, R. There is plenty of room at the bottom. talk, 1959. Annual meeting of the American Physical Society at the California Insitute of Technology.

[44] Alivisatos, A. P. *Journal of Physical Chemistry*, **1996**, *100*, 13226–13239.

[45] Choi, C. L.; Alivisatos, A. P. *Annu. Rev. Phys. Chem.*, **2010**, *61*, 369–389.

[46] Mitrin, V. V.; Sementsov, D. I.; Vagidov, N. Z. *Quantum Mechanics for Nanotructures.* Cambridge University Press, Cambridge, 2010.

[47] Brus, L. E. *J. Chem. Phys.*, **1984**, *80*, 4403–4409.

[48] Kim, B. S.; Islam, M. A.; Brus, L. E.; Herman, I. P. *J. Appl. Phys.*, **1984**, *89*, 8127–8140.

[49] Blachnik, R.; Chu, J.; Galazka, R. R.; Geurts, J.; Gutowski, J.; Hönerlage, B.; Hofmann, D.; Kossut, J.; Lèvy, R.; Michler, P.; Neukirch, U.; Strauch, D.; Story, T.; Waag, A. *Landolt-Börnstein: Group III: Condensed Matter, Volume41 Semiconductors, Subvolume B, II - VI and III - V Compounds, Semimagnetic compounds.* Springer- Verlag, Berlin, Heidelberg, New York, 1999.

[50] Norris, D.; Bawendi, M. G. *Phys. Rev. B*, **2010**, *53*, 16338–16346.

[51] Jasieniak, J.; Smith, L.; van Embden, J.; Mulvaney, P. *J. Phys. Chem. C*, **2009**, *113*, 19468–19474.

[52] Yu, W. W.; Qu, L.; Guo, W.; Peng, X. *Chem. Mater.*, **2003**, *15*, 2854.

[53] Leatherdale, C. A.; Woo, W. K.; Mikulec, F. V.; Bawendi, M. G. *J. Phys. Chem. B*, **2002**, *106*, 7619.

[54] Choi, J.-H.; Fafarman, A. T.; Oh, S. J.; Ko, D.-K.; Kim, D. K.; Diroll, B. T.; Muramoto, S.; Gillen, J. G.; Murray, C. B.; Kagan, C. R. *Nano Lett.*, **2012**, *12*, 2631–1638.

[55] Lefrançois, A.; Couderc, E.; Faure-Vincent, J.; Sadki, S.; Pron, A.; Reiss, P. *J. Mater. chem.*, **2011**, *21*, 11524–11531.

[56] Liu, S.-M.; Gou, H.-Q.; Zhang, Z.-H.; Li, R.; Chen, W.; Wang, Z.-G. *Physica E*, **2000**, *8*, 174–178.

[57] Wolcott, A.; Doyeux, V.; Nelson, C. A.; Gearba, R.; Lei, K. W.; Yager, K. G.; Dolocan, A. D.; Williams, K.; Nguyen, D.; x. Y. Zhu. *J. Phys Chem. Lett.*, **2011**, *2*, 795–800.

[58] Efros, A. L.; Rosen, M.; Kuno, M.; Nirmal, M.; Norris, D. J.; Bawendi, M. *Phys. Rev. B*, **1996**, *54*, 4843–4856.

[59] Shiang, J. J.; Kadavanich, A. V.; Grubbs, R. K.; Alivisatos, A. P. *J. Phys. Chem.*, **1995**, *99*, 17417–17422.

[60] de Mello Donegà, C.; Boda, M.; Meijerink, A. *Phys. Rev. B*, **2006**, *74*, 085320.

[61] Bawendi, M. G.; Wilson, W. L.; Rothberg, L.; Carroll, P. J.; Jedju, T. M.; Steigerwald, M. L.; Brus, L. E. *Phys. Rev. Lett.*, **1990**, *65*, 1623.

[62] Murray, C. B.; Kagan, C. R.; Bawendi, M. G. *Annu. Rev. Mater. Sci*, **2000**, *30*, 545–610.

[63] Kagan, C. R.; Murray, C. B.; Nirmal, M.; Bawendi, M. G. *Phys. Rev. Lett.*, **1996**, *76*, 1517–1520.

[64] Underwood, D. F.; Kippeny, T.; Rosenthal, S. J. *J. Phys. Chem. B*, **2001**, *105*, 436–443.

[65] Leung, K.; Whaley, K. B. *J. Chem Phys*, **1999**, *110*, 11012–11022.

[66] Prokant, S.; Whaley, K. B. *Eur. Phys. J. D*, **1999**, *6*, 255–267.

[67] Völker, J.; Zhou, X.; Ma, X.; Flessau, S.; Lin, H.; Schmittel, M.; Mews, A. *Chem. Soc. Rev.*, **2010**, *49*, 6865–6868.

[68] Guyot-Sionnest, P.; Shim, M.; Matranga, C.; Hines, M. *Phys. Rev. B*, **1999**, *60*, 2181–2184.

[69] Wuister, S.; de Mello Donegà, C.; Meijerink, A. *J. Phys. Chem. B*, **2004**, *108*, 17393–17397.

[70] Guyot-Sionnest, P.; Wang, C. *J. Phys. Chem. B*, **2003**, *107*, 7355–7359.

[71] Lee, J.-S.; Kovalenko, M. V.; Huang, J.; Chung, D. S.; Talapin, D. V. *Nat. Nanotech.*, **2011**, *6*, 348–352.

[72] Vanmakelbergh, D.; Liljeroth, P. *Angew. Chem., Int. Ed.*, **2005**, *34*, 299–

312.

[73] Guyot-Sionnest, P. *J. Phys. Chem. Lett.*, **2012**, *3*, 1169–1175.

[74] Chu, I.-H.; Radulaski, M.; Vukmirovic, N.; Cheng, H.-P.; Wang, L.-W. *Phys. Chem. C*, **2011**, *115*, 21409–21415.

[75] Miller, A.; Abrahams, E. *Phys. Rev.*, **1960**, *120*, 745–755.

[76] Marcus, R. A. *Annu. Rev. Phys. Chem.*, **1965**, *16*, 155.

[77] Koberling, F.; Kolb, U.; Philipp, G.; Potapova, I.; Basché, T.; Mews, A. *J. Phys. Chem. B*, **2003**, *107*, 7463–7471.

[78] Bawendi, M. G.; Kortan, A. R.; Steigerwald, M. L.; Brus, L. E. *J. Chem. Phys.*, **1989**, *91*, 7282.

[79] Scherrer, P. *Nachr. Ges. Wiss. Göttingen*, **1918**, *26*, 98–100.

[80] Langford, J.; Wilson, A. *J. Appl. Cryst*, **1978**, *11*, 102–113.

[81] EP10176561, Bayer Technology Services GmbH. Patent application on pending.

[82] Scriven, L. E. *Better Ceramics Through Chemistry III.* C. J. Brinker, D. E. Clark and D. R. Ulrich (eds) Mat. Res. Soc., Pittsburgh, Pa., 1988.

[83] Landau, L. D.; Levich, B. G. *Acta Physiochim. U.R.S.S.*, **1942**, *17*, 42–54.

[84] Kronik, L.; Shapira, Y. *Surf. Science Rep.*, **1999**, *37*, 1–206.

[85] extended lecture, T. Dittrich, http://www.helmholtz-berlin.de/media/media/forschung/energie/heterogen/eta/methods/spv-techniques-2010-08-09.pdf. accesed 02.08.2012.

[86] Dittrich, T.; Bönisch, S.; Zabel, P.; Dude, S. *Rev. Sc. Instr.*, **2008**, *79*, 113903.

[87] Mahrov, B.; Boschloo, G.; Hagerfeldt, A.; Dloczik, L.; Dittrich, T. *Appl-Phys. Lett.*, **2004**, *84*, 5455.

[88] Mora-Seró, I.; Bisquert, J.; Dittrich, T.; Belaidi, A.; Susha, A. S.; Rogach, A. L. *J. Phys. Chem. C*, **2007**, *111*, 14889–14892.

[89] Zidon, Y.; Shapira, Y.; Dittrich, T. *Appl. Phys. Lett.*, **2007**, *90*, 142103.

[90] Fungo, F.; Milanesio, M. A.; Durantini, E. N.; Otero, L.; Dittrich, T. *J. Mater. Chem.*, **2007**, *17*, 2107.

[91] Mora-Seró, I.; h, T.; Garcia-Belmonte, G.; Bisquert, J. *J. Appl. Phys.*,

2006, *100*, 103705.

[92] Duzhko, V.; Timushenko, V. Y.; Koch, F.; Dittrich, T. *Phys. Rev. B*, **2001**, *64*, 075204.

[93] Schmid, M. *Optik der $CuGaSe_2$-Solarzelle für hocheffiziente Tandemkonzepte*. PhD thesis, Freie Universität Berlin, 2009.

[94] Tyborsky, T. *Struktuelle und optische Untersuchungen an graphitischem Kohlenstoffnitrid - ein Photokatalysator für die lichtinduzierte Wasserstoffzerzeugung*. Master's thesis, Freie Universität Berlin, 2011.

[95] Merschjann, C.; Mews, M.; T, M.; Karakatzinou, A.; Urusu, M.; Korzun, B. V.; anc P. Schubert-Bischoff, S. S.; Seeger, S.; Schedel-Niedreig, T.; Lux-Steiner, M.-C. *J. Phys.: Condens. Matter.*, **2012**, *24*, 175801.

[96] Rubin, S.; Passell, T. O.; Bailey, E. *Analytical Chemistry*, **1957**, *29*, 736–743.

[97] Leavitt, J. A.; McIntyre, L. C.; Weller, M. R. *Handbook of Modern Ion Beam Materials Analysis*. J. R. Tesmer, M. Nastasi, J. Ch. Barbour, C. J. Maggiore and J. W. Mayer (eds) Mat. Res. Soc., Pittsburgh, Pa., 1995.

[98] Morgan, D. V.; Gittins, R. P. *phys. stat. sol. (a)*, **1972**, *13*, 517–525.

[99] Barradas, N. P.; Jeanes, C.; Webb, R. P. *Appl. Phys. Lett.*, **1997**, *71*, 291–293.

[100] Chu, W.-K.; Mayer, J. W.; Nicolat, M.-A. *Backscattering Spectrometry*. Academic Press, New York, 1978.

[101] Chu, W.-K.; Mayer, J. W.; Nicolat, M.-A.; Buck, T. M.; Amsel, G.; Eisen, F. *Thin Solid Films*, **1973**, *17*, 1–41.

[102] Zillner, E.; Dittrich, T. *Phys. Stat. Sol. RRL*, **2011**, *5*, 256–258.

[103] Zillner, E.; Fengler, S.; Niyamakom, P.; Rauscher, F.; Köhler, K.; Dittrich, T. *Chem. Phys. C.*, **2012**, *116*, 16747–16754.

[104] Ueda, A.; Tayagaki, T.; Kanemitsu, Y. *J. Phys. Soc. Jpn.*, **2009**, *78*, 083706.

[105] Talgorn, E.; de Vries, M. A.; Siebbeles, L. D. A.; Houtepen, A. J. *ACS Nano*, **2011**, *5*, 3552–3558.

[106] Talgorn, E.; Moysidou, E.; Abellon, R. D.; Savenija, T. J.; Goossens, A.; Houtepen, A. J.; Siebbeles, L. D. A. *J. Phys. Chem. C*, **2010**, *114*, 3441–

3447.

[107] Valerini, D.; Creto, A.; Lomascolo, M.; Manna, L.; Cingolani, R.; Anni, M. *Phys. Rev. B*, **2005**, *71*, 235409.

[108] Garnett, J. C. M. *Philos. Trans. R. Soc. London, Ser. B*, **1904**, *203*, 385.

[109] Wohlfarth, C. *Landolt-Börnstein: Group IV: Macroscopic and Technical Properties of Matter, Volume 6 Static Dielectric Constants of Pure Liquids and Binary Liquid Mixtures*. Springer- Verlag, Berlin, Heidelberg, New York, 1999.

[110] Ennaoui, A.; Bär, M.; Klaer, J.; Kropp, T.; Sáez-Araoz, R.; Lux-Steiner, M. C. *Progress in Photovoltaics*, **2006**, *14*, 499–511.

[111] Sankar, N.; Sanjeeviraja, C.; Ramachandran, K. *Journal of Crystal Growth*, **2002**, *243*, 117–123.

[112] Zillner, E.; Kavalakkatt, J.; Eckhardt, B.; Dittrich, T.; Ennaoui, A.; Lux-Steiner, M. *Thin Solid Films*, **2012**, *520*, 5500–5503.

[113] Gur, I.; Fromer, N. A.; Geier, M. L.; Alivisatos, A. P. *Science*, **2004**, *310*, 462 – 465.

[114] Ding, X. M.; Hung, L. M.; Cheng, L. F.; Deng, Z. B.; Hou, X. Y.; Lee, C. S.; Lee, S. T. *Appl. Phys. Lett.*, **2000**, *76*, 2704 – 2706.

[115] Schlaf, R.; Murata, H.; Kafafi, Z. H. *J. of Electron Spectroscopy and Related Phenomena*, **2000**, *120*, 149 – 154.

Publications

Journal Articles

Elisabeth Zillner, Björn Eckhardt, Ahmed Ennaoui, Martha Ch. Lux-Steiner and Thomas Dittrich, Charge transfer from CdTe quantum dots into a CdS thin layer. Energy Procedia **2011**, *10*, 225 – 231.

Elisabeth Zillner and Thomas Dittrich, Surface photovoltage within a monolayer of CdSe quantum dots. Phys. Stat. Sol. RRL **2011**, *5*, 256 – 258.

Elisabeth Zillner Jaison Kavalakkatt, Björn Eckhardt, Thomas Dittrich, Ahmed Ennaoui and Martha Lux-Steiner. Thin Solid Films **2012**, *520*, 5500 – 5503.

Elisabeth Zillner Steffen Fengler, Phenwisa Niyamakom, Frank Rauscher, Karen Köhler and Thomas Dittrich Role of Ligand Exchange at CdSe Quantum Dot Layers for Charge Separation. J. Phys. Chem. C **2012**, *116*, 16747 – 16754.

Conference Presentations - Oral Presentations

Elisabeth Zillner, Björn Eckhardt, Ahmed Ennaoui, Martha Ch. Lux-Steiner and Thomas Dittrich, Charge transfer from CdTe quantum dots into a CdS thin layer. European Materials Research Society, Spring Meeting 2011, May 9 –13, Nice (France).

Elisabeth Zillner, Steffen Fengler and Thomas Dittrich, Role of ligand exchange at CdSe quantum dot layers for charge separation. European Society for Quantum Solar Energy Conversion, Winter Workshop 2012, March 11 –16, Bad Gastein

(Austria).

Elisabeth Zillner, Steffen Fengler and Thomas Dittrich, Role of surfactants and defect generation in CdSe QD layers for separation of photo-generated charge carriers. Spring Meeting of the German Physical Society 2012, March 25 –30, Berlin (Germany).

Conference Presentations - Poster Presentations

Elisabeth Zillner, Karen Köhler and Frank Rauscher and Thomas Dittrich, Transient surface photovoltage study of charge separation in ultrathin CdSe quantum dot layers. 13. JCF-Frühjahrssymposium 2011, March 23 –26, Erlangen (Deutschland).

Elisabeth Zillner and Thomas Dittrich, Investigation of charge separation in semiconductor quantum dot layer systems by surface photovoltage. Nano IS Green Conference 2011, June 19 – 24, Bar-Ilan University (Israel).

Acknowledgments

First of all I want to thank Prof. Lux-Steiner for accepting me in her group and giving me the opportunity to do my PhD thesis at the Helmholtz-Zentrum Berlin. Special thanks go to PD. Dr. Thomas Dittrich for accepting me as his PhD student and for his great supervision. Thank you for helping me with your knowledge, your experience and the many long discussions we had.
Acknowledgments also to Prof. Rühl for his willingness to act as the co-examiner of this PhD thesis.
I am grateful to Dr. Köhler, Dr. Niyamakom and Dr. Rauscher from BTS for the preparation and TGA-MS measurements of CdSe QDs and CdTe NPs.
Acknowledgments also to the BMBF (grant: 03SF0363B) for financial support.
Thank you to Steffen Fengler for a year of very effective teamwork on the mechanisms of charge separation in CdSe QD layers, the development of the program for SPV transient simulation and your help with physics.
Many thanks to Björn Eckhardt for good work in the laboratory together on the preparation of QD layers and for the preparation of electrophoretic deposited QD layers. Thank you also for the discussions, your much appreciated feedback and a great time.
I want to thank Albert Juma for being a great office mate. I really enjoyed our (not always) scientific discussion and thank you for your feedback.
Many thanks to Dr. Christoph Merschjann for the introduction into PL spectroscopy and the assistance with interpretation of PL data.
Acknowledgments to Jaison Kavalakkatt, Ulrike Blöck and Dr. Elke Wendler for SEM, TEM and RBS measurements.
Thank you to the whole E-I2 group for a great time, especially the coorganizers of the ISUenergy Johanna, Susanna, Jaison, Christoph, Iver and Tristan.
Last but not least I want to say thank you to Andreas for listening to my doubts and worries and for being alway patient and encouraging.